8-2010

COMBINED MUSCULO-SKELETAL MULTI-BODY DYNAMICS/FINITE ELEMENT ANALYSIS OF SEVERAL ERGONOMICS AND BIO-MECHANICS PROBLEMS

Xin Xie
Clemson University, xxie@clemson.edu

Recommended Citation

Xie, Xin, "COMBINED MUSCULO-SKELETAL MULTI-BODY DYNAMICS/FINITE ELEMENT ANALYSIS OF SEVERAL ERGONOMICS AND BIO-MECHANICS PROBLEMS" (2010). *All Theses*. 873.
https://tigerprints.clemson.edu/all_theses/873

COMBINED MUSCULO-SKELETAL MULTI-BODY DYNAMICS/FINITE ELEMENT ANALYSIS OF SEVERAL ERGONOMICS AND BIO-MECHANICS PROBLEMS

A Thesis
Presented to
the Graduate School of
Clemson University

In Partial Fulfillment
of the Requirements for the Degree
Master of Science
Mechanical Engineering

---

by
Xin Xie
August 2010

Accepted by:
Mica Grujicic, Committee Chair
Martine LaBerge
Yong Huang
Gang Li

ABSTRACT

Within this thesis, two ergonomics (i.e. seating comfort and long-distance driving fatigue problems) and two structural bio-mechanics (i.e. femur-fracture fixation and radius-fracture fixation) problems are investigated using musculo-skeletal multi-body dynamics and finite element computational analyses.

Within the seating comfort problem analyzed, a complete-body finite element model is constructed and used to assess the effect of seat geometry and seating posture on the feel of comfort experienced by a seated human.

Within the long-distance driving fatigue problem, musculo-skeletal analysis is employed to assess the extent of fatigue experienced by a driver through the evaluation of level of activity of his/her various muscles.

Within the femur-fracture fixation problem, physiologically realistic loading conditions associated with active daily activities (i.e. cycling) are employed within a finite-element frame work to assess fracture fixation performance and durability of the implant.

Within the radius-fracture fixation problem, the analysis developed within the femur-fracture fixation problem is further related to indicate the effects of other types of loadings (associated with additional daily activities) and improved biological and structural material model are employed.

For all cases studied in the present work, relevant experimental data are used to validate the computational procedure employed.

DEDICATION

This thesis is dedicated to my parents, who gave me great support for my study in Clemson University and taught me how to become a good engineer.

ACKNOWLEDGMENTS

I am heartily thankful to my graduate advisor, Dr.Mica Grujicic, whose encouragement, guidance and support from the initial to the final level enabled me to develop an understanding of this topic. Also, I offer my regards and blessings to my advising committee members, Dr.Martine LaBerge, Dr.Yong Huang and Dr.Gang Li, as well all my group colleagues who helped me a lot during the completion of this thesis.

TABLE OF CONTENTS

Page

CHAPTER

LIST OF TABLES

Table Page

LIST OF FIGURES

CHAPTER ONE

INTRODUCTION

In the present work, a couple of ergonomics problems (i.e. seating comfort and long-distance driving fatigue) and two bio-mechanics (i.e. a femur-fracture and radius-fracture implant-fixation) problems are investigated computationally. In each case, the relevant open-literature experimental results are used to judge validity/fidelity of the present computational approach. As will be shown in the subsequent four chapters, the overall agreement between the computation and experiment is reasonably suggesting that the present computational approach has the potential of greatly helping further advances in the area of ergonomics and bio-mechanics.

The organization of the present thesis is as follows. In Chapter 2, the problem of seating comfort is presented and discussed. The main computational tool used in this section is the finite element method. In Chapter 3, the problem of long-distance driving fatigue is treated computationally. In this case, the finite element analysis is complemented by a musculo-skeletal multi-body dynamics analysis to create physiologically realistic loading conditions experienced by a human-body during driving.

In Chapter 4, the problem of femoral-fracture fixation is analyzed using both the musculo-skeletal multi-body and structural bio-mechanics finite element analysis. The same approach is next extended in Chapter 5 to the problem of radius-fracture fixation. In

Chapter 6 and Chapter 7, a brief summary of the work is presented and recommendations are made for the future work, respectively.

CHAPTER TWO

SEAT-CUSION AND SOFT-TISSUE MATERIAL MODELING AND A FINITE ELEMENT INVESTIGATION OF THE SEATING COMFORT FOR PASSENGER-VEHICLE OCCUPANTS

ABSTRACT

Improved seating comfort is an important factor that most car manufacturers use to distinguish their products from those of their competitors. In today's automotive engineering practice, however, design and development of new, more comfortable car seats is based almost entirely on empiricism, legacy knowledge and extensive, time-consuming and costly prototyping and experimental/field testing. To help accelerate and economize the design/development process of more-comfortable car seats, more extensive use of various computer aided engineering (CAE) tools will be necessary. However, before the CAE tools can be used more successfully by car-seat manufacturers, issues associated with the availability of realistic computer models for the seated human, the seat and the seated-human/seat interactions as well as with the establishment of objective seating-comfort quantifying parameters must be resolved.

In the present work, detailed finite element models of a prototypical car seat and of a seated human are developed and used in the investigation of seated-human/seat interactions and the resulting seating comfort. To obtain a fairly realistic model for the human, a moderately detailed skeletal model containing 16 bone assemblies and 15 joints has been combined with an equally detailed ‘‘skin” model of the human. The intersection

between the two models was then used to define the muscular portion of the human. Special attention in the present work has been given to realistically representing/modeling the materials present in different sections of the car seat and the seated human. The models developed in the present work are validated by comparing the computational results related to the pressure distribution over the seated-human/seat interface with their open-literature counterparts obtained in experimental studies involving human subjects.

Ii.1. INTRODUCTION

Today, in the industrialized world, sitting is the most common working posture and perhaps the most frequent leisure posture. It is well-recognized that constrained sitting postures can lead to discomfort and health disorders (e.g. back, neck and shoulder pain, etc.) which translates into a major cost to society through missed work and reduced work-effectiveness/productivity [2.1]. Consequently, furniture manufacturers and car-seats manufacturers are forced to more aggressively address seating ergonomics in order to gain a competitive edge. In the automotive industry, the ever increasing customer demand for vehicles with improved performance has been complimented by an equally strong demand for vehicles with improved comfort. As a result, vehicle manufacturers use car-seat/interior comfort as an important selling point and a way to distinguish themselves from their competitors. (Vehicle seats and the comfort level they can offer to the seated individual is the subject of the present work.) The current state of the car-seat manufacturing industry is such that development and introduction of new, more-comfortable car seats is based almost entirely on empiricism, legacy knowledge and extensive, time-consuming and costly prototyping and experimental/field testing. 64

Considering the fact that Computer Aided Engineering (CAE) has made major contribution and has become an indispensible tool to many industries, one should expect that CAE should be used more aggressively by the car-seat manufacturing industry in order to address the issue of seating comfort. That is, the use of computer models of a human and seat, and the analysis of their interactions could facilitate, accelerate and economize the process of development and introduction of new, more comfortable car seats. Specifically, in the early stages of the seat-design process, a new design can be tested for its degree of comfort by carrying out computer simulations of the seated-human interactions with the seat. However, before these computer simulations can become reliable, high-fidelity seating-comfort assessment tools, a critical problem of identifying/defining the objectives and measurable comfort- quantifying parameters/measures and the establishment of their correlation with the subjective feeling of comfort has to be solved. Among the comfort-quantifying parameters, the ones most frequently cited are: (a) the average human/seat contact pressure; (b) the maximum human/seat contact pressure; (c) the human/seat contact-area size and (d) the extent of symmetry of the human/seat contact-area [2.2 – 2.14]. All of these comfort-quantifying parameters are based on measurements of the distribution of human/seat contact pressure over the contact area and these measurements commonly suffer from several limitations, e.g. [2.15,2.16]: (a) they are relatively difficult to perform reproducibly and with high accuracy; (b) the obtained contact-pressure distributions do not provide any information about internal stresses and deformations of the human soft tissues and (c) the contact pressure distributions measured provide only information about the normal stresses at the contact human/seat interface whereas it is well established that significant shear stresses can be present at the human/seat interface, e.g. [2.17 – 2.22]. In addition, the contact-pressure distribution-measurement approach has major deficiencies in its ability (or total lack thereof) to provide information about the level of muscular activity and about the magnitude of joint forces, two quantities which are certainly related to the seating comfort.

To address some of the shortcomings of the contact-pressure distribution-measurement approach, various human-body/seat coupled computer models and computational analyses were proposed. For example, a finite-element based modeling approach was introduced by Verver et al. [2.23] and a rigid-body mechanical based model was suggested by Langford et al. [2.24], etc. While these approaches were able to provide estimates for some of the parameters that are either difficult or impossible to obtain via direct measurements, so far however, it has not been possible to create a model that can calculate how muscular activity and joint forces are affected by changes in sitting conditions. The main reason for this is that the human body, in general, and its muscular and skeletal systems, specifically, is quite challenging mechanical systems to model.

To address the limitations of the seating-comfort assessment computer modeling schemes mentioned above, the AnyBody Research Group [2.25] at Aalborg University in Denmark in collaboration with three furniture manufacturers recently initiated a research project entitled ‘‘The Seated Human’’. The main objective of this project is to define a set of seating-comfort design criteria for chairs and to devise the means (based on rigorous computer modeling of the human musculoskeletal system) for reliable assessment of these criteria. Within the project, the recently-developed novel technology for computer modeling of the human-body mechanics and dynamics, namely the AnyBody Modeling System [2.25] and its associated public domain library of body models are being fully utilized and further developed. In its most recent rendition [2.26], the AnyBody Modeling System enables creation of a detailed computer model for a human body (including all important components of the musculoskeletal system) as well as examination of the influence of different postures and the environment on the internal joint forces and muscle activity.

The earliest public-domain report related to the human body in a seated posture can be traced back to the pioneering analytical investigation conducted by Mandal [2.27, 2.28] who used simple physics-based reasoning in place of the traditional empirical and subjective approaches. The main outcome of Mandal's work was that it is beneficial from the spinal-loads reduction point of view to reduce the pelvic rotation (i.e. flexion between the pelvis and the thorax) below a normal value of 90° in the seated-human posture (by tilting the seat-pan forward and/or the backrest backward). In a recent multi-body dynamics based work carried out by Rasmussen et al. [2.29 – 2.32] it was shown that forward seat-pan inclination indeed can reduce the spinal-joint loads. However, forward seat-pan inclination was also found to increase the maximum muscle activity (i.e. muscle fatigue) unless sufficient friction is present at the human-buttocks/seat interface in which case its spinal-joint load-reduction beneficial effect diminishes and is replaced with an comfort-compromising/harmful effect of inducing shear forces in the human soft tissue.

While the work of Rasmussen et al. [2.29 – 2.32] has made major contributions to the field of seating comfort/discomfort, it has also revealed some of the limitations of the multi-body dynamics musculoskeletal approach with respect to modeling the interactions between the seated human and the seat. Simply stated, while the multi-body dynamics approach can in general capture the overall magnitudes of normal and shear interaction forces between the seated human and the seat, the distribution of the forces over the contact interface and their penetration into the human soft tissue could not be addressed. It appears clear that further progress in the area of seating-comfort modeling and simulation will come through additional advances in both the multi-body dynamics musculoskeletal and finite-element analyses of the seated-human/seat interactions and by finding ways to cooperatively and interactively engage these two modeling/simulation approaches.

The main purpose of the present work is to introduce a fairly detailed finite-element model for a seated human and for a generic car seat and to carry out a preliminary computational finite element analysis of the seated-human/seat interactions in order to help identify the factors which affect seating comfort/discomfort. A review of the literature carried out as part of the present work revealed several finite-element models of the seated human. However, all these models suffer from one or more serious limitations such as: (a) over-simplification of the geometry of the skeletal and/or muscular portions of the model [2.16, 2.19, 2.33 – 2.35]. As explained before, the maximum human/seat contact pressure and its distribution are related to the seating comfort. It is well-established that the maximum contact pressure occurs under the ischial tuberosities and for a finite-element model to correctly predict the location of the maximum contact pressure it must provide an accurate geometrical description of the skeletal system of the human body; (b) excessive coarseness of the finite-element mesh used in order to reduce the computational cost [2.36 – 2.38] which yields to less accurate computational results and (c) geometrical details of the skeletal and the muscular systems are obtained from different sources and they are somewhat inconsistent [2.39].

II.2. MODELING AND COMPUTATIONAL PROCEDURES

II.2.1. Finite Element Model of the Car Seat

A generic car-seat finite element model was constructed within this work, Figure 2-1. First, a solid-geometrical model was developed using CATIA V5, a CAD computer program [2.40]. Then, the CAD model was pre-processed using HyperMesh, a general purpose analysis pre-processing software [2.41] to construct a meshed model with all the required sections, materials, joints, initial and boundary condition definitions.

The car-seat model comprised five shell components (foot-rest, seat-base, seat-pan back-face, back-rest back-face and head-rest back-face) and three solid components (seat-pan, back-rest and head-rest), Figure 2-1. The shell components were meshed using 3,220 three-node first-order shell finite elements while the solid sections were discretized using 21,200 four-node first-order tetrahedron solid finite elements.

The shell sections of the car seat were constructed using low-car- bon steel with a Young’s modulus of 210 *GPa* and a Poisson’s ratio of 0.3. Since the loading experienced by the seat is solely caused by the weight of the seat occupant, and is hence not excessively high, plasticity of the steel components of the seat was not considered.

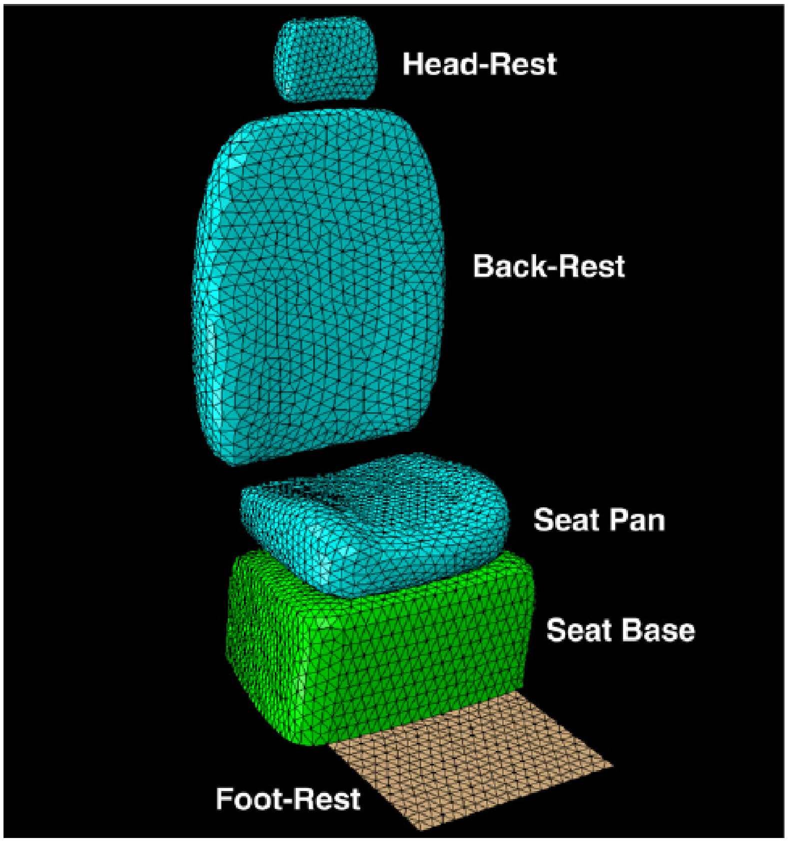

Figure 2-1. Finite element model for the car seat used in the present work.

Solid sections of the seat were constructed using a hyperelastic foam (a poly-urethane seat-cushion like) material. This material was represented using a non-linear isotropic compressible hyperelastic foam (i.e., a ‘‘hyperfoam”) material model. Within the hyperelastic foam material model formulation, the unique (generally non-linear) relation between the stress and the strain measures is represented using an elastic strain-energy potential function, W, in the form:

$$W = \sum_{i=1}^{N} \frac{2\mu_i}{\alpha_i^2} \left[\hat{\lambda}_1^{\alpha_i} + \hat{\lambda}_2^{\alpha_i} + \hat{\lambda}_1^{\alpha_i} - 3 + \frac{1}{\beta_i} \left(\left(J^{el} \right)^{-\alpha_i \beta_i} - 1 \right) \right] \qquad (2.1)$$

where N (=1, 2, 3) is the polynomial model order μ_i, α_i and β_i are temperature-dependent material parameters; $\hat{\lambda}_i = \left(J^{th} \right)^{-\frac{1}{3}} \lambda_i$, $\hat{\lambda}_1 \hat{\lambda}_2 \hat{\lambda}_3 = J^{el}$ and λ_is are the principal stretches. J^{el} is the elastic-deformation volume-change ratio and J^{th} is the thermal-strain volume-change ratio. The coefficient β_i controls the degree of compressibility and is related to the Poisson's ratio, v_i. It should be further noted that in order to account for the thin cell-wall closed-cell structure of the foam which allows wall buckling under pressure without lateral resistance/constraints, principal stresses/strains are assumed to be fully de-coupled. In other words, the Poisson's effect was neglected and the Poisson's ratio set to zero.

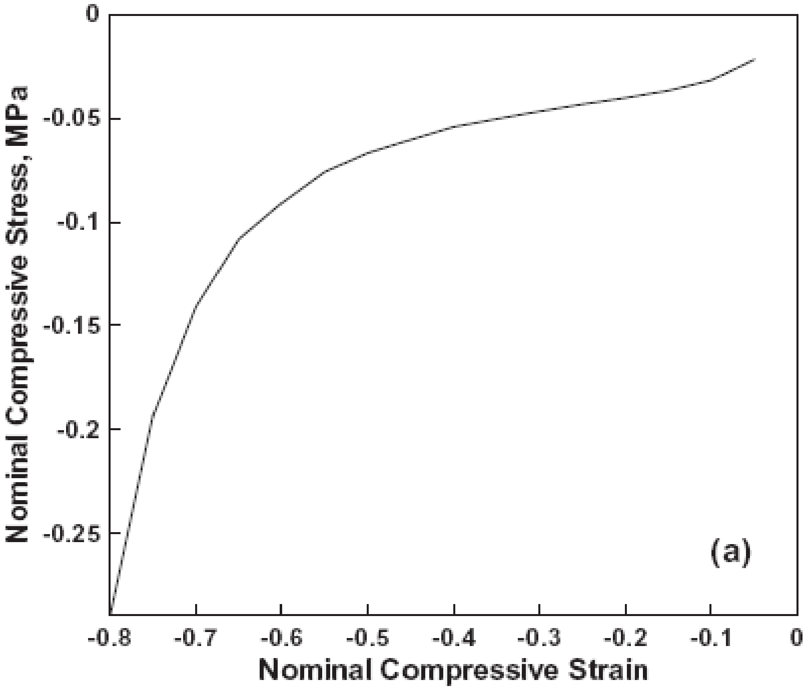

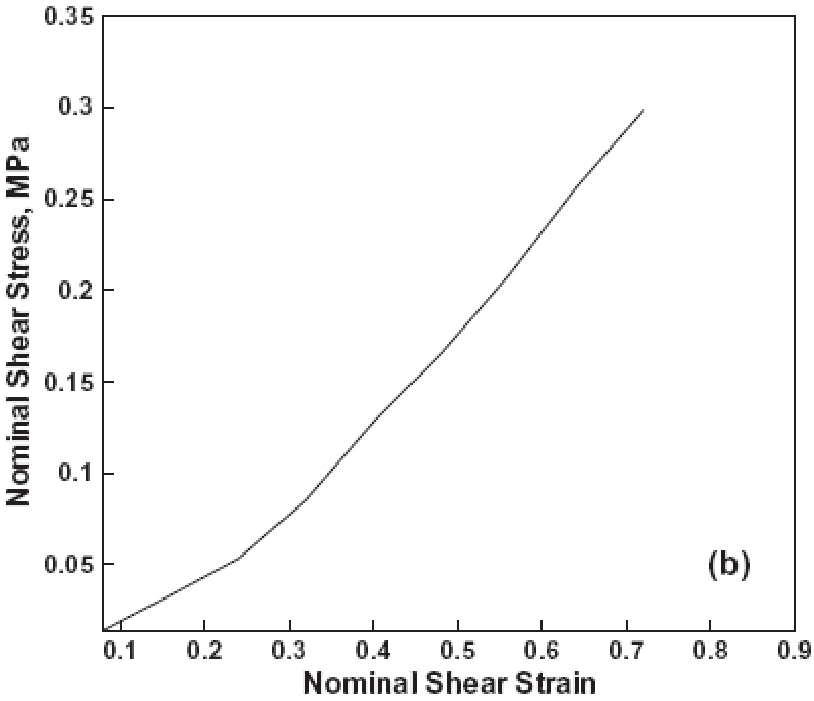

Figure 2-2. (a) Uniaxial compression and (b) Simple shear test data used in the construction of the non-linear elastic part of the hyperfoam material model.

In the present work, a second order (i.e. $N = 2$) strain energy hyperfoam potential function was used. Parameterization of this model was done by providing to ABAQUS/Standard (the general-purpose finite-element package used in the present work [2.50]) uni-axial-compression and simple-shear nominal stress vs. nominal strain experimental test data, Figures 2-2a and b. The data were obtained in an experimental investigation carried out in accordance with ASTM 3574-01 [2.48]. ABAQUS/Standard then performs a non-linear least-squares fit of the provided test data to determine the hyper-foam model parameters μ_i, α_i and β_i. This procedure yielded the following results: $\mu_1 = 164.861\ kPa$, $\alpha_1 = 8.88413$, and $\beta_1 = 0.0$, and $\mu_2 = 0.023017\ kPa$, $\alpha_2 = -4.81798$, and $\beta_2 = 0.0$. Within the hyper-foam material model used in the present work, principal components of the stress (more precisely, principal components of the Cauchy stress tensor, σ) are obtained by differentiating the strain energy function W with respect to the principal stretches, λ_is, as:

$$\sigma_i = J^{el-1}\lambda_i \frac{\partial W}{\partial \lambda_i} \tag{2.2}$$

Since the polyurethane foam modeled in the present work falls into the class of elastomeric-foam materials, which displays viscoelastic behavior, viscoelasticity was added to the hyperelastic model described above. To define the viscoelastic portion of the seat-cushion foam model, a time-based Prony-series model for the shear modulus was used. Since time dependency of the bulk modulus is generally quite weak in this type of material, the viscoelastic portion of the material model was confined to the shear modulus. Within this model, the time-dependent shear modulus, G(t), is defined in terms of the instantaneous shear modulus, G_0, as:

$$G(t) = G_0 - \sum_{i=1}^{N} G_i (1 - e^{-\frac{t}{\tau_i}}) \tag{2.3}$$

where G_i (the relaxation magnitude) and τ_i (the relaxation time) are material dependent parameters and N is the order of the Prony-series ($N = 2$ in the present work).

The viscoelastic portion of the foam model is defined in the present work by providing ABAQUS/Standard with the experimental normalized shear modulus, $G(t)/G_0$ vs. time relaxation data, Figure 2-3. These data are filled using a non-linear least squares procedure to define the viscoelastic material parameters, G_i and τ_i. This procedure yielded the following results: $G_1 = 0.3003$ and $\tau_1 = 0.010014$ s, and $G_2 = 0.1997$ and $\tau_2 = 0.1002$ s. It should be noted that while the viscoelastic part of the elastomeric-foam material; model was developed and parameterized in the present work, due to static nature of the computational analysis used, the role of viscoelasticity was immaterial.

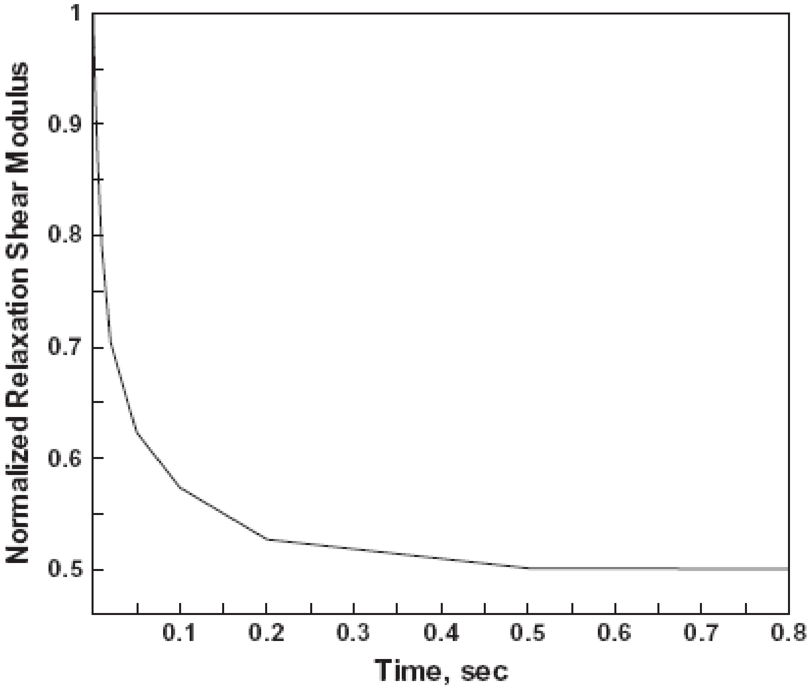

Figure 2-3. Normalized shear modulus relaxation data used in the construction of the viscoelastic portion of the hyperfoam material model.

II.2.2. Finite Element Model of the Seated Human

A new finite element model of the seated human was developed within the present work. The model was constructed by (somewhat) simplifying and re-posturing the human-body skeleton model downloaded from the AnyBody Repository [2.42], Figure 2-4, and combining it with a human-body shell model developed by F. Summer [2.43], Figure 2-5.

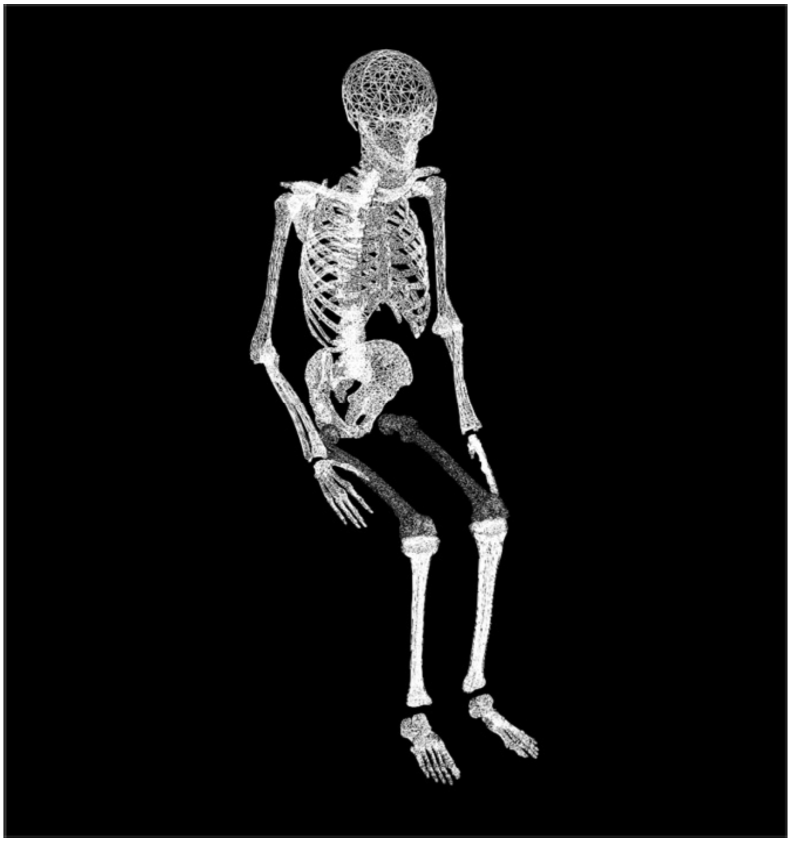

Figure 2-4. Finite element model for the skeletal portion of the seated human analyzed in the present work.

The human-body skeleton model used included a fairly detailed anatomical description of the main bony structures (e.g. the *iliac wings* comprising *the ischial tuberosities, sacrum, coccyx and femora*). The intersection of the two models was used to define the portion of the human body filled with soft tissue (muscles, ligaments and fat). The outer surface of the model was covered with skin while the skeletal portion of the model was filled with (hollow) bones. The skin portion of the human body model was meshed using ca. 60,000 three-node shell elements, the soft-tissue portion with ca. 135,000 four-node first-order tetrahedron elements while the bones were meshed using ca. 30,000 three-node shell elements. Equivalent nodes were used between the skin and the soft tissue as well as between the soft tissue and the bones.

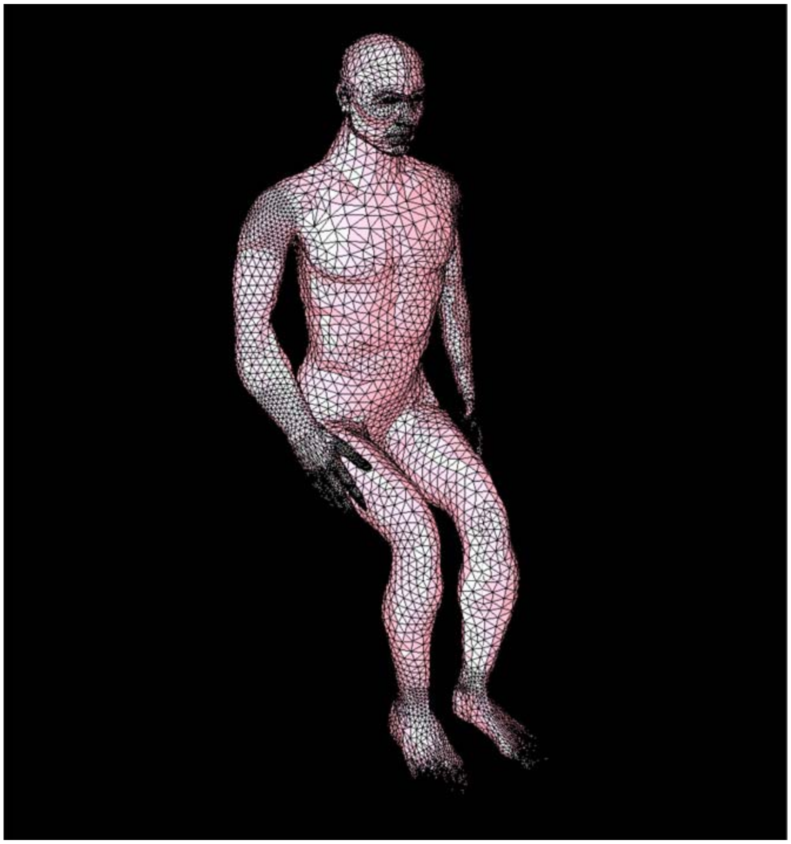

Figure 2-5. Finite element model for the muscular portion of the seated human analyzed in the present work.

Three different materials (bones, soft-tissue muscle/fat and skin) are used in the construction of the seated-human finite-element model.

Following the work done in Refs. [2.44,2.45], the skin was modeled as a linearly-elastic isotropic nearly-incompressible material with a Young's modulus of 0.15 *MPa*, a Poisson's ratio of 0.46 and an average density of 1100 kg/m^3.

Individual bones of the skeletal portion of the human-body model are constructed using a rigid (non-deformable) material with densities adjusted to yield accurate bone masses. The use of the rigid-material approximation was justified by the fact that the extents of deformation experienced by the bones are so small in comparison to that experienced by the soft tissue, that it can be ignored. Various (e.g. spherical, revolute, etc.) connectors were used to represent the joints connecting adjacent bones. For example, a spherical joint was placed between the lumbar spine and the pelvis, two spherical joints representing hips were placed between the iliac wings and the two femur bones, two revolute (knee) joints were placed between the femora and the lower legs, etc. A total of 15 connectors/joints were used in the skeletal portion of the human-body model.

The muscular portion of the human-body was modeled using a Mooney–Rivlin hyperelastic isotropic material model. This model is capable of accounting for large (non-linear) elastic deformations that soft tissue of the seated human can be subjected to, due to human/seat interactions. In the literature, it is well-established that a non-linear hyperelastic isotropic material model is a best compromise between physical reality and computational efficiency when dealing with the human-body soft tissue. However, the type(s) of the hyperelastic isotropic material model and their parameterizations vary widely [2.15, 2.16, 2.19, 2.39, 2.45 – 2.47]. Within the hyperelastic isotropic material model formulation, the unique (generally non-linear) relation between the stress and the strain measures is represented using an elastic strain-energy potential function. Within the

Mooney–Rivlin model used in the present work, the strain-energy potential function, W, is defined as:

$$W = A_1(J_1 - 3) + A_2(J_2 - 3) + A_3(J_3^{-2} - 1) + A_4(J_3 - 1)^2 \quad (2.4)$$

where J_1, J_2 and J_3 are the three invariants of the Cauchy–Green strain tensor, C, defined as:

$$C = F^T F \quad (2.5)$$

with F being the deformation-gradient tensor and superscript ‘‘*T*” denotes a transverse of the tensor in question. The three invariants of the C tensor are defined respectively as:

$$J_1 = trace(C) \quad (2.6)$$

$$J_2 = \frac{1}{2}\left[trace^2(C) - trace(C^2)\right] \quad (2.7)$$

$$J_3 = \det(C) \quad (2.8)$$

In Eq. 2.4, the material-dependent parameters A_3 and A_4 are related to the other two parameters, A_1 and A_2, as:

$$A_3 = \frac{1}{2}A_1 + A_2 \quad (2.9)$$

and

$$A_4 = \frac{A_1(5\nu - 2) + A_2(11\nu - 5)}{2(1 - 2\nu)} \quad (2.10)$$

Following the investigations described in Refs. [2.15,2.16,2.19,2.39,2.45 – 2.47], using the experimental compression-force vs. displacement rigid flat-ended cylindrical-punch data reported in Ref. [2.49] and the finite-element/optimization procedure described in Appendix, A_1, A_2 and m were determined and respectively assigned the following values: 1.65 *kPa*, 3.35 *kPa* and 0.49.

Stress (more precisely, the second Piola–Kirchhoff stress tensor, S) is obtained by differentiating the strain energy function W with respect to the right Cauchy–Green strain tensor, C, as:

$$S = 2\frac{\partial W}{\partial C} \tag{2.11}$$

The (true) Cauchy stress, σ, can then be computed from the corresponding second Piola–Kirchoff stress, S, using the following component-form relation:

$$\sigma_{rk} = F_{ri} S_{ij} F_{kj} J^{el-1} \tag{2.12}$$

II. 2.3. Seated-human/seat Contact/interactions

In the seated-human/car-seat interaction analyses carried out in the present work, the shell sections of the seat are first positioned to obtain the desired seat-pan and back-rest inclination angles. Subsequently, their positions are kept fixed.

The loading present in the seated-human/car-seat interaction analyses is associated solely with the weight of the seated-human. In other words, only the distributed gravity-based body forces were used to prescribe the loading.

The interactions between the seated human and the seat, between human feet and the foot-rest as well as potential human soft-tissue and seat self-interactions are analyzed in ABAQUS/Standard using a ‘‘*penalty*” contact method within which the penetration of the surfaces into each other is resisted by linear spring forces/contact-pressures with values proportional to the depth of penetration. These forces, hence, tend to pull the surfaces into an equilibrium position with no penetration. Contact pressures between two bodies are not transmitted unless the nodes on the “*slave surface*” contact the ‘‘*master surface*”. There is no limit to the magnitude of the contact pressure that could be transmitted when the surfaces are in contact. Transmission of shear stresses across the contact interfaces is defined in terms of a static and a kinetic/sliding friction coefficient and an upper-bound shear stress limit (a maximum value of shear stress which can be transmitted before the contacting surfaces begin to slide). A typical seated-human/car-seat configuration analyzed in the present work is shown in Figure 2-6.

As mentioned earlier, all the calculations in the present work were done using ABAQUS/Standard [2.50]. A typical quasi-static computational analysis of the seated-human/car-seat interactions carried out on a 64 bit Windows XP based PC with two quad-core 2.83 *GHz* Xenon processors (eight total cores) and 8 GB of RAM required ca. 30 min of wall-clock time.

II.2.4. Seated-human/car-seat Model Validation

To validate the present model for the seated-human/car-seat assembly, the computational results obtained in the present work related to the distribution of pressure over the human/seat contact interface as well as the size and shape of this interface are compared with their experimental counterparts reported in Ref. [2.23]. Toward that end, the seat-pan has been replaced with a cubical-shaped foam block with the dimension is $L \times W \times H = 400\ mm \times 400\ mm \times 60\ mm$. The seat-pan is divided in three through-the-thickness layers and each layer meshed using eight-node first-order solid elements with the dimensions $L \times W \times H = 25\ mm \times 25\ mm \times 20\ mm$. In this way, the size of the upper-face of the elements was made equal to the size of the pressure plates used in the experiments required in Ref. [2.23]. In Ref. [2.23], a 16 × 16 sensor pressure-mapping system with a sampling rate 3072 readings per second and a calibrated pressure range of 0–200 *mmHg* was used.

Figure 2-6. A typical configuration of the seated-human/car-seat assembly used in the present work.

An example of the comparison of the computational and the experimental results from Ref. [2.23] is displayed in Figure 2-7a and b. Due to copyright restrictions, the experimental results reported in Ref. [2.23], had to be read-off from this reference and re-plotted Figure 2-7a. A comparison between the results presented in Figures 2-7a and b suggest that there is a quite good agreement between the experimental findings and the present modeling approach. Specifically, in both cases the maximum pressure is around 30 *kPa* and it is located under the ischial tuberosities while the over-all size and shape of the contact-surface patches are quite comparable. Thus, to a first order of approximation, the present model can be relied on for further investigation of seated-human/car-seat interactions.

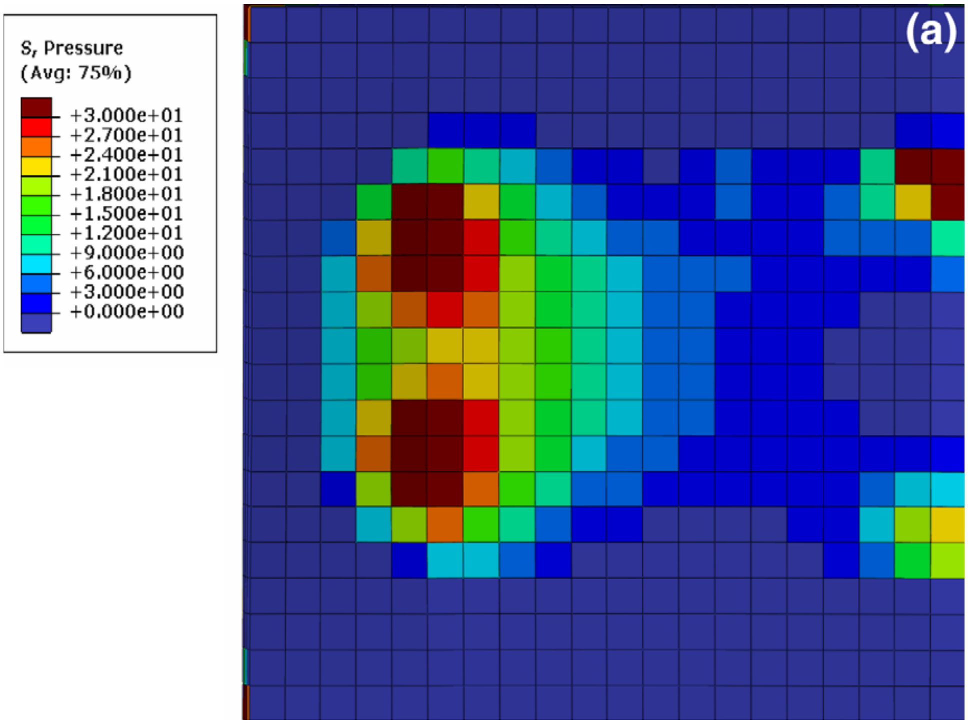

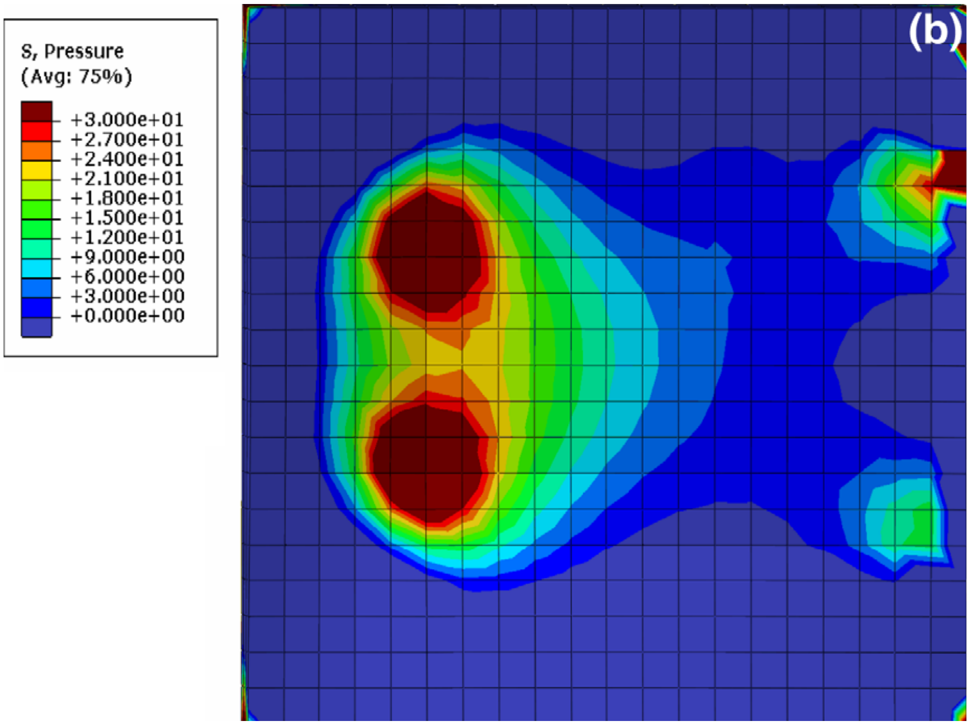

Fig. 2-7. A comparison between the contact pressure distribution over the seat-pan top surface obtained: (a) experimentally, in Ref. [1.23] and (b) computationally, in the present work.

II.3. RESULTS AND DISSCUSSION

The car-seat and the seated-human finite element models (as well as the seat-cushion and the human soft-tissue material models) developed in the present work and reported in the previous section and in the Appendix enable preliminary investigation of comfort of the seated human. Two specific seating postures were considered: (a) a seating posture in which the feet of the human were supported by the foot rest (referred to as the ‘‘supported feet case”), and (b) a seating posture where the feet were not supported by the foot rest (referred to as the ‘‘*dangling feet case*”). The results of this preliminary investigation are presented in the remainder of this section.

II.3.1. Contact-pressure Distribution and Contact Patch(es) Size/shape

As stated earlier, distribution of the contact pressure over the seated human/car-seat contact interface is an important factor in controlling seating comfort. Typical distributions of the contact pressure in the supported feet and dangling feet cases are shown in Figures 2-8a and b, respectively. The results displayed in these figures can be related to the seating comfort in the following ways: (a) the magnitude and the location of the maximum contact pressure can be determined. As was expected, the results displayed in Figure 2-8a show that the maximum pressure in the supported feet case was located at *ischial tuberosities* (a rounded protuberance associated with the lowest of the three pelvis bones), while Figure 2-8b shows that the maximum pressure in the dangling feet case was centered on the mid-span of the hamstring. Also, it should be noted that contact pressures are lower in the supported feet case; (b) the distribution of the pressure over the contact interface. It is well established that lower maximum contact pressure and more uniform distribution of the pressure over the human-body/car-seat contact area imply improved seating comfort; (c) the size and (d) the shape/symmetry of the contact area. Larger and more symmetric contact surface(s) are associated with increased seating comfort, in general.

II.3.2. Distribution of Contact Shear Stresses

As pointed out earlier, conventional experiments aimed at quantifying the interactions between a seated human and a car seat can only deal with normal contact stresses. However, contact shear stresses can also develop at the contact interface(s) (particularly in the case when the backrest is reclined backward and the human is leaning against it). It is commonly known that prolonged exposure to contact shear stresses can

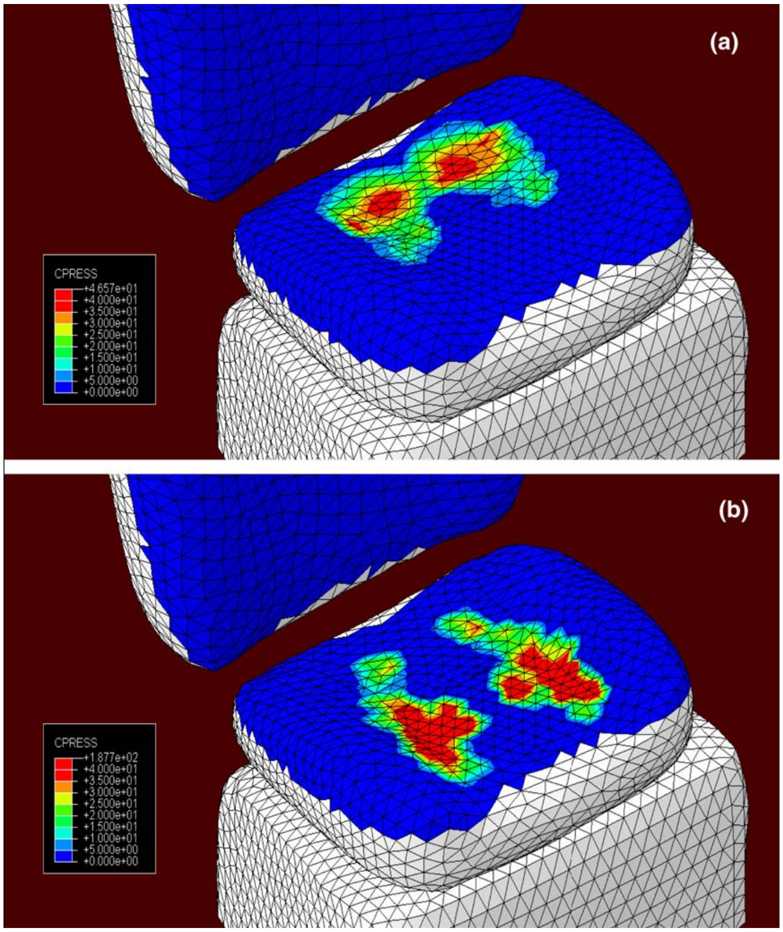

Figure 2-8. Typical contact pressure distribution over the human-body/car-seat interface for the case of a seat-human with: (a) supported feet and (b) dangling feet.

cause soft-tissue trauma in wheel-chair bound disabled people, elderly or diabetic patients. In these individuals, the consequences of soft-tissue trauma can be quite severe and can lead to ulcers and tissue necrosis. While healthy individuals with proper skin sensation generally change their position/posture before significant tissue trauma occurs, contact shear stresses clearly contribute to the perception of seating discomfort in these individuals.

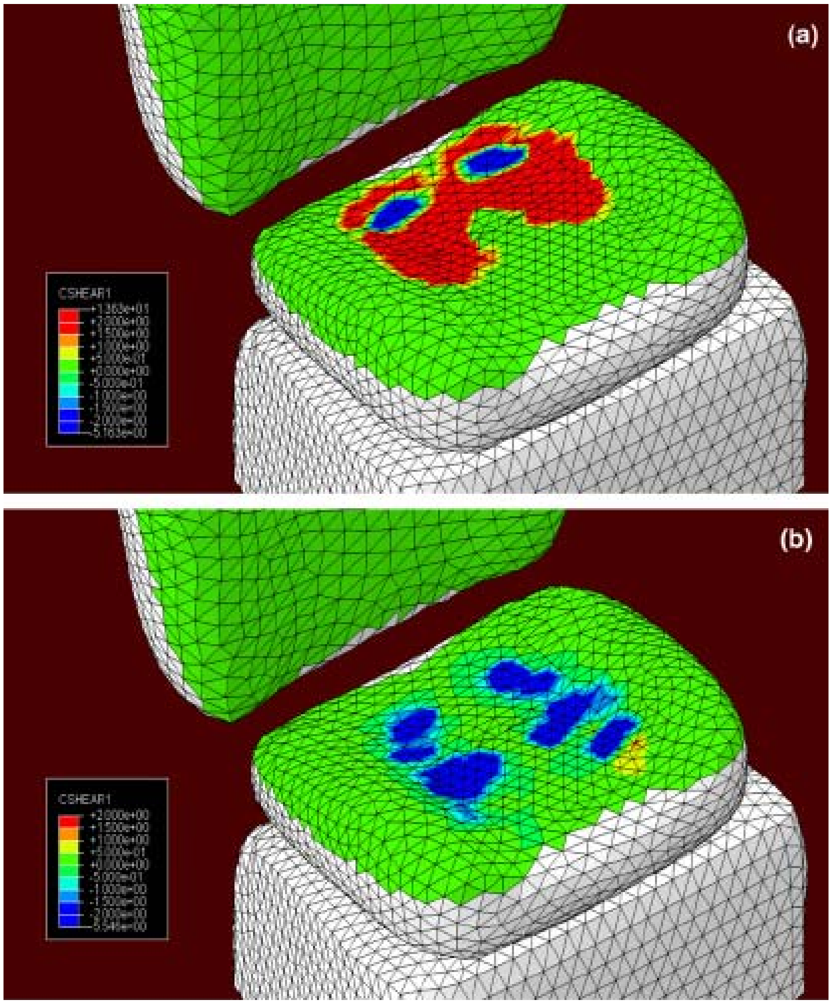

Figure 2-9. Typical contact shear stress distribution over the human-body/car-seat interface for the case of a seat-human with: (a) supported feet and (b) dangling feet.

Typical distributions of the longitudinal contact shear stress in the supported feet and dangling feet cases are shown in Figures 2-9a and b, respectively. It should be noted that the results displayed in Figures 2-9a and b were obtained under the constant static friction coefficient condition of 0.5 (corresponding roughly to the case of a clothed human body sitting on a fabric upholstered car seat.) Clearly, in the absence of friction, no contact shear stresses can be developed at the seated-human/car-seat interface. In should be further observed that somewhat higher longitudinal contact shear stresses exist in the supported feet case, the case for which the contact normal stresses were found to be lower.

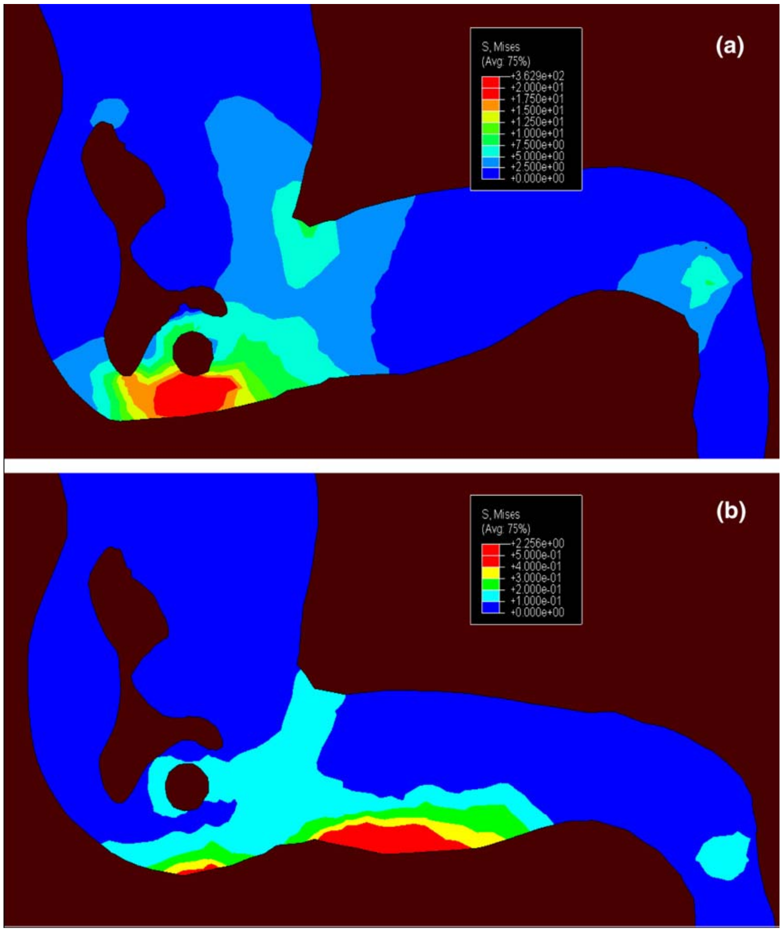

Figure 2-10. Distributions of the von Mises equivalent stress over a section-cut along a sagittal (x-y) plane through the left ischial tuberosity for the case of a seat-human with: (a) supported feet and (b) dangling feet.

II.3.3. Stresses Within the Human Body

The results presented in the previous two sections deal with contact normal and shear stresses, i.e. with the stresses present at the seated-human/car-seat contact interfaces. It is generally recognized that not only these contact stresses but also the stresses distributed within the human body in the regions adjacent to the contact interface can greatly contribute to the perception of seating discomfort. While at the present time these in-body stresses cannot be measured experimentally, they can be readily computed using finite element analyses of the human-body/car-seat interactions, like the one developed in the present work. Examples of the computed results of in-body stresses are displayed in Figures 2-10 – 2-12. In these figures, the distribution of von Mises equivalent stress over three vertical sections of the human body model is displayed for two seating posture cases. The results displayed in Figures 2-10a and b correspond to the case of a section-cut along a *sagittal (x-y)* plane through the left *ischial tuberosity*. A comparison of the results displayed in Figure 2-10a and b reveals that the in-body stresses are somewhat higher and concentrated around the ischial tuberosity in the supported feet case. While, in the dangling feet case, the stresses are mainly localized under the hamstring. Figures 2-11a and b correspond to the case of a sagittal plane cut through the coccyx (the tailbone, i.e. the final segment of the human vertebral column). The results displayed in these Figures show relatively low levels of the in-body stresses. This is justified by the fact that there is limited contact between the human soft tissue just below the *coccyx* and the seat pan, in both seating postures. Figures 2-12a and b display the case of a *coronal (y-z)* plane cut through the *ischial tuberosities*. A comparison of the results displayed in Figures 2-12a and b reveal significantly higher in-body stresses for the case of supported feet. This finding is reasonable considering the fact that in the supported feet case the majority of the human upper-body weight is supported by the contact interfaces located directly below the *ischial tuberosities*.

Again, it should be recalled that within the coordinate system chosen, *x*-axis is pointing forward, *y*-axis upward, and *z*-axis from left to right.

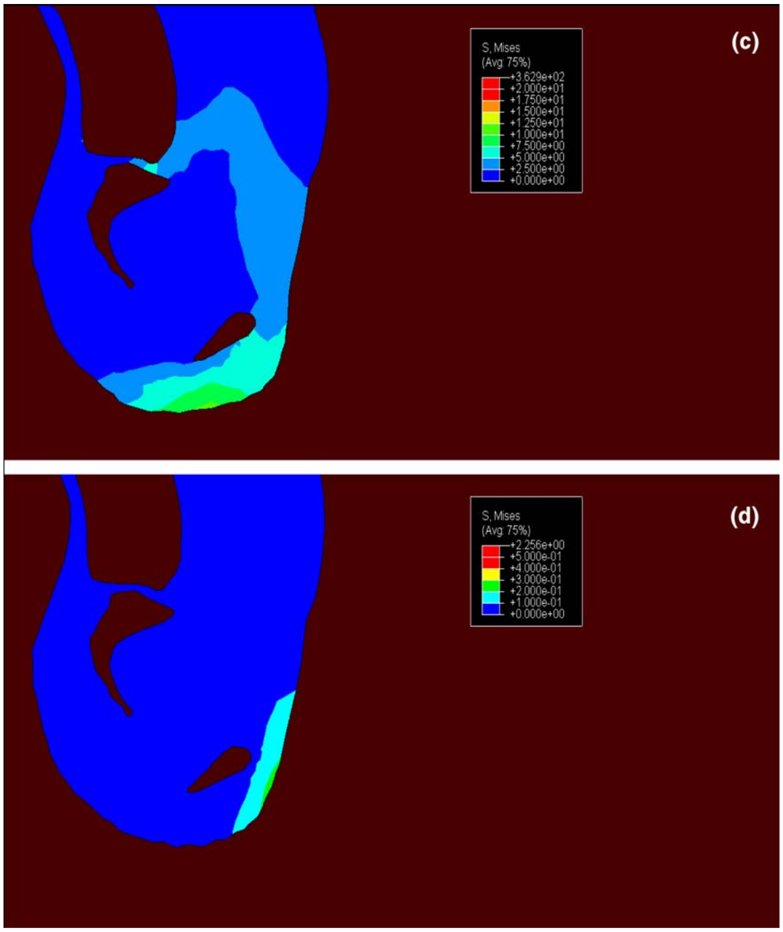

Figure 2-11. Distributions of the von Mises equivalent stress over a sagittal plane cut through the coccyx for the case of a seat-human with: (c) supported feet and (d) dangling feet.

II.3.4. Seating Comfort Evaluation

To make the results displayed in Figures 2-8 – 2-12 useful, they should be compared with the (subjective) corresponding results of the human-subjects’ perception of the seating comfort. In such studies, the human-body model should be customized in order to most accurately describe the stature, physical build, weight, and the physical condition of the human test subject in question. This can be done through proper scaling of the generic human-body model like the one developed in the present work.

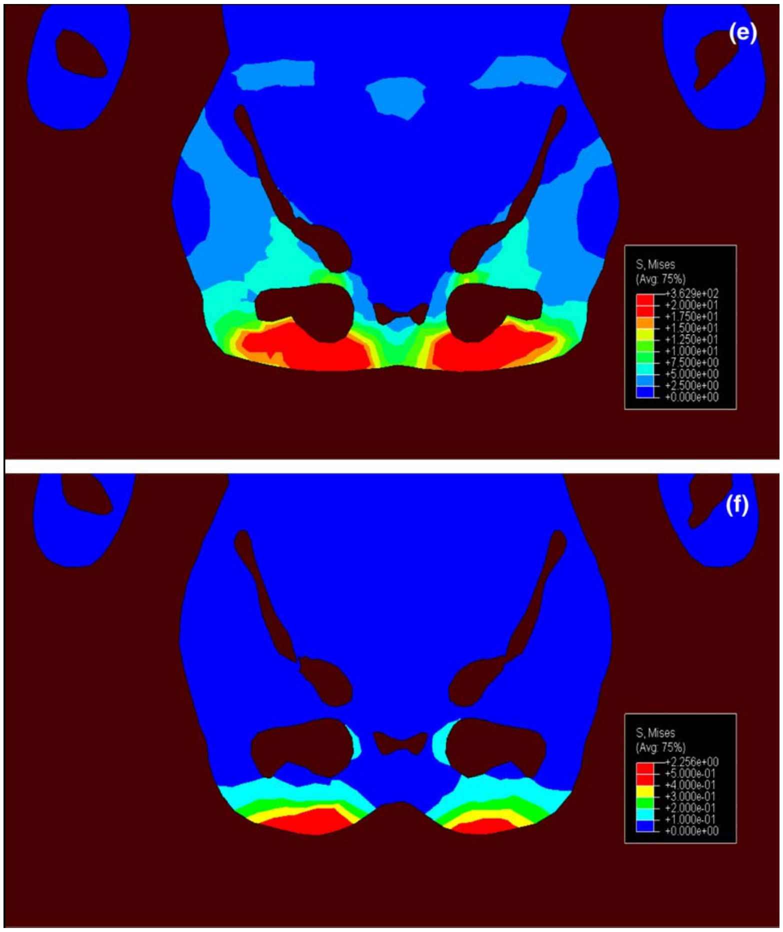

Figure 2-12. Distributions of the von Mises equivalent stress over a coronal (y–z) plane cut through ischial tuberosities for the case of a seat-human with: (e) supported feet and (f) dangling feet.

It should be noted that, as mentioned earlier, maximum muscle activity also contributes to the perception of comfort. That is, if the voluntary muscle forces (controlled by the human central nervous system) required to maintain the given seating posture of the human are higher, then there will be an increased perception of discomfort. At the present time muscles are not treated as contractile actuation elements within the finite element models, like the one developed in the present work. However, muscle activities can be computed via the use of musculoskeletal multi-body dynamics programs like AnyBody Modeling System [2.25]. An example of the muscle activation results which can be obtained through the use of the AnyBody Modeling System is shown in Figure 2-13. In Figure 2-13, muscles are depicted as purple-grey lines while the extent of muscle activation can be denoted pictorially by the extent of muscle bulging. The results shown in Figure 2-13 were generated in our ongoing musculoskeletal investigation of seating comfort [2.51]. The two computational approaches to seating comfort analysis, i.e. the finite-element approach and the musculoskeletal multi-body dynamics approach, will be combined in our future work to construct a seating comfort metric. The starting point in this effort will be the so-called discomfort function proposed by Rasmussen and de Zee [2.31] which combines properly-weighted squared total shear force between the seat-pan and the human buttocks and the maximum muscle activity.

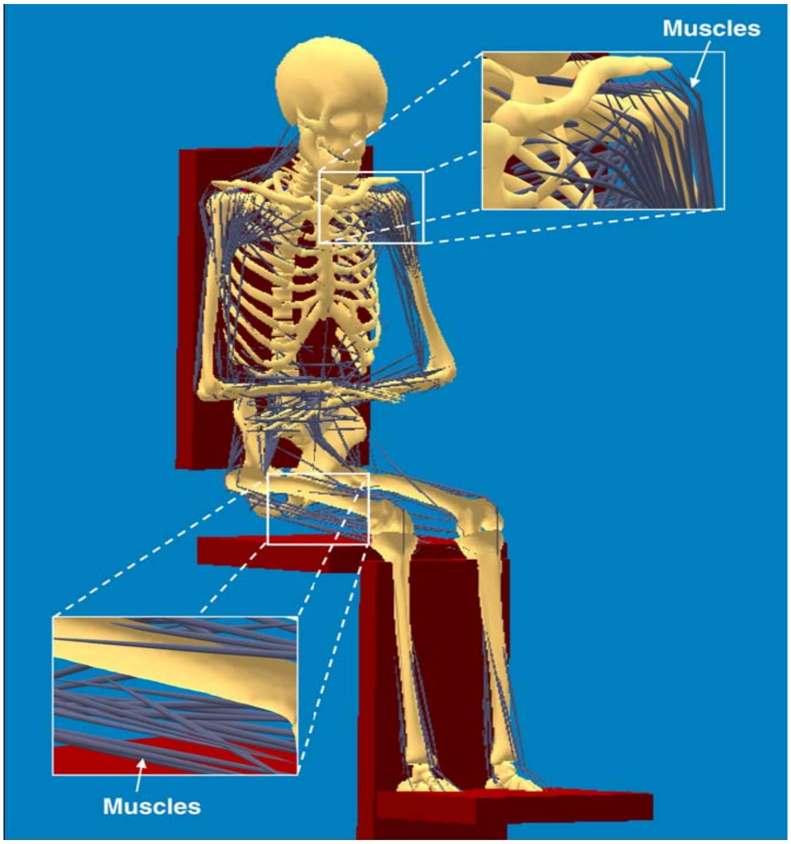

Figure 2-13. A musculoskeletal model used in the ongoing AnyBody System Modeling investigation of seating comfort [1.51].

II.4. SUMMARY AND CONCLUSIONS

Based on the results obtained in the present work, the following main summary remarks and conclusions can be drawn:

1. In order to investigate seated-human/car-seat interactions and their effect on human perception of seating comfort and fatigue, fairly detailed and anatomically correct finite element models have been developed for an average male human body and for a prototypical car seat.

2. One of the critical steps in development of the human-body model was a material-modeling of human soft tissue (skin, muscle and fat). This was accomplished through the use of a simple optimization procedure in conjunction with experimental and computational results pertaining to the force vs. displacement curves obtained in flat-head cylindrical rigid-punch indentation tests.

3. The seated-human/car-seat assembly was validated by matching the available contact pressure experimental results from the literature with the computational results obtained in the present work.

4. A computational finite-element investigation of the seated-human/car-seat interaction was used to compute a number of quantities (contact pressure, contact shear stresses, and in-body stresses) which can be related to the seat-occupant’s perception of seating comfort.

APPENDIX I(A). PARAMETERIZATION OF THE HUMAN SOFT-TISSUE MOONEY-RIVLIN HYPERELASTIC MATERIAL MODEL

It is well-established that human soft-tissue behaves as a non- linear hyperelastic, viscoelastic, anisotropic and inhomogeneous material. To simplify mathematical modeling of the mechanical response of human soft-tissue (while retaining the physical reality) various assumptions are often utilized. Among these assumptions the following will be employed in the present work: (a) initial isotropy; (b) local homogeneity; and (c) time-invariant (i.e. non-visco-elastic) material behavior (mainly due to a lack of reliable data).

In accordance with the assumptions listed above, soft tissue is modeled using a Mooney–Rivlin hyperelastic material model which, in accordance with Eqs. 2.4, 2.9, and (10) contains three material-dependent parameters: A_1, A_2, and v. These parameters were determined in the present work by fitting the compression- force vs. compression-strain data obtained in Ref. [2.48] (using a flat-head cylindrical rigid-punch indentation procedure) to the corresponding results obtained computationally in the present work (via the use of a finite element analysis). Details of this fitting procedure are described below.

A simple schematic of the flat-head cylindrical rigid-punch indentation soft-tissue mechanical-property characterization test is depicted in Figure 2-A1. In Figure 2-A1, the key experimental quantities are denoted as: P – indentation force, h – specimen thickness, w– depth of indentation and a – the punch radius.

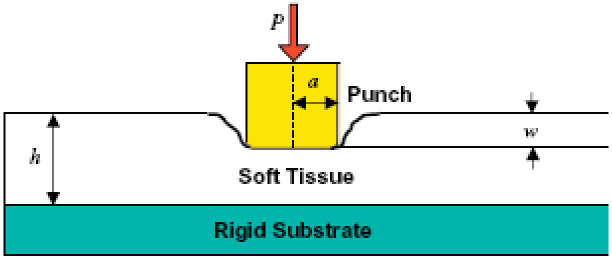

Figure 2-A1. Schematic of typical flat-head cylindrical rigid-punch indentation experiment used to determine the mechanical properties of soft tissue.

To determine the three unknown Mooney–Rivlin hyperelastic soft-tissue material parameters (A_1, A_2, and v), an axisymmetric finite element model of the flat-head cylindrical rigid-punch indentation experiment was constructed, Figures 2-A2a and b. To ensure that the finite-element results are not significantly affected by the mesh size, a mesh-convergence analysis was undertaken for each choice of material parameters A_1, A_2, and v. Additional details of the finite element procedure used are provided below. The (static) finite element analysis yielded a unique P *vs.* w/h curve. To determine the optimal values of A_1, A_2, and v, the finite-element analysis of the flat-head cylindrical rigid-punch indentation test was coupled with a simple gradient-free Nelder-Mead simplex optimization algorithm in which the sum of squares of the differences between the measure and computed indentation force, P, at a given level of indentation, w, was treated as the objective function and minimized. Additional details of the optimization procedure

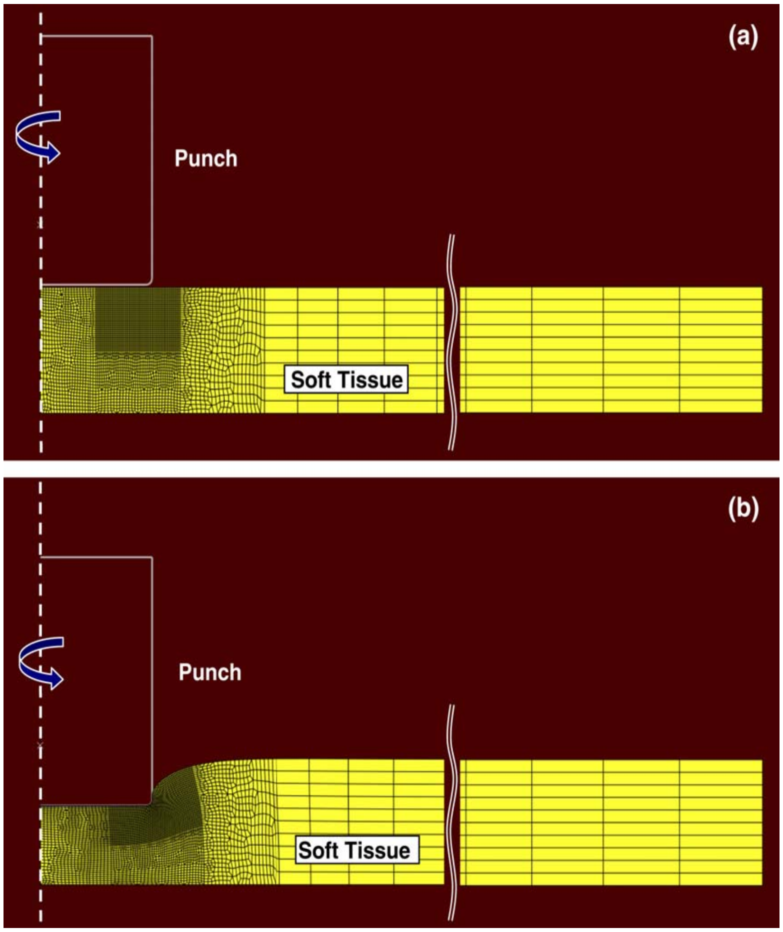

Figure 2-A2. (a) The initial, and (b) a deformed finite-element mesh used in the present investigation of the flat-head cylindrical rigid-punch indentation experiment.

used are provided below. The resulting optimal values of A_1, A_2, and v are reported in Section II.2.2. An example of the typical agreement between the experimental and the computational *P vs. w* results obtained in the present work is displayed in Figure 2-A3.

As mentioned above, the finite-element model employed in this portion of the work was two-dimensional axisymmetric and based on a finite-deformation formulation. The model was meshed using quadrilateral CAX8H and triangular CAX6H quadratic elements in order to improve the ability of the model to deform to large strains. The flat-headed cylindrical punch was modeled as a rigid body with a radius of 3 *mm* and a fillet radius of 0.2 *mm*. Punch/soft-tissue sample contact was treated as frictionless. To simulate the indentation test, a vertical displacement was prescribed, and the corresponding reaction force at the punch reference node was calculated. The bottom surface of the soft-tissue sample was constrained in the vertical direction to account for testing on a hard substrate and assigned a frictionless-type contact/boundary condition. Only the loading behavior of the soft-tissue material was investigated and, hence, the dissipative components of the response were neglected.

As mentioned above, to carryout model parameterization (i.e. parameter identification), an iterative inverse finite-element problem was constructed so that the unknown material-model parameters are determined from the condition that a satisfactory agreement is attained between model-predicted and experimentally-measured load vs. nominal strain curves. Clearly, parameter identification is an optimization problem in three-dimensional $A_1 – A_2 – v$ parameter space with the objective function (to be minimized) being the mean squared error (MSE) between the modeled and experimental force vs. nominal strain curves. Optimization was carried out by coupling HyperStudy computer software from Altair Engineering [2.52] with ABAQUS/Standard. To increase the likelihood of finding the global solution, rather than a local minimum, the optimization algorithm was employed using different initial points in the parameter space. An optimization termination condition was defined as either a maximum of 1000 iterations or the normalized simplex diameter smaller than 0.0001. A typical parameter identification analysis carried out on a 64 bit Windows XP based PC with two quad-core 2.83 *GHz* Xenon processors (eight total cores) and 8 *GB* of RAM required ca. 40 *min* of wall-clock time.

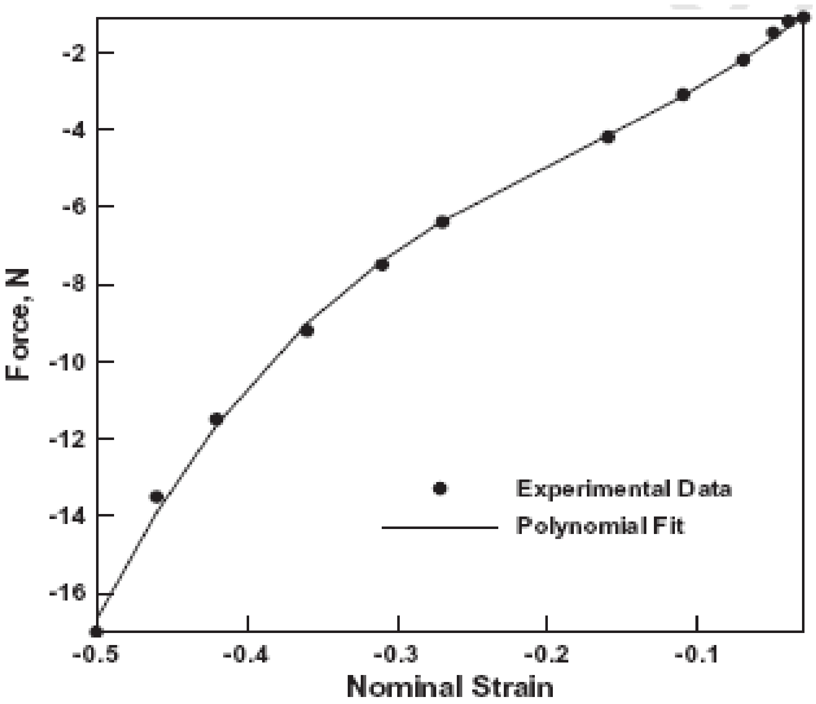

Figure 2-A3. Typical agreement between the experimental and the computational results pertaining to the flat-head cylindrical rigid-punch indentation experiment.

REFERENCES

[2.1]. U. Johansen, A, Johren, “*Personalekonomi idag,*” Uppsala Publishing House, ISBN: 9170052026, 2002.

[2.2]. K. Ebe, M. J. Griffin, “*Factors effecting static and seat cushion comfort,*” Ergonomics**,** 2001; 41(10):901–92.

[2.3]. H. Inagaki, T. Taguchi, E. Yasuda, Y. Iizuka, “*Evaluation of riding comfort: from the viewpoint of interaction of human body and seat for static, dynamic and long time driving,*” In: SAE conference, SAE no. 2000-02-0643; 2000.

[2.4]. K. Kamijo, Tsujimura H, Obara H, M. Katsumata, “*Evaluation of seating comfort,*” In: SAE conference, no. 820761; 1982.

[2.5]. J. Lee, T. Grohs, M. Milosic, “*Evaluation of objective measurement techniques for automotive seat comfort,*” In: SAE conference, SAE no. 950142; 1995.

[2.6]. A. Milvojevich, R. Stanciu, A. Russ, G. R. Blair, J. D. van Heumen, “*Investigating psychometric and body pressure distribution responses to automotive seating comfort,*” In: SAE conference, SAE no. 2000-01-0626; 2000.

[2.7]. S. J. Park, C. B. Kim, “*The evaluation of seating comfort by objective measures,*” In: SAE conference, SAE no. 970595; 1997.

[2.8]. S. J. Park, Y. S. Lee, Y. E. Nahm, J. W. Lee, J. S. Kim, “*Seating physical characteristics and subjective comfort: design considerations,*” In: SAE conference, SAE no. 980653; 1998.

[2.9]. M. P. Reed, M. Saito, Y. Kakishima, N. S. Lee, L. W. Schneider, “*An investigation of driver discomfort and related seat design factors in extended-duration driving,*” In: SAE conference, SAE no. 910117; 1991.

[2.10]. V. K. Tewari, N. Prasad, “*Optimum seat pan and back-rest parameters for a comfortable tractor seat,*” Ergonomics 2000; 43(2):167–86.

[2.11]. K. Thakurta, D. Koester, N. Bush, S. Bachle, “*Evaluating short and long term seating comfort,*” In: SAE conference, SAE no. 950144; 1995.

[2.12]. K. Uenishi, K. Fujihashi, H. Imai, “*A seat ride evaluation method for transient vibrations,*” In: SAE conference, SAE no. 2000-01-0641; 2000.

[2.13]. M. H. Yun, L. Donjes, A. Freivalds, "*Using force sensitive resistors to evaluate the driver seating comfort,*" Adv Ind Ergon Safety IV 1992:403–10.

[2.14]. L. Q. Zhao, Q. S. Xia, X. T. Wu, "*Study of sitting comfort of automotive seats,*" SAE conference, SAE no. 945243; 1994.

[2.15]. D. L. Bader, P. Bowder, "*Mechanical characteristics of skin and underlying tissues in vivo,*" Biomaterials 1980; 4:305–8.

[2.16]. C. W. J. Oomens, E. M. H. Bosboom, O. F. J. T. Bressers, C. V. C. Bouten, D. L. Bader, "*Can loaded interface characteristics influence strain distribution in muscles adjacent to bony prominences,*" Comput Methods Biomech Eng 2003;6(3):171–80.

[2.17]. D. L. Bader, P. Bowder, "*Ischial pressure distribution under the seated person,*" In: Bader DL, editor. Pressure stores – clinical practice and scientific approach; 1990. p. 223–33.

[2.18]. L. Bennett, D. Kauver, B. Y. Lee, F. A. Trainor, "*Shear vs. pressure as causative factors in skin blood flow occlusion,*" Arch Phys Med Rehab 1979;60:309–14.

[2.19]. W. W. Chow, E. I. Odell, "*Deformation and stresses in soft body tissues of a sitting person,*" J Biomech Eng 1978; 100:79–87.

[2.20]. T. A. Krouskop, S. L. Garber, P. Noble, "*Pressure management and the recumbent person,*" In: Bader DL editor. Pressure sores – clinical practice and scientific approach; 1990. p. 235–48.

[2.21]. S. M. Reichel, "*Shear force as a factor in decubitus ulcers in paraplegics,*" J Am Med Assoc 1958; 166:762–3.

[2.22]. J. Scales, "*Pressure sore prevention,*" Care Sci Pract 1982; 1:9–17.

[2.23]. M. M. Verver, J. van Hoof, C. W. Oomens, J. S. Wismans, F. P. Baaijens, "*A finite element model of the human buttocks for prediction of seat pressure distributions,*" Comput Methods Biomech Biomed Eng 2004;7:193–203.

[2.24]. M. Langsfeld, A. Frank, D. L. van Deursen, P. Griss, "*Lumbar spine curvature during office chair sitting,*" Med Eng Phys 2000;22:665–9.

[2.25]. *AnyBody 3.1*. Aalborg, Denmark: AnyBody Technology A/S; 2008.

[2.26]. M. Damsgaard, J. Rasmussen, S. T. Christensen, E, Surma, M. de Zee, “*Analysis of musculoskeletal systems in the anybody modeling system,*” Simulat Model Pract Theory 2006;14:1100–11

[2.27]. A. C. Mandal, “*The seated man (homosedens) – the seated work position: theory and practice,*” Appl Ergonom 1984; 12:19–26. 736

[2.28]. A. C. Mandal, “The influence of furniture height on back pain,” Behav Inform Technol 1987; 6:347–52.

[2.29]. D. Karlsson, A. L. Osvalder, J. Rasmussen, “*Towards better seating design – a discussion and comparison between office chairs and car seats,*” In: Proceedings of the 39th nordic ergonomics society conference, Sweden; 2007.

[2.30]. J. Rasmussen, M. de Zee, S. Torholm, “*Muscle relaxation and shear force reduction may be conflicting: a computational model of seating,*” In: SAE conference, SAE no. 2007-01-2456; 2007.

[2.31]. J. Rasmussen, M. de Zee, “*Design optimization of airline seats,*” In: SAE conference, SAE no. 2008-01-1863; 2008.

[2.32]. J. Rasmussen, S. Torholm, M. de Zee, “*Computational analysis of the influence of seat pan inclination and friction on muscle activity and spinal joint forces,*” Int J Ind Ergonom 2009; 39:52–7.

[2.33]. T. Brosch, M. Arcan, “*Modeling the body/chair interaction – an integrative experimental–numerical approach,*” Clin Biomech 2000; 15:217–9.

[2.34]. P. A. Dabnichki, A. D. Crocombe, S. C. Hughes, “*Deformation and stress analysis of supported buttock contact,*” Proc Inst Mech Eng. J Eng Med 1995;208:9–17.

[2.35]. B. A. Todd, J. G. Thacker, “*Three dimensional computer model of human buttocks in-vivo,*” J Rehab Res Dev 1994; 31(2):111–9.

[2.36]. B. Besnault, H. Guillemot, S. Robin, F. Lavaste, “*A parameteric finite element (FE) model of the human pelvis,*” In: Proceedings of the 42nd STAPP car crash conference, SAE no. 983147. p. 33–46.

[2.37]. J. Hoof, R. van Happee, R. Meijer, R. Bours, “*MADYMO FE human body model for automotive impact conditions,*” In: Proceedings of the JSAE spring convention, no. 20015336; 2001.

[2.38]. E. Lizee, S. Robin, E. Song, N. Bertholon, J. Y. Le coz, B. Besnault, “*Development of a 3D finite element (FE) model of the human body,*” In: Proceedings of the 42nd STAPP car crash conference, SAE no. 983152.

[2.39]. Moens, Horvath, “*Using finite element models of the human body for shape optimization of seats: optimization material properties,*” In: Proceedings of the international design conference, Dubrovnik, Yugoslavia; 2002.

[2.40]. *CATIA V5,* Vélizy-Villacoublay, France: Dassault Systemes Inc.; 2009.

[2.41]. *HyperWorks 9.0*. Troy (MI, USA): Altair Engineering Inc.; 2009.

[2.42]. *AnyScript Model Repository 7.1*. AnyBody 3.0. Aalborg, Denmark: AnyBody Technology A/S; 2009.

[2.43]. F. Summer. Model no. 1045, www.3Dcadbrowser.com, Hampshire (UK): 3D Club; 2009.

[2.44]. F. M. Hendricks, D. Brokken, C. W. J. Oomens, F. P. T. Baaijens, J. B. A. M. Horsten, “*A numerical–experimental method to characterize the non-linear mechanical behavior of human skin,*” Skin Res Technol 2003; 9:274–83.

[2.45]. D. Adams, G. B. Morgan, T. Nghi, M. J. Salloum, T. O’Bannon, “*Creating a biofidelic seating surrogate,*” In: SAE conference no. 1999-01-0627; 1999.

[2.46]. E. M. H. Bosboom, M. K. C. Hesselink, C. W. J. Oomens, C. V. C. Bouten, M. R. Drost, F. P. T. Baaijens, “Passive transverse mechanical properties of skeletal muscle under in-vivo compression,” J Biomech 2001; 34:1365–8.

[2.47]. R. S. Setyabudhi, A. Ali, R. P. Hubbard, C. Beckett, R. C. Averill, “*Measuring and modeling of human soft tissue and seat interaction,*” In: SAE conference, SAE no. 970593; 1997.

[2.48]. ASTM D 3574 Document Information, “*Standard test methods for flexible cellular materials—slab, bonded, and molded urethane foams,*” ASTM International; July 1, 2008.

[2.49]. M. Zhang, Y. P. Zheng, A. F. Mak, "*Estimating the effective young's modulus of soft-tissues from indentation tests – nonlinear finite element analysis of effects of friction and large deformation,*" Med. Eng. Phys. 1997; 19:512–7.

[2.50]. *ABAQUS version 6.8-1*. User documentation. Dassault Systems; 2008.

[2.51]. Grujicic M. Clemson University; February 2009 [Work in Progress].

[2.52]. *HyperStudy user manual*. Troy (MI): Altair Engineering Inc.; 2009.

CHAPTER THREE

MUSCULOSKELETAL COMPUTATIONAL ANALYSIS OF THE INFLUENCE OF CAR-SEAT DESIGN/ADJUSTMENTS ON LONG-DISTANCE DRIVING FATIGUE

ABSTRACT

The main causes for long-distance driving fatigue experienced by vehicle drivers is investigated computationally using musculoskeletal modeling and simulation methods. A rigid-body model of a prototypical adjustable car-seat is constructed as a part of the present work and combined with a public-domain musculoskeletal model of a seated human. Seated-human/car-seat interactions associated with typical seating postures of the vehicle driver are analyzed using the inverse-dynamics approach while the “minimum-fatigue” criterion is utilized to deal with the muscle-redundancy problem (i.e. with the problem that human body contains more muscles than what would be typically needed to drive various body joints).

The results obtained show that various seat adjustments (e.g. back-rest inclination, seat-pan horizontal track position, etc.), driver’s back supports (e.g. presence/absence of lumbar support) and the nature of seat upholstery (e.g. fabric vs. vinyl) can have complex influence on the muscle activation, joint forces, soft-tissue contact normal and shear stresses, all of which not only affect the comfort perception of the driver but also their feel of fatigue. Subsequently, the results of the present work along with relevant public-domain literature findings (e.g. subjective driving-fatigue assessments provided by

human test subjects and human-body/seat contact-force measurements) are used to construct a preliminary long-distance driving-fatigue function.

III.1. INTRODUCTION

Today, in the industrialized world, sitting is the most common working posture and perhaps the most frequent leisure posture. It is well-recognized that constrained sitting postures can lead to discomfort and health disorders (e.g. back pain, neck-shoulder complaints, etc.) causing a major cost to the society through missed work and reduced work-effectiveness/productivity [3.1]. Consequently, furniture manufacturers and car-seats manufacturers are forced to more aggressively address seat ergonomics in order to gain a competitive edge. In the automotive industry, the ever increasing demand by the customers for vehicles with improved performance has been complimented by an equally strong demand for vehicles with improved comfort. As a result, vehicle manufacturers use car-seat/interior comfort as an important selling point and a way to distinguish themselves from their competitors. Car seats and their role in the subjective perception of long-distance driving fatigue is the subject of the present work. The state of the car-seat manufacturing industry today is that the development and introduction of new, more-comfortable car seats is based almost entirely on empiricism, legacy knowledge and extensive, time-consuming and costly prototyping and experimental/field testing. Considering the fact that Computer Aided Engineering (CAE) has made major contribution and has become an indispensible tool for many industries, one should expect that CAE should be used more aggressively by the car seat manufacturing industry in order to address the issue of seating comfort. That is, the use of computer models of human and seat and the analysis of their interactions could facilitate, speed-up and economize the process of development and introduction of new, more comfortable car seats. Specifically, in the early stages of the seat-design process, a new design can be tested for its degree of comfort by carrying out computer simulations of the seated-human interactions with the seat. However, before these computer simulations can become reliable/high-fidelity seating-comfort assessment tools, a critical problem of identifying/defining the objectives and measurable comfort-quantifying parameters/measures and the establishment of their relations with the subjective feeling of comfort/fatigue has to be solved. Among the comfort-quantifying parameters the ones most frequently cited are: (a) the average human/seat contact pressure; (b) the maximum human/seat contact pressure; (c) the human/seat contact-area size and (d) the extent of symmetry of the human/seat contact-area [3.2 – 3.14]. All these comfort-quantifying parameters are based on measurements of the distribution of human/seat contact pressure over the contact area and these measurements commonly suffer from several limitations [e.g. 3.15,3.16] (a) they are relatively difficult to perform reproducibly and with high accuracy; (b) the obtained contact-pressure distributions do not provide any information about internal stresses and deformations of the human soft tissues; (c) the contact pressure distributions measured provide only information about the normal stresses at the contact human/seat interface whereas it is well established that significant shear stresses can be present at the human/seat interface [e.g. 3.17 – 3.22]. In addition, a major deficiency of the contact-pressure distribution-measurement approach is that it does not provide any information about the level of muscular activity and about the magnitude of joint forces, two quantities which are certainly related to the seating comfort and fatigue perception.

To address some of the limitations of the contact-pressure distribution-measurement-approach, various human-body/seat coupled computer models and computational analyses have been proposed. For example, a finite-element based modeling approach was introduced by Verver et al. [3.23], a rigid-body mechanics based model was suggested by Langsfeld et al.[3.24], etc. While these approaches were able to provide estimates for some of the parameters that are either difficult or impossible to obtain via direct measurements, so far however, it has not been possible to create a model that can calculate how muscular activity and joint forces are affected by changes in sitting conditions. The main reason for this is that the human body, in general, and its muscular and skeletal systems, specifically, are quite challenging mechanical systems to model.

To address the limitations of the seating-comfort-assessment computer modeling schemes mentioned above, the AnyBody Research Group [3.25] at Aalborg University in Denmark in collaboration with three furniture manufacturers initiated recently a research project entitled ‘‘*The Seated Human*’’. The main objective of this project is to define a set of seating-comfort design criteria for chairs and to devise the means (based on rigorous computer modeling of the human musculo-skeletal system) for reliable assessment of these criteria. Within the project, the recently-developed novel technology for computer modeling of the human-body mechanics and dynamics, namely the AnyBody Modeling System [3.25] and its associated public domain library of body models are being fully utilized and further developed. In its most recent rendition [3.26], the AnyBody Modeling

System enables creation of a detailed computer model for the human body (including all important components of the musculo-skeletal system) as well as examination of the influence of different postures and the environment on the internal joint forces and muscle activity.

The earliest public-domain report related to the human body in a seated posture can be traced back to the pioneering analytical investigation conducted by Mandal [3.27, 3.28] who used simple physics-based reasoning in place of the traditional empirical and subjective approaches. The main outcome of Mandal's work was that it is beneficial from the spinal-loads reduction point of view to reduce the pelvic rotation (i.e. flexion between the pelvis and the thorax) below a normal value of 90° in the seated-human posture (by tilting the seat-pan forward and/or the backrest backward). Moreover, in a recent work carried out by Rasmussen et al. [3.29 – 3.32] it was shown that forward seat-pan inclination indeed reduces the spinal-joint loads. However, it may also increase the maximum muscle activity (i.e. muscle fatigue) unless sufficient friction is present at the human-buttocks/seat interface in which case its spinal-joint load-reduction beneficial effect diminishes and is replaced with an comfort-compromising/harmful effect of inducing shear forces in the human soft tissue.

The main objective of the present work is to explore the capabilities of the AnyBody Modeling System in predicting the aspects of human-body/car-seat interactions which affect car-driver fatigue during long-distance driving and to device a long-distance driving-fatigue function. The issue of long-distance driving induced fatigue in drivers was addressed by Michida et al. [3.41] using laboratory and on-road tests. These tests involved subjective evaluations of fatigue provided by human test subjects as well as objective measurements obtained using contact-pressure sensor-array mats and non-invasive electromyography (EMG, a muscle activity measuring technique). The results obtained by Michida et al. [3.41] can be summarized as follows:

(a) While the interactions between human-body and the car-seat pan could contribute to seating discomfort via contact shear stresses (can in general lead to soft-tissue trauma) and via normal contact pressures, the interactions between the car-driver's back and seat back-rest tend to play a critical role in increasing long-distance driving fatigue;

(b) In general, three main back/back-rest contact conditions were identified which are conducive to long-distance driving fatigue: (i) insufficient lumbar support; (ii) insufficient thorax support and (iii) excessive thorax support; and

(c) As will be discussed in greater detail in Section III, the aforementioned three driving-fatigue controlling factors can be related to the kinematics of pelvis and lumbar and thoracic regions of the spine and with the required activities of the muscles to maintain the most comfortable seating posture.

The organization of the paper is as follows. A brief overview of the AnyBody Modeling System is provided in Section III.2.1. The musculoskeletal human-body model, the concepts of muscle recruitment and muscle activity envelope, the car-seat model and the issues related to seated-human/car-seat kinematics and contact interactions are discussed in Sections III.2.2 - III.2.6. The definition of the problem analyzed in the present work is discussed in Section III.2.7. The results obtained in the present work are presented and discussed in Section III.3. A discussion of the driving fatigue-relevant public-domain literature and the formulation of a preliminary long-distance driving-fatigue function are presented in Section III.4. The main conclusions resulting from the present work are summarized in Section III.5.

III.2. MODELING AND COMPUTATIONAL PROCEDURES

III.2.1. The AnyBody Modeling System [2.25]

The AnyBody Modeling System [3.25] developed at Aalborg University and used in the present work is a general-purpose musculoskeletal modeling and simulation program. The essential features of this computer program can be summarized as follows:

(a) The musculoskeletal model is typically constructed as a standard multi-body dynamics model consisting of rigid bodies, kinematic joints, kinematic drivers and force/moment actuators (i.e. muscles) which can be solved using standard multi-body dynamics simulation methods;

(b) Complex geometries of the muscles and their spatial arrangement/ interactions (e.g. muscles wrapping around other muscles, bones, ligaments, etc.) can be readily modeled within AnyBody Modeling System [3.25];

(c) It is well-established that a typical musculoskeletal system suffers from the so-called “muscle redundancy problem”: i.e. the number of muscles available is generally larger than those needed to drive various body joints. Within the living humans and animals, this problem is handled by their Central Nervous System (CNS) which controls muscles activation/recruitment. To mimic this role of the CNS, the AnyBody Modeling System [3.25] offers the choice of several optimization-based muscle-recruitment criteria;

(d) A typical musculoskeletal multi-body dynamics problem is solved using computationally-efficient inverse dynamics methods within which the desired motion is prescribed while the muscle activity required to produce this motion is computed;

(e) Within the AnyBody Modeling System [3.25], the muscle recruitment problem is solved using an optimization-based approach in the form:

Minimize the objective function:

$$G(f^{(M)}) \tag{3.1}$$

Subjected to the following constraints:

$$Cf = d \tag{3.2}$$

$$f_i^{(M)} \geq 0 \quad i \in \{1,\ldots,n^{(M)}\} \tag{2.3}$$

where the objective function G (a scalar function of the vector of $n^{(M)}$ unknown muscle forces, $f^{(M)}$), defines the minimization object of the selected muscle-recruitment criterion (assumed to mimic the one used by the CNS). Eq. 3.2 defines the condition for dynamic mechanical equilibrium where C is the coefficient matrix for the "*unknown*" forces/moments in the system while d is a vector of the "*known*" (applied or inertia) forces. The forces appearing in vector f in Eq. 3.2 include the unknown muscle forces, $f^{(M)}$, and the joint-reaction forces, $f^{(R)}$. Eq. 3.3 simply states that muscles can only pull (not push) and that the upper bound for the force in each muscle $f_i^{(M)}$ i corresponding muscle strength, N_i;

(f) While there are a number of functional forms for the objective function, *G*, the one most frequently used is the so-called "*min/max*" form within which the objective: function (to be minimized) is defined as the maximum muscle activity defined for each muscle *i* as $f_i^{(M)}/N_i$, i.e.:

$$G\left(f^{(M)}\right) = \max\left(f_i^{(M)} / N_i\right); \qquad (3.4)$$

This formulation offers several numerical advantages over other popular forms of *G* and, in addition, it appears to be physiologically sound. That is, under the assumption that muscle fatigue is directly proportional to its activity, Eqs. 3.1 and 3.4 essentially state that muscle recruitment is based on a minimum muscle-fatigue criterion;

(g) The problem defined by Eqs. 3.1 – 3.4 can be linearized using the so-called "*bound formulation*" [3.33] resulting in a linear programming problem with muscle forces and joint reaction forces as free variables. Relations between these two types of forces are next used to eliminate the joint reaction forces yielding a linear programming problem with the number of unknowns equal to the number of muscles in the system; and

(h) While for a fairly detailed full-body model containing around one thousand muscles, this constitutes a medium-to-large size problem which can be readily solved by a variety of design-optimization methods (e.g. Simplex, Interior-point methods, etc.), the min/max problem is inherently indeterminate and must be solved iteratively. This can be rationalized as follows: The min/max criterion only deals with the maximally-activated muscles and with muscles which help support the maximally-activated muscles. Since the system, in general, may contain muscles that have no influence on the maximum muscle activity in the system, the forces in these muscles are left undetermined by the min/max formulation presented above. To overcome this shortcoming, the muscle-recruitment optimization problem is solved iteratively, so that each iteration eliminates the muscles with uniquely determined forces and the procedure is repeated until all muscle forces are determined.

III.2.2. Musculoskeletal Human-body Model

The musculoskeletal model of the human body used in the present work was downloaded from the public domain AnyScript Model Repository [3.34]. The model was originally constructed by AnyBody Technology using the AnyBody Modeling System [3.25] following the procedure described in details by Damsgaard et al. [3.26].

Model Taxonomy: The musculoskeletal human-body model includes: (a) an arm/shoulder assembly containing 114 muscle units on each side of the body and having a morphology defined by Van der Helm [3.35], (b) a spine model developed by de Zee et al. [3.36] comprising sacrum, all lumbar vertebrae, a rigid thoracic-spine section, and a total of 158 muscles, and (c) a pelvis and lower extremity model with a total of 70 muscles. In total, the model contains more than 500 individual muscle units and, hence, can be considered as a fairly detailed description of the human musculo-skeletal system. The anthropometrical dimensions of the model are selected in such a way that they roughly correspond to a 50th percentile European male.

Segments and Joints: Within the model, the bodies (referred to as the "*segments*" within the AnyBody Modeling System) are treated as rigid with their mass/inertia properties derived from mass and shape of the associated bone and the soft tissue that is allotted to the bone. Joints in the human body are treated as idealized frictionless kinematic constraints between the adjoining segments. Both standard kinematic joints (e.g. spherical joints for the hips, hinge joints for the knees, etc.) as well as specially-developed joints (e.g. those used to represent kinematic constraints associated with floating of the scapula on the thorax) are employed.

Muscles: Muscles are treated as string contractile force –activation elements which span the distance between the *origin* and the *insertion points* through either the *via points* or by wrapping over the surfaces which stand on their way. Muscle wrapping problem is treated using a shortest-path contact-mechanics algorithm. Due to the fact that the problem considered in the present work is static, muscles are modeled as being *isometric* (i.e. muscle strength is considered as being constant rather than being a function of the body posture and the rate of contraction). For the same reason, *passive elasticity* of muscles (i.e. the resistance of the muscles to stretching) is not considered.

Model Validations: The mechanics of the model is implemented as a full three-dimensional Cartesian formulation and includes inertial body forces (in the static problem under consideration, only gravity inertial forces are present). Integral validation of whole-body musculoskeletal models is very difficult to conduct. To the best knowledge of the present authors, validation of the whole-body musculo-skeletal model is still lacking (due to major challenges which would be associated with such validation). However, various subsystems of the whole-body model were validated separately. For example: (a) The lumbar spine model was validated by de Zee et al., [3.36] by comparing the model prediction with *in vivo L4-5 intradiscal* pressure measurements of Wilke et al. [3.37]; (b) de Jong et al. [3.38] validated the lower extremity model by comparing model-predicted muscle activations and pedal forces with their experimental counterparts obtained in pedaling experiments; an (c) The shoulder model was validated in the early work of Van der Helm [3.35].

III.2.3. The Muscle Activity Envelope

As originally recognized by An et al. [3.39], the *min/max* muscle-recruitment formulation, discussed in Section III.2.1, defines effectively a *minimum fatigue criterion* as the basis for muscle recruitment, i.e. the aim of the proposed muscle-recruitment strategy is to postpone fatigue of the "*hardest-working*" muscle(s) as far as possible. The physiological consequence of this strategy is that muscles tend to form groups with muscles within the same group having comparable activity levels. In particular, in the muscle group associated with the maximum muscle activity there will be usually many muscles which, in a coordinated manner, carry a portion of the load comparable with their individual strengths. Consequently, in this group, many muscles will have the same activity level, which will be referred to as *"the muscle activity envelope*". The linearity of the reformulated *min/max* criterion discussed earlier guarantees that the optimization problem defined by Eqs. 3.1 – 3.3, is convex and, hence, that the solution to the problem is unique and corresponds to the global optimum. In other words, there is no other muscle recruitment strategy which can reduce the muscle-activity envelope further. Moreover, since the muscle activity envelope represents the maximum muscle activation in the model, it can be interpreted as the fraction of maximum voluntary contraction necessary to support the imposed load (gravity in the present case) while maintaining the prescribed posture. Thus, the muscle-activity envelope appears to be an important parameter/measure for ergonomic-design optimization, in the sense that designs which is associated with lower envelope levels may be perceived as less fatigue-inducing.

III.2.4. Car-seat Model

A rigid-body model of a prototypical seat is developed for use in the present work, Figure 3-1. The car seat model comprises of the following rigid bodies: head-rest, back-rest, seat-pan, leg-rest and the foot-rest. Revolute joints were used to enable back-rest and seat-pan inclination angle adjustment and a prismatic joint was used for seat longitudinal-track position adjustment.

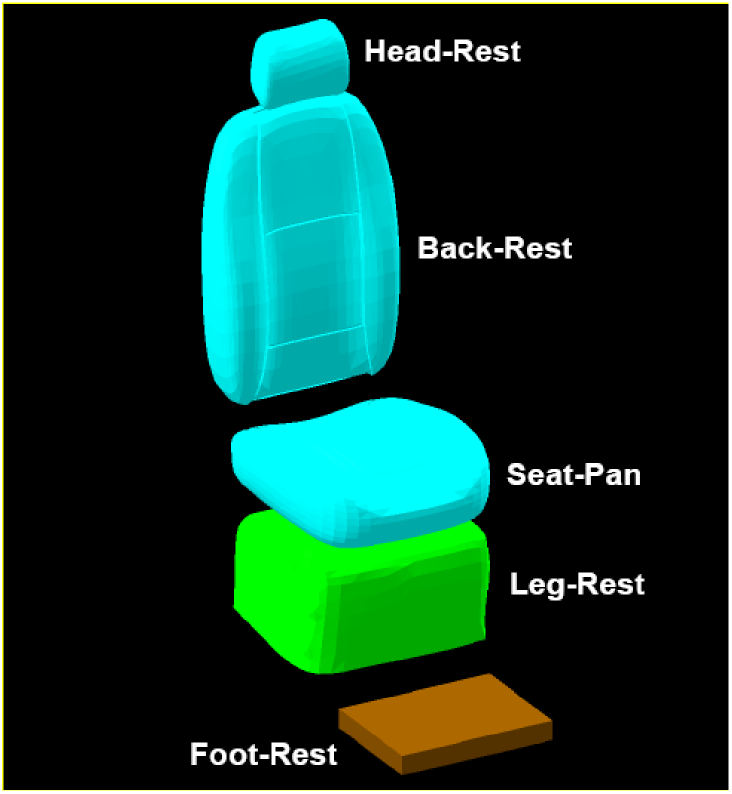

Figure 3-1. Rigid-body model for the car seat used in the present work.

To obtain the desired posture of the human for a given adjusted configuration of the car-seat (linear and angular) kinematic links were placed at the seated-human/seat contact interfaces (at the back-rest and at the seat-pan). However, these links were not allowed to transmit any forces/moments. As will be discussed below, human-body/car-seat contact forces have been accounted for through the use of "*support points*".

III.2.5. Seated-human/Car-seat Kinematics

As mentioned above, the car-seat can be adjusted, as needed, by assigning proper values to the car-seat joint degrees of freedom. Due to the presence of the human-body/car-seat kinematic links, the human body acquires the appropriate seating posture for each given set of car-seat adjustments. In the process of acquiring the appropriate seating posture, kinematics of the spine is adjusted in accordance with the so-called "*spinal rhythm*" algorithm. Within this algorithm, a single input, the pelvis-thorax angle, is used to determine the three rotational-joint angles of adjacent vertebrae (under a condition that the passive-elastic elements of the spine are able to force the spine to act kinematically as an elastic beam). The physical soundness of the spinal-rhythm algorithm for the seating posture has been validated by Rasmussen and de Zee using motion capture experiments [3.32].

In acquiring the seated position for the human, an additional algorithm was employed. This algorithm controls the relative magnitudes of hip flexion and pelvis/thorax flexion. Following the experiments of Bell and Stigant [3.40], the ratio of the two angles was set to 2. That is, for a given value of the angle between the thorax and the thigh, the hip-joint flexion angle is twice that of the spine flexion angle.

III.2.6. Seated-human/Car-seat Contact Interactions

To quantify the extent of and to account for the distributed nature of the human-body/car-seat contact interactions, a number of support points are introduced over the back-rest, seat-pan and the foot-rest surfaces. These support points allow the transfer of reaction forces to the car-seat support elements. To quantify the contact reaction forces at the support points, the so-called "*supporting elements*" are used which can provide compressive reaction forces, R_i, (i is the support-element number) and tangential/friction forces, F_{fi}, (the maximum values of which is μR_i, where μ is the (input) friction coefficient. It should be noted that the compressive reaction forces are perpendicular to the support surfaces while tangential force can be in any direction perpendicular to the corresponding compressive force.

The reaction forces R_i and F_{fi} are unknown for a given seating posture and must be determined. However, due to the fact that a large number of support points were added in order to assess the distribution of contact forces over the seated-body/car-seat contact interfaces, the problem is made statically indeterminate and the solution cannot be obtained by simply solving the mechanical equilibrium equations. To overcome this problem, the unknown contact forces, R_i , are normalized using a large value of the "*artificial-muscle*" strength, N_i, and added to the vector of unknown forces fi in Eq.3.2. The seated-human/car-seat contact forces are then obtained by invoking the same muscle-recruitment algorithm discussed in Section III.2.1. This approach, thus, treats the human-body/car-seat contact problem as follows: (a) the human body is postulated to use the available support points at the backrest, seat-pan and the foot-rest to minimize its muscle activity and (b) by choosing a large value of the artificial-muscle strength, the supporting elements are prevented from dominating the anatomic-muscle recruitment process.

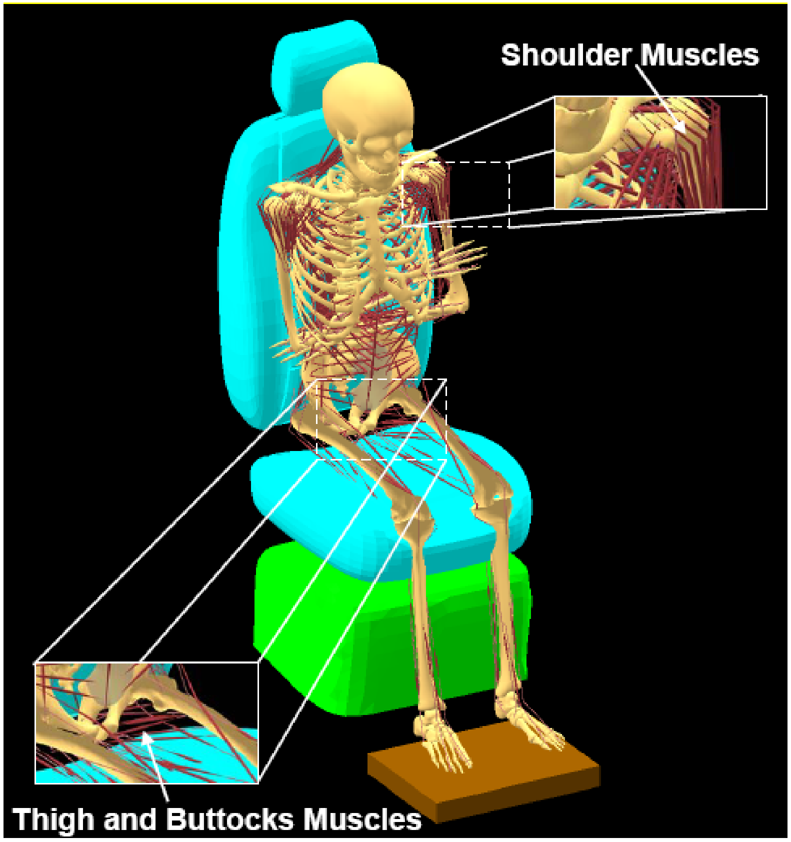

Figure 3-2. The musculoskeletal model of a human sitting in the car-seat developed in the present work.

III.2.7. Problem Definition

To analyze long-distance driving fatigue, the human-body model reviewed in Section III.2.2 is first placed in the car-seat described in Section III.2.4. Two additional environment segments are then added, one representing the brake pedal/accelerator assembly while the other representing the steering column. Then the human-body was repositioned in accordance with a typical posture associated with vehicle driving. This involved placing the driver's hands on the steering wheel, positioning of his right foot on the accelerator pedal while having his left foot resting on the foot-rest/vehicle-floor. In addition, neck flexion was adjusted to ensure straight-forward vision of the driver. A typical driving posture used in the present work is displayed in Figures 3-3(a)-(b). To improve clarity, human-body muscles are not shown in Figures 3-3(a)-(b). To mimic the reaction moment experienced by the driver's right foot during the act of acceleration, a 20*Nm* contact moment is applied to the right-foot/accelerator pedal revolute joint. Where applicable, to account for the presence/absence of lumbar support, the support points on the lumbar-section of the spine were added/removed accordingly.

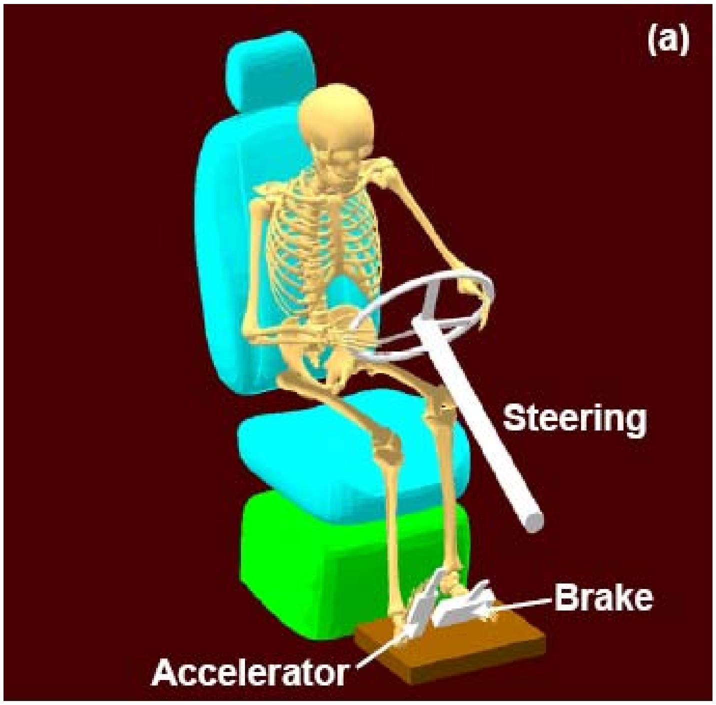

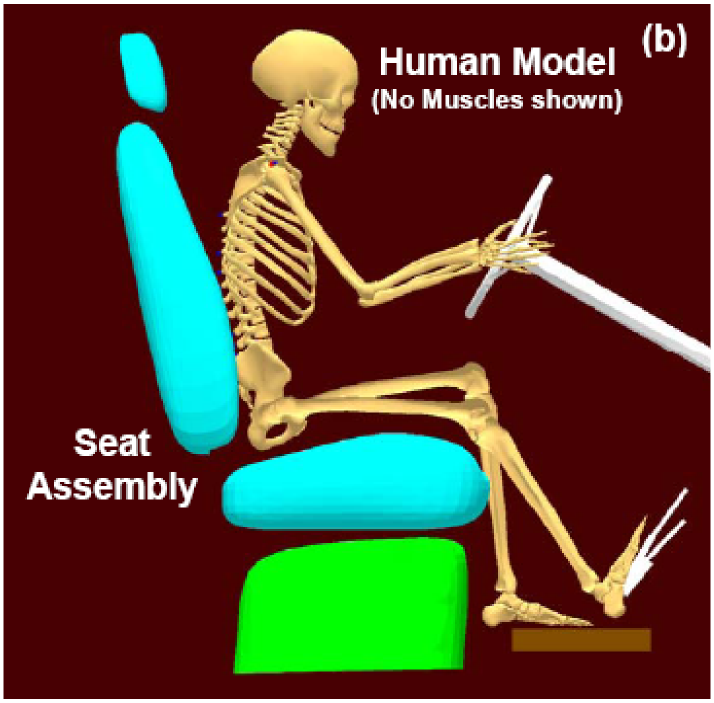

Figure 3-3. (a) Isometric and (b) side-view of the car driver-seat assembly.

III.3. RESULTS AND DISCUSSION

In this section, the main results obtained in the present work are presented and discussed. First, the "*reference-case*" is considered and the key metrics related to long-distance driving fatigue are introduced. Then, several parametric studies are performed within which the effects of key driver/seat kinematic and interaction parameters (e.g. seat-back inclination angle, back-rest/seat-pan upholstery-controlled friction coefficient, seat-pan track/longitudinal position, and the absence/presence of lumbar support) are investigated.

III.3.1. The Reference Case

Within the reference case, the following driver/seat kinematic/interaction parameters are used: back-rest (backward) inclination angle = 10^o; seat-height = 600 mm (relative to the foot-rest); human-body/car-seat friction coefficient = 0.5 (corresponds to atypical value associated with woven wool- or cotton-based fabric seat-upholstery); seat-pan track position = 830 mm (corresponds to the distance between the driver's right heel and the driver's right hip); and lumbar support is used.

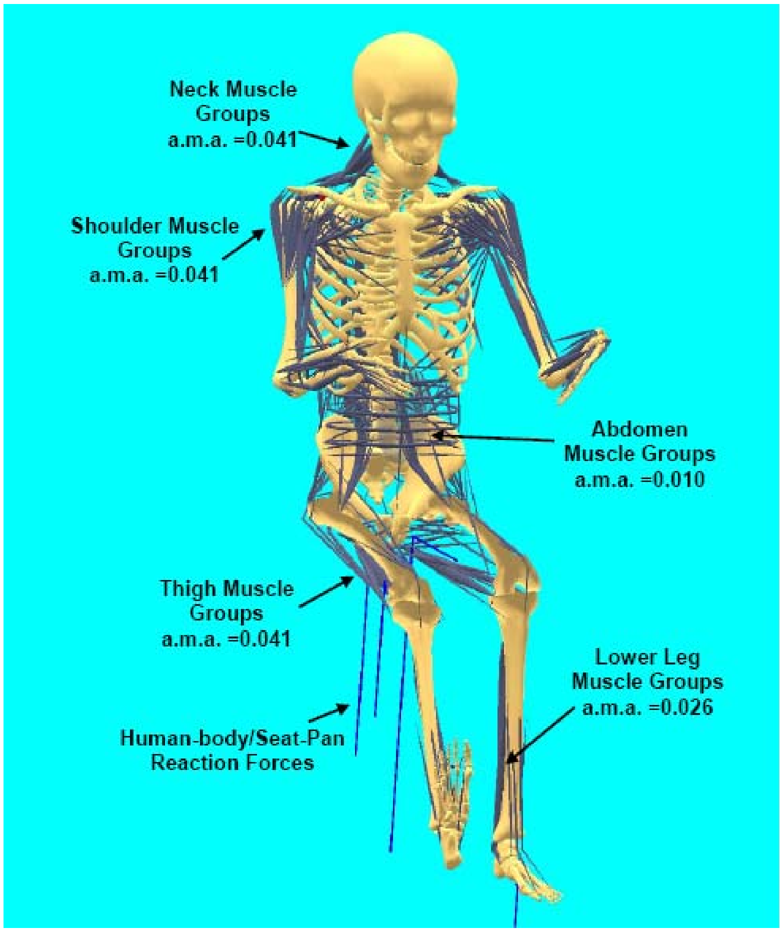

Figure 3-4. Muscle groups with the largest values of the average muscle activity (a.m.a.) for the reference case of the driver/car-seat interaction model.

An example of the results of the present musculoskeletal computational analysis of long-distance driving comfort and fatigue for the reference case is displayed in Figure 3-4. In this figure, the extent of actuation of the various muscles is displayed pictorially by the extent of their bulging. Furthermore, muscle groups associated with the largest levels of activation are identified and the typical range of activation is indicated. It is seen that the following three muscle groups are associated with the largest extent of muscle-activity (i.e. that the following three muscle groups define the muscle activity envelope): (a) the *Corachobrachialis*, the *Deltoid* and the *Scapular* muscles located in the forearm/shoulder region; (b) the *Scalene,* the *Infraspinatus,* the *Supraspinatus* neck muscles; and (c) the *Semimembranosus* and the *Rectus Femoris* thigh muscles (all with an average activity of 0.041). The next two groups of highly-activated muscles are the *Soleus* muscles (average activity: 0.026), found in the lower legs and the *Rectus Abdominis* and the *Oblique* muscles found in the abdomen regions, associated with significantly lower levels of activation (average activity: 0.010).

It is well documented that in addition to the activity of the muscles, long-distance driving discomfort and fatigue are affected by shear contact forces present at the human-buttocks/seat-pan interface. In the reference case considered in this section, the total shear contact force was evaluated as 292*N*.

When seating discomfort and the associated fatigue are investigated experimentally (e.g. [3.23]) or analyzed computationally using the finite-element method [3.42], the maximum contact pressure is found at the human-buttocks/seat-pan and thigh/seat-pan interfaces. As expected earlier, a number of support points were used to model driver/seat contact interactions. Since these points were fairly equally spaced, one can assume that the maximum normal contact force is a good representation of the maximum contact pressure. In the reference case, this force was found to be 615*N*.

While it is not fully agreed that the magnitude of the intradiscal compressive forces in the spine contribute to long-distance driving fatigue, their detrimental effect on the spine health is well established [3.43]. For comparison with the other cases studied in the present work, the intradiscal compressive force between the fourth and the fifth lumbar vertebrae was computed for reference case and found to be ca. 331*N*. It is also well-established [3.43] that intradiscal spine loads are generally higher in the seating posture than in the corresponding standing posture due to the forward rotation of the pelvis around the pelvis/lumbar joints, Figures 3-5(a) - (b).

III.3.2. The Effect of Back-rest Inclination

As mentioned earlier, the (backward) back-rest inclination angle was set to 10° in the reference case. In this section, the effect of varying the back-rest inclination angle in a 0°-15° range in the increments of 5° is examined.

An example of the results obtained in this portion of the work pertaining to the 0° back-rest-inclination angle is displayed in Figure 3-6. The results displayed in this figure show that the following two muscle groups are associated with the highest level of activation: (a) the *Scalene*, the *Infraspinatus,* the *Supraspinatus* neck muscles and (b) the left *Soleus* (lower left leg) muscles all with an average muscle-activity level of ca. 0.041. The next three groups of muscles associated with a high level of muscle activity are: (a) the *Deltoid* (shoulder) muscles with an average activity of ca. 0.035; (b) the *Semimembranosus* and the right *Rectus Femoris* (the lower thigh and the upper thigh muscles, respectively) with an average muscle activity of ca. 0.024; and (c) the *Obliques* and *Rectus Abdominis* (abdomen) muscles with an average muscle activity of ca. 0.010.

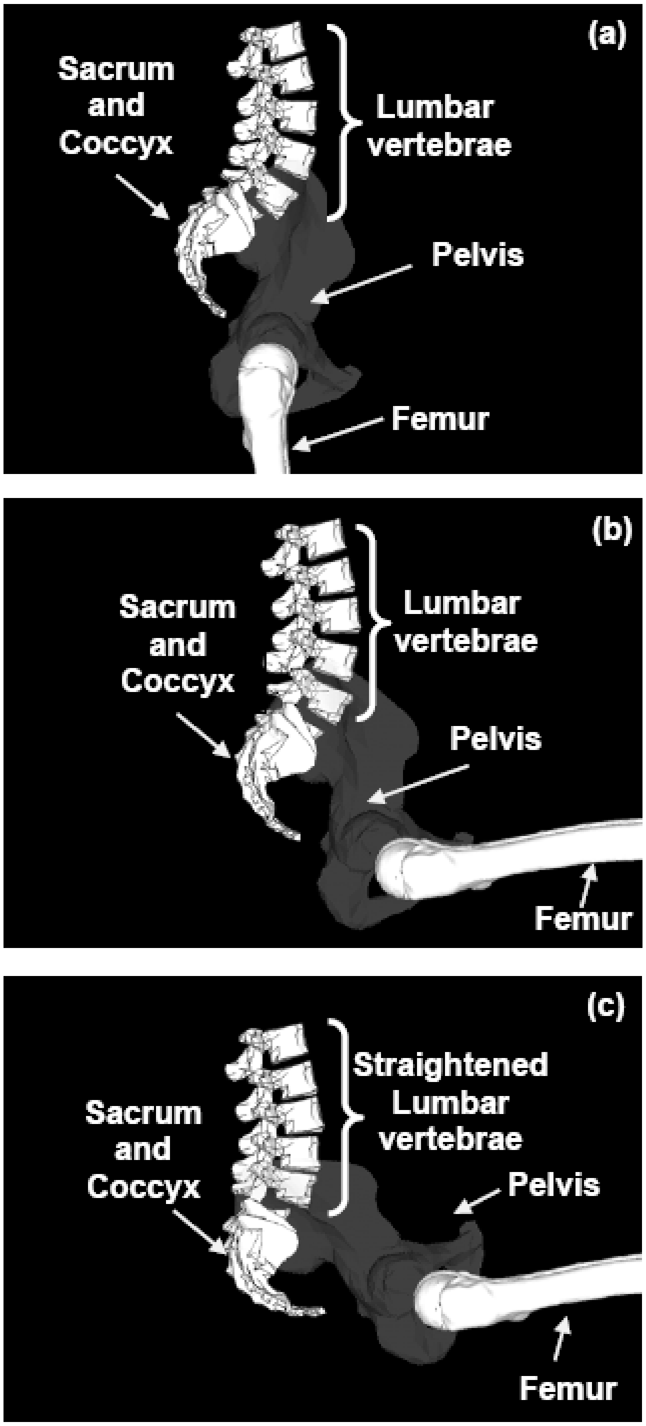

Figure 3-5. Evaluation of the kinematics of the human-body pelvis region with a change in posture from: (a) standing to: (b) sitting erect to: (c) sitting in hunch-back posture.

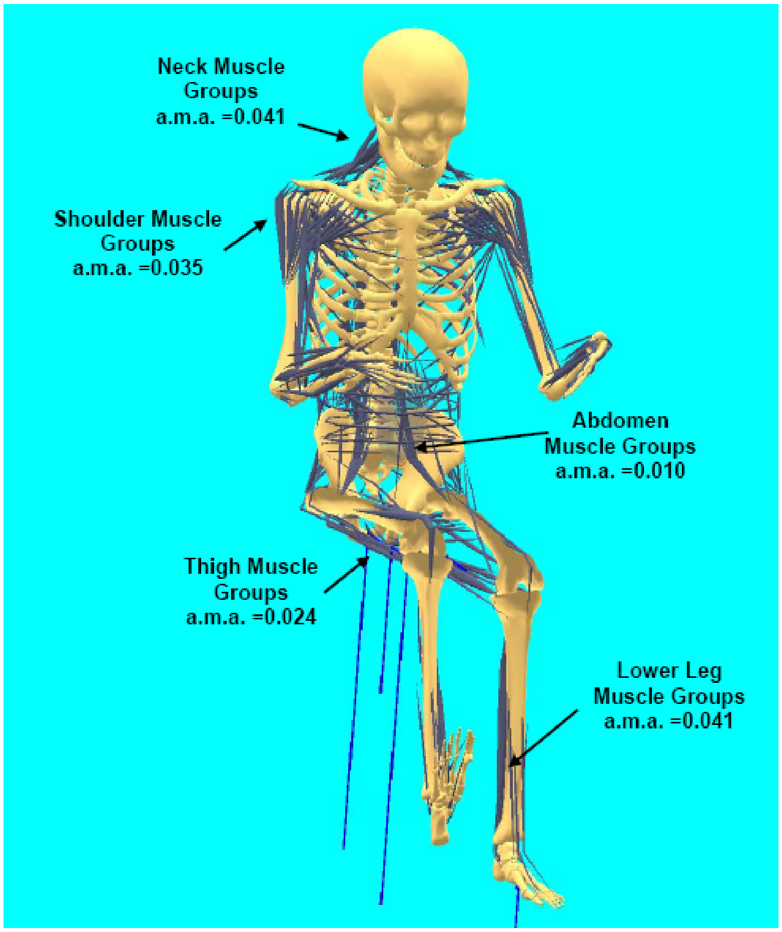

Figure 3-6. Muscle groups with the largest values of the average muscle activity (a.m.a.) for the 0- back-rest inclination angle case of the driver/car-seat interaction model.

A comparison of the results displayed in Figure 3-4 and Figure 3-6 reveals several important findings:

(a) While the muscle-activity envelope has not changed, different three groups of muscles define the envelope, i.e. as the back-rest has been brought into the upright position, the thigh muscle group has been substituted by the lower leg muscle group in the muscle-activity envelope and the shoulder muscles are no longer on the muscle-activity envelope;

(b) As the back-rest is placed in the straight upright position, and the shoulders get close to the steering wheel, the shoulder muscle activity drops from ca. 0.041 to ca. 0.035. This finding is expected since as the shoulder-to-steering-wheel distance decreases and shoulder flexing lowers the center of gravity of the arms, a lower level of muscle activation is required to retain the imposed kinematic configuration of the arms;

(c) The lower leg muscles whose activation level in the reference case was ca. 0.026, has increased in the 0º back-rest inclination angle case considerably to ca. 0.041. This finding is also reasonable since as the upper body is taking a more upright posture and less vertical support is provided by the seat back-rest, leg muscles' activity has to increase in order to support the human-body weight; and

(d) The abdominal and neck muscles have retained their levels of muscle activity.

The effect of variation of the seat back-rest inclination angle on the average muscle activity of the five muscle groups mentioned above (i.e. neck, shoulder, abdominal, thigh and lower-leg muscle groups) is displayed in Figure 3-7(a). The results shown in this figure indicate that, for the most part, the muscle activation changes monotonically with the back-rest inclination angle.

In Figure 3-7(b), the effect of variation of the seat-back inclination on the magnitude of the intradiscal L4-L5 compressive force and on the seat-pan/human-buttocks shear force is displayed. The results displayed in Figure 3-7(b), which pertain to the effect of seat-back inclination angle on the intradiscal force, are reasonable since as the thorax becomes to lean forward, the line of gravity of the upper body moves forward and increases the moment which has to be counterbalanced by higher intradiscal forces and higher abdominal muscle activities.

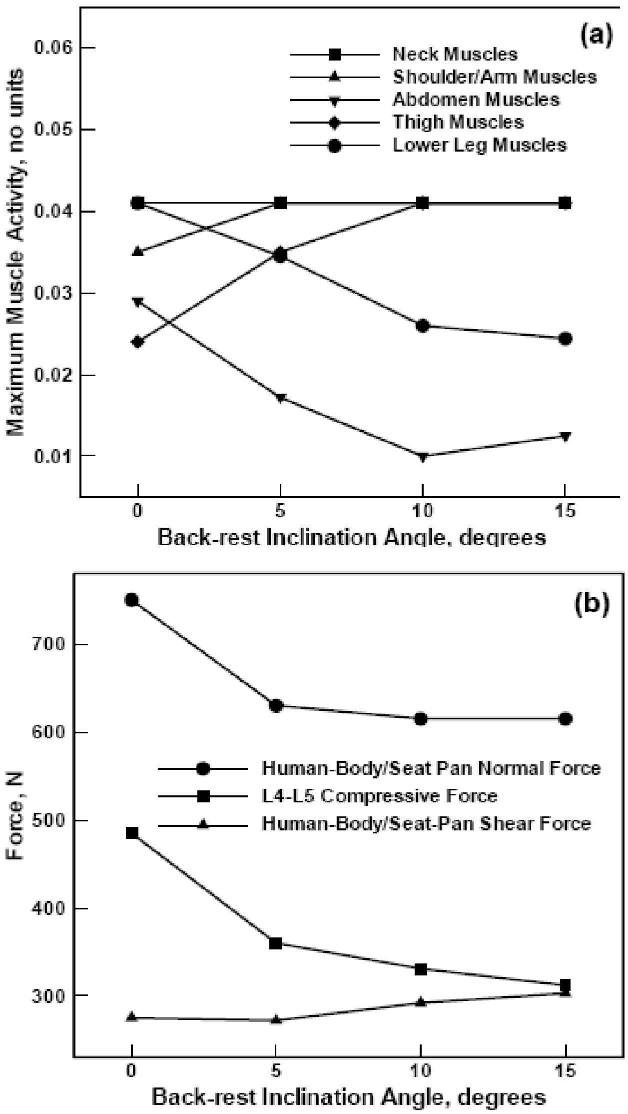

Figure 3-7. The effect of variation in the back-rest inclination angle on: (a) the maximum muscle activity; and (b) the maximum normal and total shear contact forces and the intradiscal L4-L5 compressive forces.

III.3.3. The Effect of Friction Coefficient

In the reference case, the friction coefficient between the driver and the car seat was set to a value of 0.5 which roughly corresponds to the case of woven wool- or cotton-fabric seat upholstery. Car seats are often equipped with vinyl or leather covering and in these cases the friction coefficient typically takes a significantly lower value (assumed as 0.2, in the present work). In this section, the effect of reduction of the friction coefficient from 0.5 to 0.2 is considered while all other kinematic parameters of the driver and the seat are kept at their reference-case values as defined in Section III.3.1.

An example of the results obtained in the present low-friction-coefficient case is displayed in Figure 3-8. It is seen that the following four muscle groups define the muscle-activity envelope: (a) the *Infraspinatus*, *Supraspinatus* and *Scalene* (neck) muscles; (b) the *Deltoid*, *Corachobrachialis* and *Scapular* (shoulder) muscles; (c) the *Rectus Abdominis* and *Oblique* (abdominal) muscles; and (d) the *Soleus* (lower leg) muscles, all with an average muscle activity of 0.041. It is also seen that the *Semimembranosus* and *Rectus Femoris* (thigh) muscles display a lower level of muscle activity (muscle activity of 0.023).

A comparison of the results displayed in Figure 3-4 and Figure 3-8 shows that while the muscle-activity envelope has not changed measurably, the muscle groups defining the envelope have changed. That is, the thigh muscles are no longer associated with the highest level of muscle activity (average muscle activity level = 0.023), while the legs and abdomen muscles have joined the shoulders and the neck muscles as the muscle groups with the highest level of activation (average muscle activity level =

0.041). This finding is reasonable considering the fact that at a back-rest inclination angle of 10° and in the presence of a lower value of friction coefficient, the shear/tangential forces originating at the thorax/back-rest interface and propagated to the human-buttocks/seat-pan interface cannot be fully counterbalanced by the friction forces causing the leg and abdomen muscles to be engaged more extensively (in order to prevent the driver from sliding).

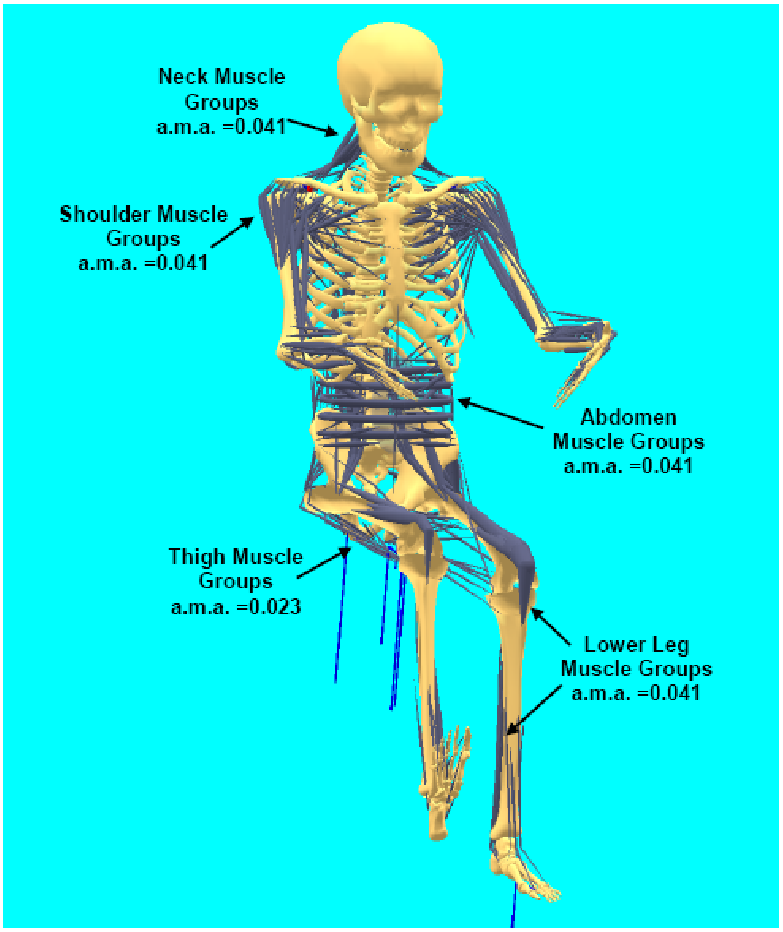

Figure 3-8. Muscle groups with the largest values of the average muscle activity (a.m.a.) in the driver/car-seat interaction model for the case of a lower human-body/seat interface friction coefficient.

The human-buttocks/seat-pan total shear force (116*N*) is reduced significantly relative to that in the reference case (292*N*). This is clearly related to the fact that the maximum tangential force is controlled by the magnitude of the friction coefficient (as well as by the magnitude of the normal force).

Reduction in the friction coefficient from 0.5 to 0.2 has been found to lower the maximum normal contact force by less than 5% relative to that observed in the reference case.

The intradiscal L4-L5 compressive force (345*N*) was found to be somewhat higher than that of its reference-case counterpart (331*N*). This finding indicates that as the friction coefficient is reduced and lesser support is provided to the thorax by the back-rest, more upper-body weight has to be supported by the spine itself.

III.3.4. Effect of (Front/Back) Seat Track Position

In this section, the effect of longitudinal-position adjustment of the seat along the track is considered. Two specific cases are analyzed: (a) forward translation of the seat by 10 *cm* (no significant differences in the level of activation of the muscle groups analyzed so far or in the magnitudes of the lumbar and shear forces, relative to the reference case are observed); and (b) backward translation of the seat by 10 *cm*(the results discussed below).

For brevity, no figures will be shown for the 10 *cm* back-translation case and the key result will only be discussed. Three muscle groups, the shoulder, the neck and the thigh muscles, define the muscle-activity envelope associated with a muscle-activity level of 0.043. This level is somewhat higher than the reference-case level (0.041), and this increase can be attributed to the fact that the steering wheel is farther away (this increases shoulder and neck muscles activity) and since the accelerator pedal is also farther away, lower thigh muscles have to be engaged more extensively to keep the right foot on the accelerator pedal.

One more significant observation was made: the *Erector Spinae* and the *Spinalis* muscle located at the back of the thoracic section of the spine are found to acquire an increased level of activity. This finding can be attributed to the fact that as the arms and the right leg are getting extended, the spine tends to bend to a hunch-back configuration which is supported by the aforementioned thoracic-spine muscles.

The backward translation of the seat by 10 *cm* has been found to reduce the total shear contact force from 292*N* to 254*N*. This finding is consistent with the fact that as the spine is becoming to acquire the hunch-back configuration, less contact is expected between the thorax and the back-rest.

The normal force has been found to remain essentially unchanged with the changes in the track position of the seat.

The intradiscal L4-L5 compressive force, on the other hand, is found to increase with the 10cm backward translation of the seat, from 331*N* to 341*N*. This increase can be attributed to the effect of lesser support of the thorax by the back-rest in the case of the hunch-back configuration of the spine.

Also, as shown in Figure 3-5(c), for the hunch-back configuration of the spine, the forward shift in the upper-body line of gravity is increased significantly which, as mentioned earlier, leads to increased intradiscal forces. Figure 3-5(c) also shows that the shape of lumbar-portion of the spine changes (i.e. the lumbar section becomes more straight) which also contributes to an increase in the intradiscal forces.

III.3.5. The Effect of Lumbar Support

In the reference case, as well as in all other cases analyzed up to this point, lumbar support at the back-rest was used. In this section, the effect of lumbar-support removal is investigated. Again, a complete set of results will be discussed but not shown (for brevity):

An example of the results obtained in the present section is displayed in Figure 3-9(a). For comparison, the corresponding results obtained in the reference case are displayed in Figure 3-9(b). The comparison of results displayed in Figures 3-9(a) - (b) reveals that:

(a) The muscle activity level corresponding to the muscle-activity envelope has been raised (from 0.041 in the reference case) to 0.058;

(b) Furthermore, two muscle-groups define the muscle-activity envelope: (a) the shoulder muscles and (b) the abdomen muscles;

(c)The neck muscle group has retained its muscle activity at the level observed in the reference case (average muscle activity level of 0.041);

(d) Both the thigh and the leg muscle groups have significantly reduced their level of activity relative to the reference case (0.041 --> 0.010 and 0.026 --> 0.010, respectively). This finding is consistent with the fact that as the back-rest support is lowered due to removal of the lumbar support, less shear forces are transferred to the thighs and, in turn, to the legs; and

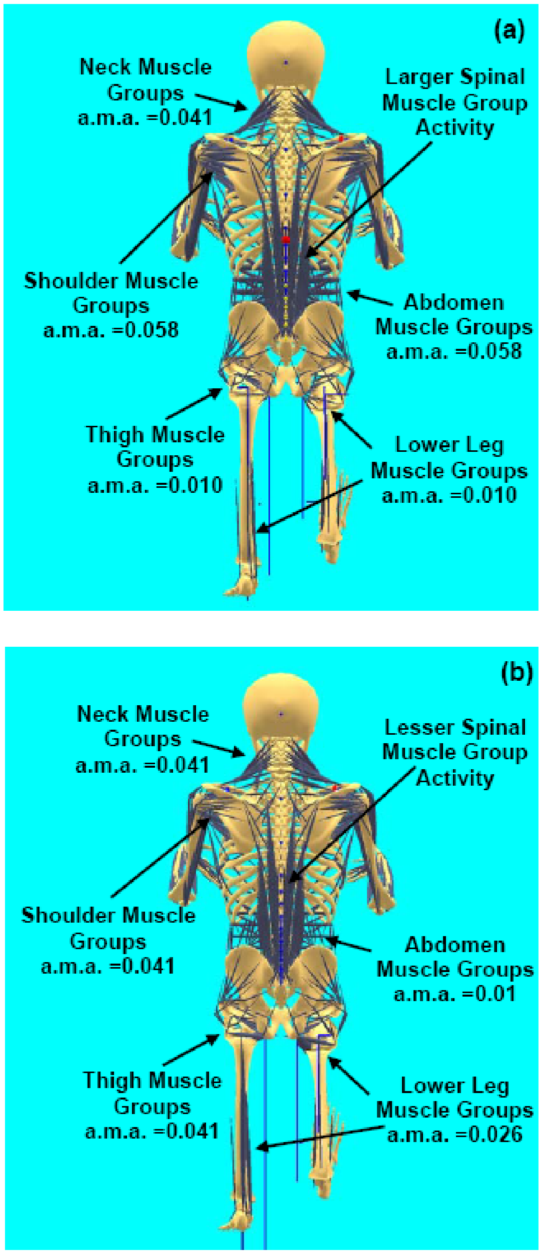

Figure 3-9. Muscle groups with the largest values of the average muscle activity (a.m.a.) for: (a) the driver/car-seat configuration without lumbar support; and (b) the reference case.

(e) The level of activity of the muscles in the back of the human-body (supporting the spine) has significantly increased (>0.010) compared to the reference case (<0.005).

The total shear force at the human-body/seat-pan interface has decreased from ca. 252*N* in the reference case to ca. 115*N*. At the same time, the normal contact force has remained effectively unchanged. As far as the intradiscal L4-L5 compressive force is concerned, it has increased from ca. 373N in the reference case to ca. 400*N*.

III.4. DISCUSSION

In the introduction section, Section III.1, of the present work, it was discussed that the main factors contributing to the long-distance driving fatigue are the maximum level of muscle activity, the magnitude of the driver/car-seat contact total shear force, the maximum contact normal force and the magnitude of intradiscal spine forces (e.g. the intradiscal L4-L5 compressive force). In Section III.3, the effect of four driver/car-seat kinematic/interaction parameters (i.e. the back-rest inclination angle, the friction coefficient, the longitudinal-track seat-position and the presence/absence of lumbar support) on the driving-induced fatigue-controlling parameters was investigated. In the present section, an attempt is made to provide more insight into the problem of long-distance driving fatigue and to set the foundation for future developments of a long-distance driving fatigue function. Toward that end, available public-domain data pertaining to the subjective input of human test subjects, the contact-pressure and EMI measurements will be used.

A review of the public-domain literature showed that there are no driving-induced fatigue functions which can relate the objectively measured or computed driver/seat interaction parameters (e.g. maximum muscle activity, maximum normal contact force, etc.) with the subjective perception of fatigue by the human test subjects. It is interesting to note that Rasmussen and de Zee [3.31] proposed a short-term seating discomfort function, as a linear combination of the squared maximum muscle activity and the squared (properly normalized) total contact shear force. While this function can be a good starting point in the development of a long-distance driving fatigue function, one must recognize that fatigue does not only depend on the maximum level of muscle activation but also on the number of muscles or muscle groups associated with the highest level of activation.

The review of public-domain literature further revealed that the long-distance driving-fatigue investigation involving subjective inputs from human test subjects and objective EMI and contact pressure measurements reported in Ref. [3.41] is most closely related to the present work. Hence, a brief summary of the main findings reported in Ref. [3.41] is next presented.

The main findings reported in Ref. [3.41] can be summarized as follows: (a) Despite significant variations in human test-subjects subjective evaluations, the study clearly established that there are correlations between the perception of fatigue and particular measurable human-body/car-seat kinematics/interaction parameters; (b) The three parameters which were found to most profoundly affect the perception of fatigue were identified as: (i) insufficient support provided by the seat to the lumbar region of the driver’s spine, (ii) insufficient thorax support and (iii) excessive thorax support. The three types of supports were quantified via contact pressure measurements; (c) Furthermore, the study established that depending on the level of support provided by the car seat, the driver test subjects were found to adopt different seating postures. The associated level of muscle activity of different muscle groups were measured and also correlated with the subjective perception of fatigue. Specifically, neck, shoulder, abdomen, thigh, leg and spine muscle groups (i.e. the muscle groups investigated in Section III.3 of the present work) were found to be the key contributors to long-distance driving-fatigue perception; (d) Contact normal and shear forces acting on buttocks/thighs were not directly investigated/measured. However, the computational study carried out in Section III.3 of the present work clearly established relationships between the back-rest/lumbar support levels and the effects of normal/shear contact forces; and (e) Intradiscal forces were also not measured since it was assumed that these forces may affect spine health but not play a major role in the fatigue perception. Since this opinion is broadly observed in the literature, it was also adopted in the present work.

Based on the findings obtained in the present work, the overview of the results obtained in Ref. [3.41] and other comments made throughout this manuscript, one should expect that the long-distance driving-fatigue function, *LDDFF*, has the following general form:

$$LDDFF = func(CMA, CNF, CSF) \tag{3.5}$$

where *CMA*, *CNF* and *CSF* denote the cumulative muscle activity, the contact normal force and the contact shear force, respectively. Furthermore, to a first-order of approximation, *CMA* can be represented by the sum of activity levels of the muscle groups defining the muscle activity envelope.

To avoid potential complications arising from the fact that *CSF* could be either positive or negative and that *CNF* is zero or negative (compressive), Eq.3.5 has been rewritten as:

$$LDDFF = func(CMA^2, CNF^2, CSF^2) \tag{3.6}$$

Since the exact mathematical form for the function *"func"* is presently not known, the following simple weighted-average form can be used as a starting point:

$$LDDFF = w_{CMA}\left(\frac{CMA}{CMA^*}\right)^2 + w_{CNF}\left(\frac{CNF}{CNF^*}\right)^2 + w_{CSF}\left(\frac{CSF}{CSF^*}\right)^2 \tag{3.7}$$

where CMA^*, CNF^*(=1.0) and CSF^* are normalizing factors used to bring *CMA* and *CSF* values to a level comparable to that of *CNF* and *w's* define the relative weighing coefficients for the three fatigue-controlling factors. The magnitude of the *w's* quantifies the relative importance of the three fatigue-controlling factors. Since only relative values of the *w's* are important, *wCNF* was set to 1.0.

To establish preliminary values of the two remaining weighting coefficients (as well as of the two remaining normalizing factors, CMA^* and CSF^*), the following simple analysis was carried out: (a) Based on the results displayed in Figure 3-7(b), characteristic values for *CNF* and *CSF* are chosen as 600*N* and 300*N*, respectively. Consequently, CSF^* is set to 0.5(=300*N*/600*N*); (b) Since it is well-established that contact shear forces contribute more towards fatigue perception (as well as to muscle trauma/tissue-necrosis [3.30]), *wCSF* is arbitrarily set to 1.5 (i.e. *CSF* is assumed to contribute 50% more than *CNF* to the perception of fatigue); (c) At the prevailing muscle activity level of 0.041, and a typical number of 66 muscles defining the muscle-activity envelope, CMA^* can be defined as 0.0045(=0.041·66/ 600); and (d) While the contact normal and shear forces may play a more critical role in the perception of short-term seating discomfort, the role of cumulative muscle activity is expected to be dominant in the perception of long-distance driving fatigue. Consequently, and arbitrarily, *wCMA* is set to 5.0. In other words, cumulative muscle activity is assumed to contribute five times more to fatigue perception than the maximum contact normal force.

Based on the analysis presented above, Eq.3.7 can be rewritten as:

$$LDDFF = 5.0\left(\frac{CMA}{0.0045}\right)^2 + 1.0\left(\frac{CNF}{1.0}\right)^2 + 1.5\left(\frac{CSF}{0.5}\right)^2 \tag{3.8}$$

This function is currently being used in our ongoing work in order to test its validity both against the results recorded in the Ref. [3.41] and the results being obtained in the ongoing investigation. A detailed account of the findings will be reported in our future communications.

III.5. SUMMARY AND CONCLUSIONS

Based on the results obtained in the present work, the following main summary remarks and conclusions can be drawn:

1. Musculoskeletal modeling and simulation technique is employed in order to investigate the problem of long-distance driving fatigue.

2. The effect of several driver/car-seat kinematic/interaction factors (e.g. backrest inclination angle, human-body/car-seat interface friction coefficient, longitudinal-track position of the seat and presence/absence of lumbar support) on the factors controlling

driving fatigue (e.g. maximum muscle activity, contact normal and shear forces intradiscal spine forces, etc.) has been investigated.

3. A preliminary long-distance driving fatigue function (*LDDFF*) has been constructed in accordance with the findings obtained in the present work as well as the findings reported in the open literature.

REFERENCES

[3.1]. U. Johansen and A. Johren, “*Personalekonomi idag.,*” Uppsala Publishing House, ISBN, 9170052026, 2002.

[3.2]. K. Ebe and M.J. Griffin, “*Factors Effecting Static and Seat Cushion Comfort,*” Ergonomics, 41, 10, 2001, 901-992.

[3.3]. H. Inagaki, T. Taguchi, E. Yasuda and Y. Iizuka, “*Evaluation of Riding Comfort: From the Viewpoint of Interaction of Human Body and Seat for Static, Dynamic and Long Time Driving,*” SAE Conference, SAE no. 2000-02-0643, 2000.

[3.4]. K. Kamijo, H. Tsujimura, H. Obara and M. Katsumata, “*Evaluation of Seating Comfort,*” SAE Conference, no. 820761, 1982.

[3.5]. J. Lee, T. Grohs and M. Milosic, “*Evaluation of Objective Measurement Techniques for Automotive Seat Comfort,*” SAE Conference, SAE no. 950142, 1995.

[3.6]. A. Milvojevich, R. Stanciu, A. Russ, G.R. Blair and J.D. van Heumen, “*Investigating Psychometric and Body Pressure Distribution Responses to Automotive Seating Comfort,*” SAE Conference, SAE no. 2000-01-0626, 2000.

[3.7]. S.J. Park and C.B. Kim “*The Evaluation of Seating Comfort by Objective Measures,*” SAE Conference, SAE no. 970595, 1997.

[3.8]. S.J. Park, Y.S. Lee, Y.E. Nahm, J.W. Lee and J.S. Kim, “*Seating Physical Characteristics and Subjective Comfort: Design Considerations,*” SAE Conference, SAE no. 980653, 1998.

[3.9]. M.P. Reed, M. Saito, Y. Kakishima, N.S. Lee and L.W. Schneider, “*An Investigation of Driver Discomfort and Related Seat Design Factors in Extended-duration Driving,*” SAE Conference, SAE no. 910117, 1991.

[3.10]. V.K. Tewari and N. Prasad, “*Optimum Seat Pan and Back-rest Parameters for a Comfortable Tractor Seat,*” Ergonomics, 43, 2, 2000, 167-186.

[3.11]. K. Thakurta, D. Koester, N. Bush and S. Bachle, “*Evaluating Short and Long Term Seating Comfort,*” SAE Conference, SAE no. 950144, 1995.

[3.12]. K. Uenishi, K. Fujihashi, and H. Imai, “*A Seat Ride Evaluation Method for Transient Vibrations,*” SAE Conference, SAE no. 2000-01-0641, 2000.

[3.13]. M.H. Yun, L. Donjes and A. Freivalds, "*Using Force Sensitive Resistors to Evaluate the Driver Seating Comfort,*" Adv. Ind. Ergon. Saf. IV, 1992, 403-410.

[3.14]. L.Q. Zhao, Q.S. Xia and X.T. Wu, "*Study of Sitting Comfort of Automotive Seats,*" SAE Conference, SAE no. 945243, 1994.

[3.15]. D.L. Bader and P. Bowder, "*Mechanical Characteristics of Skin and Underlying Tissues in vivo,*" Biomaterials, 4, 1980, 305-308.

[3.16]. C.W.J. Oomens, E.M.H. Bosboom, O.F.J.T. Bressers, C.V.C. Bouten and D.L. Bader, "*Can Loaded Interface Characteristics Influence Strain Distribution in Muscles Adjacent to Bony Prominences,*" Comp. Meth. Biomech. Eng., 6, 3, 2003, 171-180.

[3.17]. D.L. Bader and P. Bowder, "*Ischial Pressure Distribution Under the Seated Person,*" In: D.L. Bader, ed., Pressure Sores- Clinical Practice and Scientific Approach, 1990, 223-233.

[3.18]. L. Bennett, D. Kauver, B.Y. Lee and F.A. Trainor, "*Shear vs. Pressure as Causative Factors in Skin Blood Flow Occlusion,*" Arch. Phys. Med. Rehabil., 60, 1979, 309-314.

[3.19]. W.W. Chow and E.I. Odell, "*Deformation and Stresses in Soft Body Tissues of a Sitting Person,*" J. Biomech. Eng., 100, 1978, 79-87.

[3.20]. T.A. Krouskop, S.L. Garber and P. Noble, "*Pressure Management and the Recumbent Person,*" In: D.L. Bader, ED., Pressure Sores- Clinical Practice and Scientific Approach, 1990, 235-248.

[3.21]. S.M. Reichel, "*Shear Force as a Factor in Decubitus Ulcers in Paraplegics,*" J. Am. Med. Assoc., 166, 1958, 762-763.

[3.22]. J. Scales, "*Pressure Sore Prevention,*" Care. Sci. Pract., 1, 1982, 9-17.

[3.23]. M.M. Verver, J. van Hoof, C.W. Oomens, J.S. Wismans, F.P. Baaijens, "*A Finite Element Model of the Human Buttocks for Prediction of Seat Pressure Distributions,*" Comput. Methods Biomech. Biomed. Eng., 7, 2004, 193–203.

[3.24]. M. Langsfeld, A. Frank, D.L. van Deursen and P. Griss, "*Lumbar Spine Curvature During Office Chair Sitting,*" Med. Eng. Phys., 22, 2000, 665-669.

[3.25]. *AnyBody 3.0*, AnyBody Technology A/S, Aalborg, Denmark, 2008.

[3.26]. M. Damsgaard, J. Rasmussen, S.T. Christensen, E. Surma and M. de Zee, "*Analysis of Musculoskeletal Systems in the AnyBody Modeling System,*" Simul. Model. Pract. Theory, 14, 2006, 1100–1111.

[3.27]. A.C. Mandal, "*The Seated Man (homosedens) – the Seated Work Position: Theory and Practice,*" Appl. Ergon., 12, 1984, 19–26.

[3.28]. A.C. Mandal, "*The Influence of Furniture Height on Back Pain,*" Behav. Inform. Technol., 6, 1987, 347–352.

[3.29]. D. Karlsson, A.-L. Osvalder and J. Rasmussen, "*Towards Better Seating Design-A Discussion and Comparison between Office Chairs and Car Seats,*" Proceedings of the 39th Nordic Ergonomics Society Conference, Sweden, 2007.

[3.30]. J. Rasmussen, M. de Zee and S. Torholm, "*Muscle Relaxation and Shear Force Reduction may be Conflicting: A Computational Model of Seating,*" SAE Conference, SAE no. 2007-01-2456, 2007.

[3.31]. J. Rasmussen and M. de Zee, "*Design Optimization of Airline Seats,*" SAE Conference, SAE no. 2008-01-1863, 2008.

[3.32]. J. Rasmussen, S. Torholm and M. de Zee, "*Computational Analysis of the Influence of Seat Pan Inclination and Friction on Muscle Activity and Spinal Joint Forces,*" International Journal of Industrial Ergonomics, 39, 2009, 52-57.

[3.33]. S. Dendorfer and S. Torholm, "*Final Report on Feasibility Study,*" Report no: 21385/08/NL/PA, presented to ESTEC/ESA by AnyBody Technology A/S, May, 2008.

[3.34]. *AnyScript Model Repository 7.1*, AnyBody 3.0, AnyBody Technology A/S, Aalborg, Denmark, 2009.

[3.35]. F.C.T. Van der Helm, "*A Finite Element Musculoskeletal Model of the Human Shoulder Mechanism,*" J. Biomech., 27, 1994, 551–569.

[3.36]. M. de Zee, L. Hansen, C. Wong, J. Rasmussen and E.B. Simonsen, "*A Generic Detailed Rigid-body Lumbar Spine Model,*" J. Biomech., 40, 2007, 1219–1227.

[3.37]. H. Wilke, P. Neef, B. Hinz, H. Seidel and L. Claes, “*Intradiscal Pressure Together with Anthropometric Data – a Data Set for the Validation of Models,*” Clin. Biomech., 16 (Suppl. 1), 2001, S111–S126.

[3.38]. P. de Jong, M. de Zee, P.A.J. Hilbers, H.H.C.M. Savelberg, F.N. van de Vosse, A. Wagemakers and K. Meijer, “*Multi-body Modeling of Recumbent Cycling: An Optimization of Configuration and Cadence,*” Master’s Thesis Medical Engineering, TU/e Biomodelling and Bioinformatics, University of Maastricht, Movement Sciences, Aalborg University, 2006.

[3.39]. K.N. An, B.M. Kwak, E.Y. Chao and B.F. Morrey, “*Determination of Muscle and Joint Forces: A New Technique to Solve the Indeterminate Problem,*” J. Biomech. Eng., 106, 1984, 364–367.

[3.40]. J.A. Bell and M. Stigant, “*Development of a Fibre Optic Goniometer System to Measure Lumbar and Hip Movement to Detect Activities and their Lumbar Postures,*” J. Med. Eng. Technol., 31, 2007, 361–366.

[3.41]. N. Michida, H. Okiyama, K. Nishikawa and T. Nouzawa, “*A Study of Drivers’ Fatigue Mechanisms during Long Hour Driving,*”SAE Conference, SAE No. 2001-01-0381, 2001.

[3.42]. M. Grujicic, B. Pandurangan, G. Arakere, W. C. Bell, T. He, X. Xie, “*Seat-cushion and Soft-tissue Material Modeling and a Finite Element Investigation of the Seating Comfort for Passenger-vehicle Occupants,*” Materials and Design, submitted for publication, February 2009.

[3.43]. V.H. Frankel and M. Nordin, “*Basic Biomechanics of the Skeletal System,*” Lea and Febiger Publications, Philadelphia, 1980.

CHAPTER FOUR

DESIGN-OPTIMIZATION AND MATERIAL SELECTION FOR A FEMORAL-FRACTURE FIXATION-PLATE IMPLANT

ABSTRACT

The problem of size/thickness optimization of a distal femoral-fracture fixation-plate is addressed computationally using a combined finite-element/design-optimization procedure. To obtain realistic physiological loading conditions associated with normal living activities (cycling, in the present case), a musculoskeletal multi-body inverse-dynamics analysis is carried out of a human riding the bicycle. While optimizing the design of the femoral-fracture locking-plate, realistic functional requirements pertaining to attain the required level of fracture-femur fixation and longevity/lifecycle were used. It is argued that these types of analysis should be used to complement preclinical implant-evaluation tests, the tests which normally include a limited number of physiological loading conditions and single pass/fail outcomes/decisions with respect to a set of lower-bound implant-performance criteria.

IV.1. INTRODUCTION

It is common practice to use the return of a patient to normal activities of daily living following a surgical procedure involving an implantable device (e.g. femoral-fracture fixed-plate implant, total hip replacement, etc.) as a measure of the success of the surgery [4.1]. On the other hand, as people are living longer and continuing to maintain active lifestyles, longevity of the implanted devices when subjected to physiological loads associated with the performance of normal daily activities has become an equally important measure of the success of the surgical intervention. Typically, pre-clinical implant evaluations under realistic physiological loading conditions are carried out in order to assess the lifespan of a new implant. However, in such studies, only a relatively small number of the physiological loading conditions (derived from everyday activities of the patient) are analyzed [4.2 – 4.5]. For example, long-term fatigue-controlled stability of hip implants has been evaluated under the conditions of normal walking [4.2, 4.3, 4.5], sit-to-stand [4.2], and stair climbing [4.3, 4.5] and in a combination of daily activities [4.4].

The pre-clinical implant evaluation tests mentioned above suffer from at least two major shortcomings: (a) they rely on a limited number of physiological loading conditions; and (b) the results of these studies are used only to determine if the implant has passed or failed a set of minimum-level performance criteria. Consequently, redesign of new implants is carried out only when the design has filled to meet these criteria. What is left unanswered is if the accepted new implant can meet the performance and longevity requirements under other physiological loading conditions associated with normal daily living and if the design (including the material selected for the implant) are optimal (with respect to their size, weight, cost, etc.)

The main objective of the present work is to demonstrate how musculoskeletal modeling can be used to determine physiological loading conditions not normally covered by pre-clinical implant-evaluation tests although they may refer to fairly normal daily activities (e.g. cycling). Within the present work, the recently-developed novel technology for computer modeling of the human-body mechanics and dynamics, namely the AnyBody Modeling System [4.6] and its associated public domain library of body models are being fully utilized and further developed. In its most recent rendition [4.7], the AnyBody Modeling System enables creation of a detailed computer model for the human body (including all important components of the musculoskeletal system) as well as examination of the influence of different postures and the environment on the internal joint forces and muscle activity.

The second main objective of the present paper is to demonstrate how the loading conditions derived using musculoskeletal modeling can be utilized within a combined finite-element/design-optimization procedure to carry out optimization of the design of an implanted device. Specifically, optimal thickness of a distal femoral-fracture fixation-plate under pedaling (cycling) exertion loading conditions is investigated. Optimization of the implant design/thickness is carried out with respect to its ability to meet several functional requirements pertaining to both the necessary level of fractured-femur fixation and to meeting the longevity/lifespan constraints. Details regarding these functional requirements are presented in the next section.

The organization of the paper is as follows. A brief overview of the AnyBody Modeling System is provided in Section IV.2.1. The musculoskeletal human-body model, the concepts of muscle recruitment and muscle activity envelope, the bicycle model and the issues related to human/bicycle kinematics and contact interactions are discussed in Sections IV.2.2-IV.2.5. The definition of the musculoskeletal problem of a human riding the bicycle analyzed in the present work is discussed in Section IV.2.6. The finite-element/design-optimization problem and analysis for the distal femoral-fracture fixed-plate implant are presented in Section IV.3. The results obtained in the present work are presented and discussed in Section IV.4. The main conclusions resulting from the present work are summarized in Section IV.5.

IV.2. MUSCULOSKELETAL MODELING AND SIMULATION

As mentioned earlier, two distinct computational analyses are carried out in the present work. Within the first analysis (discussed in this section), a musculoskeletal investigation of a person riding a bicycle is carried out. The resulting forces and moments, as a function of time, acting on the fractured right femur of the person riding the bicycle are next used in a finite-element/design-optimization analysis of the distal femoral-fracture fixation-plate implant.

IV.2.1. The AnyBody Modeling System [4.6]

The AnyBody Modeling System [4.6] developed at Aalborg University and used in the present work is a general-purpose musculoskeletal modeling and simulation program. The essential features of this computer program can be summarized as follows:

(a) The musculoskeletal model is typically constructed as a standard multi-body dynamics model consisting of rigid bodies, kinematic joints, kinematic drivers and force/moment actuators (i.e. muscles). The kinematic and dynamic behavior of this model can be determined using standard multi-body dynamics simulation methods;

(b) Complex geometries of the muscles and their spatial arrangement/interactions (e.g. muscles wrapping around other muscles, bones, ligaments, etc.) can be readily modeled within AnyBody Modeling System [4.6];

(c) It is well-established that a typical musculoskeletal system suffers from the so-called *"muscle redundancy problem"*: i.e. the number of muscles available is generally larger than those needed to drive various body joints. Within the living humans and animals, this problem is handled by their Central Nervous System (*CNS*) which controls muscles activation/recruitment. To mimic this role of the CNS, the AnyBody Modeling System [4.6] offers the choice of several optimization-based muscle-recruitment criteria;

(d) A typical musculoskeletal multi-body dynamics problem is solved using computationally-efficient inverse dynamics methods within which the desired motion is prescribed while the muscle activity required to produce this motion is computed;

(e) Within the AnyBody Modeling System [4.6], the muscle recruitment problem is solved using an optimization-based approach in the form:

Minimize the objective function:

$$G(f^{(M)}) \tag{4.1}$$

Subjected to the following constraints:

$$Cf = d \tag{4.2}$$

$$f_i^{(M)} \geq 0,\ \ i \in \{1, \ldots, n^{(M)}\} \tag{4.3}$$

where the objective function G (a scalar function of the vector of $n^{(M)}$ unknown muscle forces, $f^{(M)}$), defines the minimization object of the selected muscle recruitment criterion (assumed to mimic the one used by the CNS). Eq. 4.2 defines the condition for dynamic mechanical equilibrium where C is the coefficient matrix for the "*unknown*" forces/moments in the system while d is a vector of the "*known*" (applied or inertia) forces. The forces appearing in vector f in Eq. 4.2 include the unknown muscle forces, $f^{(M)}$, and the joint-reaction forces, $f^{(R)}$. Eq. 4.3 simply states that muscles can only pull (not push) and that the upper bound for the force in each muscle $f_i^{(M)}{}_i$ is the corresponding muscle strength, N_i;

(f) While there are a number of functional forms for the objective function, G, the one used in the present work is the so-called "*min/max*" form within which the objective function (to be minimized) is defined as the maximum muscle activity defined for each muscle i as $f_i^{(\mathrm{M})}/N_i$, i.e.:

$$G(f^{(M)}) = \max(f_i^{(M)} / N_i)\ ; \tag{4.4}$$

This formulation offers several numerical advantages over other popular forms of G and, in addition, it appears to be physiologically sound. That is, under the assumption that muscle fatigue is directly proportional to its activity, Eqs. 4.1 and 4.4 essentially state that muscle recruitment is based on a minimum muscle-fatigue criterion. Also, this expression for G, has been found to asymptotically approach other formulations of G (e.g. the so-called "*Polynomial*" form [4.8]).

(g) The problem defined by Eqs. 4.1 – 4.4 can be linearized using the so-called "*bound formulation*" [4.9] resulting in a linear programming problem with muscle forces and joint reaction forces as free variables. Relations between these two types of forces are next used to eliminate the joint reaction forces yielding a linear programming problem with the number of unknowns equal to the number of muscles in the system; and

(h) While for a fairly detailed full-body model containing around one thousand muscles, this constitutes a medium-to-large size problem which can be readily solved by a variety of design-optimization methods (e.g. Simplex, Interior-point methods, etc.), the min/max problem is inherently indeterminate and must be solved iteratively. This can be rationalized as follows: The min/max criterion only deals with the maximally activated muscles and with muscles which help support the maximally-activated muscles. Since the system, in general, may contain muscles that have no influence on the maximum muscle activity in the system, the forces in these muscles are left undetermined by the min/max formulation presented above. To overcome this shortcoming, the muscle-recruitment optimization problem is solved iteratively, so that each iteration eliminates the muscles with uniquely determined forces and the procedure is repeated until all muscle forces are determined.

IV.2.2. Musculoskeletal Human-body Model

The musculoskeletal model of the human body used in the present work was downloaded from the public domain AnyScript Model Repository [4.10]. The model was originally constructed by AnyBody Technology using the AnyBody Modeling System [4.6] following the procedure described in details by Damsgaard et al. [4.7].

Model Taxonomy: The musculoskeletal human-body model includes: (a) an arm/shoulder assembly containing 114 muscle units on each side of the body and having a morphology defined by Van der Helm [4.11], (b) a spine model developed by de Zee et al. [4.12] comprising sacrum, all lumbar vertebrae, a rigid thoracic-spine section, and a total of 158 muscles, and (c) a pelvis and lower extremity model with a total of 70 muscles. In total, the model contains more than 500 individual muscle units and, hence, can be considered as a fairly detailed description of the human musculo-skeletal system. The anthropometrical dimensions of the model are selected in such a way that they correspond to the female cyclist participated in the motion-capture tests, Section IV.2.7.

Segments and Joints: Within the model, the bodies (referred to as the "*segments*" within the AnyBody Modeling System) are treated as rigid with their mass/inertia properties derived from mass and shape of the associated bone and the soft tissue that is allotted to the bone. Joints in the human body are treated as idealized frictionless kinematic constraints between the adjoining segments. Both standard kinematic joints (e.g. spherical joints for the hips, hinge joints for the knees, etc.) as well as specially-developed joints (e.g. those used to represent kinematic constraints associated with floating of the scapula on the thorax) are employed.

Muscles: Muscles are treated as string contractile force –activation elements which span the distance between the *origin* and the *insertion points* through either the *via points* or by wrapping over the surfaces which stand on their way. Muscle wrapping problem is treated using a shortest-path contact-mechanics algorithm. Due to the fact that the problem considered in the present work is dynamic, muscles are modeled as being *non-isometric* (i.e. muscle strength is considered to be a function of the body posture and the rate of contraction). Also, *passive elasticity* of muscles (i.e. the resistance of the muscles to stretching) was considered.

Model Validations: The mechanics of the model is implemented as a full three-dimensional Cartesian formulation and includes inertial and gravity body forces. Integral validation of whole-body musculoskeletal models is very difficult to conduct. To the best knowledge of the present authors, validation of the whole-body musculoskeletal model is still lacking (due to major challenges which would be associated with such validation). However, various subsystems of the whole-body model were validated separately. For example: (a) The lumbar spine model was validated by de Zee et al., [4.12] by comparing the model prediction with *in vivo L4-5 intradiscal* pressure measurements of Wilke et al. [4.13]; (b) de Jong et al. [4.14] validated the lower extremity model by comparing model-predicted muscle activations and pedal forces with their experimental counterparts obtained in pedaling experiments; and (c) The shoulder model was validated in the early work of Van der Helm [4.11].

IV.2.3. The Muscle Activity Envelope

As originally recognized by An et al. [4.15], the *min/max* muscle-recruitment formulation, discussed in Section IV.2.1, defines effectively a *minimum fatigue criterion* as the basis for muscle recruitment, i.e. the aim of the proposed muscle-recruitment strategy is to postpone fatigue of the "*hardest-working*" muscle(s) as far as possible. The physiological consequence of this strategy is that muscles tend to form groups with muscles within the same group having comparable activity levels. In particular, in the muscle group associated with the maximum muscle activity there will be usually many muscles which, in a coordinated manner, carry a portion of the load comparable with their individual strengths. Consequently, in this group, many muscles will have the same activity level, which will be referred to as *"the muscle activity envelope*". The linearity of the reformulated *min/max* criterion discussed earlier guarantees that the optimization problem defined by Eqs. 4.1 – 4.3, is convex and, hence, that the solution to the problem is unique and corresponds to the global optimum. In other words, there is no other muscle recruitment strategy which can reduce the muscle-activity envelope further. Moreover, since the muscle activity envelope represents the maximum muscle activation in the model, it can be interpreted as the fraction of maximum voluntary contraction necessary to support the imposed load (gravity and inertia forces, in the present case) while maintaining the prescribed posture. Thus, the muscle-activity envelope appears to be an important parameter/measure for ergonomic-design optimization, in the sense that designs which are associated with lower envelope levels may be perceived as less fatigue-inducing.

IV.2.4. Bicycle Model

The raised-frame-bicycle used in the present musculoskeletal cycling analysis was comprised of four segments: a frame, a crank and two wheels. Three revolute joints are used to connect the crank and the two wheels to the frame.

The effort that the human body must exert in order to drive the bicycle was modeled by prescribing a time-dependent resistance crank torque. The mean value of this torque was computed using an average value of the cycling power of $170W$. The torque amplitude was defined by subtracting from the mean torque the so-called "*deadcenter crank torque*" (a value of the torque the cyclist must provide when the pedal arms are close to the vertical position and when the tangential pedal-force direction is nearly perpendicular to the preferred force direction of the legs). To comply with the fact that the two pedals function equally the crank-torque frequency is set to twice the cadence value.

IV.2.5. Human-body/Bicycle Kinematics and Interactions

The interactions between the cyclist and the bicycle were handled as follows: (a) two spherical joints were used to connect the human hands to the bicycle-frame/handlebar. These connections were attained through the use of *gloves* (one per each hand). Gloves are special elements in AnyBody which enable the definition of the joints with a finite strength and, thus, can be used to emulate the grip strength of a normal hand. This typically eliminates numerical problems (i.e. unreasonable results) associated with the use of infinitely-strong human-body/environment joints.; (b) the feet are connected to the peddle/crank using a pair of revolute joints; and (c) a general purpose joint based on linear and rotational measures was defined between the pelvis and the bicycle saddle/seat.

To quantify the extent of and to account for the distributed nature of the human-body/ bicycle-seat contact interactions, a number of support points are introduced over the bicycle-saddle surface. These support points allow the transfer of reaction forces to the bicycle-seat via the so-called "*support elements*". These elements enable quantification of the human-body/bicycle-seat contact (compressive and tangential/friction) reaction forces at the support points. It should be noted that the compressive reaction forces are perpendicular to the support surfaces while tangential force can be in any direction perpendicular to the corresponding compressive force.

Due to the presence of the aforementioned human-body/bicycle kinematic links, the human body acquires the appropriate posture for each angular position of the bicycle-crank. In the process of acquiring the appropriate posture, kinematics of the spine is adjusted in accordance with the so-called "*spinal rhythm*" algorithm. Within this algorithm, a single input, the pelvis-thorax angle, is used to determine the three rotational-joint angles of adjacent vertebrae (under a condition that the passive-elastic elements of the spine are able to force the spine to act kinematically as an elastic beam). The physical soundness of the spinal-rhythm algorithm for the seating posture has been validated by Rasmussen and de Zee using motion capture experiments [4.16].

In acquiring the sought posture for the human, an additional algorithm was employed. This algorithm controls the relative magnitudes of hip flexion and pelvis/thorax flexion. Following the experiments of Bell and Stigant [4.17], the ratio of the two angles was set to 2. That is, for a given value of the angle between the thorax and the thigh, the hip-joint flexion angle is twice that of the spine flexion angle.

IV.2.6 Musculoskeletal Definition of the Cycling Problem

To position the human body (overviewed in Section IV.2.3) onto the bicycle and have it drive the bicycle, laboratory experiments were conducted. Within these experiments, an experienced cyclist was instrumented with reflective markers on the outside of her thighs, knees, and ankles, Figure 4-1. After a bicycle specialist adjusted a raised-frame bicycle to match the anthropometry of the bicycle rider, the cyclist was asked to cycle at a comfortable speed (corresponding to the average cadence of 62 *rpm*). Meanwhile, motion capture measurements were carried out in order to locate and track the position of the reflective markers. The marker-position data recorded as a function of time were then used as input to the AnyBody Modeling System to drive the human body model during cycling, Figure 4-2.

Figure 4-1. Participant in the raised-frame-bicycle motion-capture experiments

IV.3. FINITE-ELEMENT AND DESIGN-OPTIMIZATION PROCEDURES

As mentioned earlier, the results of the musculoskeletal cycling analysis in the form of muscle forces and femur/hip and femur/knee joint reaction forces and moments, along with the spatial coordinates of the muscle attachment/via points and the two joints (as a function of time), are exported from the AnyBody Modeling System and used, as input, in a finite-element/design-optimization analysis of the distal femoral-fracture fixation-plate implant, Some details pertaining to the finite-element/design-optimization analysis are presented in the remainder of this section. In Figure 4-3, the names and the spatial locations of the muscle-attachment /via points and the hip and knee joints are provided for the right femur. In this figure, there are 27 muscle attachment/via points and two joint points. Moments are transferred to the femur only at the two joint points since muscles, being contractile linear elements, can each provide only a force.

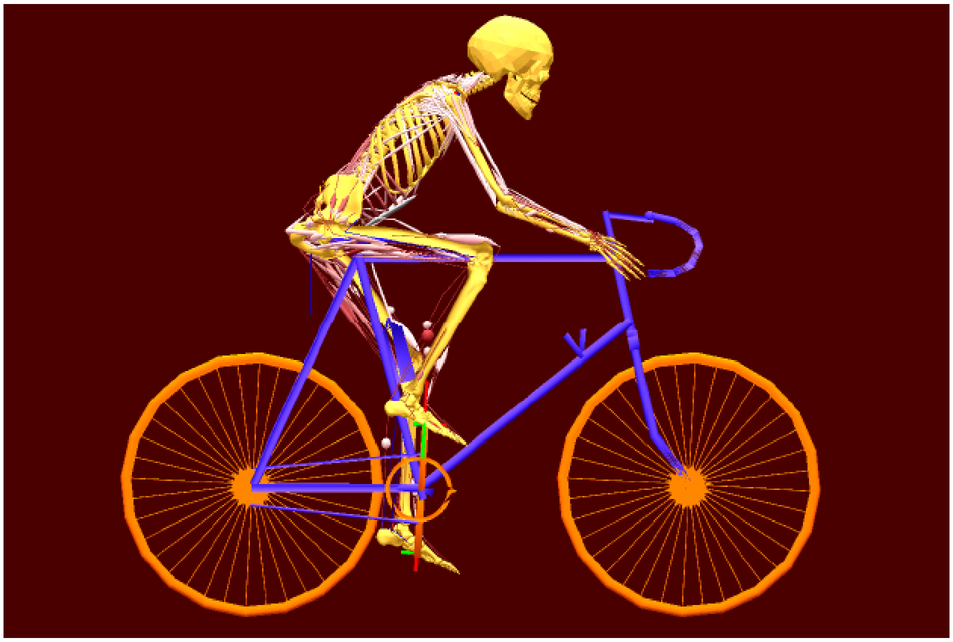

Figure 4-2. Scaled musculoskeletal model of a person riding a bicycle (not scaled to size).

In Figure 4-4, a close-up is provided of the right femur along with the adjoining bones. As can be seen, the femur contains a distal (next to the knee) fracture and it is fixed with a lateral fracture fixation-plate implant. The implant is attached to the two segments of the fractured femur using seven screws.

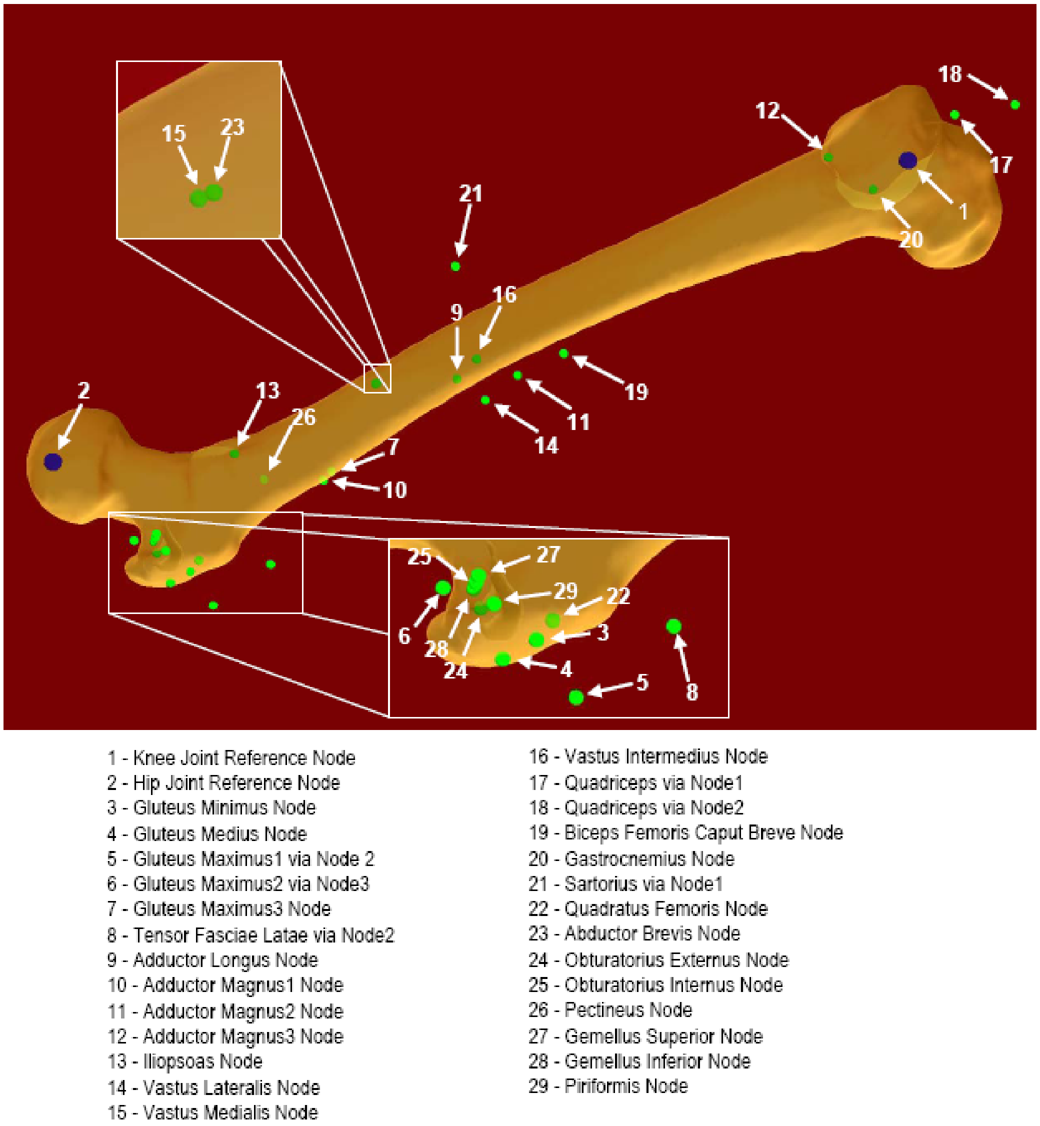

Figure 4-3. Spatial location of various muscle attachment points to the right femur.

IV.3.1. Finite Element Model and Analysis

The Model

The finite element model analyzed consisted of a fractured right femur, a fixation-plate implant and seven locking screws. Typical finite element meshes used are displayed in Figure 4-5. The femur, the plate and each of the screws were discretized using ca. 24,000

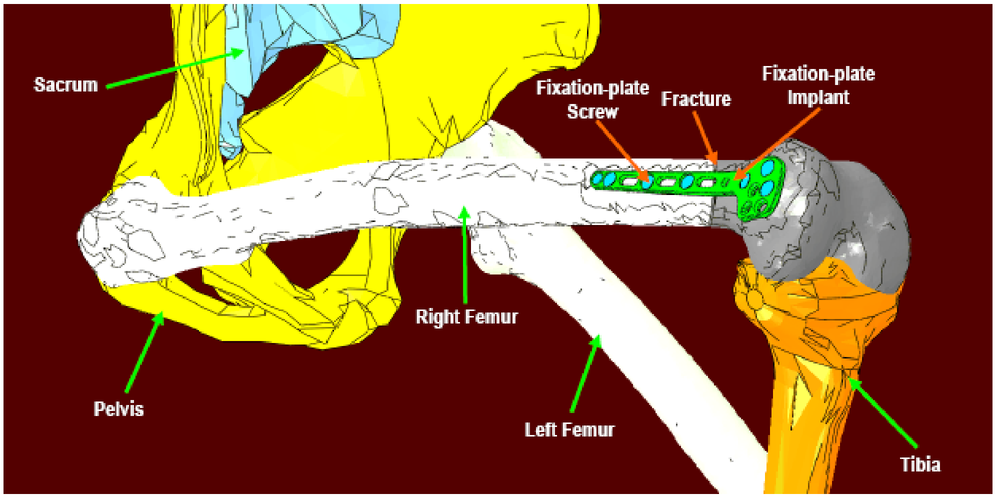

Figure 4-4. A close-up view of the fractured right femur (with a lateral fixation-plate implant and locking screws) and the adjoining bones at one time instant during a cycling-simulation run.

tetrahedral solid elements, ca. 9,000 tetrahedral solid elements and ca. 7,000 hexahedral solid elements, respectively.

To apply the muscle forces and joint-reaction forces and moments to the femur, each muscle-attachment/joint point is combined with a neighboring section of the femur surface to form a coupling. In this way, forces/moments acting at a muscle-attachment/joint point are transferred to the femur over a larger surface area preventing (unrealistic) stress-concentration artifacts.

To fasten the screws to the fixation plate and to the two bone segments, the outer surfaces of the screws are tied to the mating surfaces of the plate/femur. In other words, perfect fastening is assumed to have been achieved using the screws.

To prevent sections of the bottom surface of the fixation-plate implant between the screws from penetrating the femur, a "*penalty-type*" contact algorithm was employed. Within this algorithm, penetration of the contacting surfaces is opposed by a set of contact springs. Any level of contact pressure can be transmitted through the contact interface. Shear stresses are transmitted across the contact-interface in accordance with the Coulomb friction law.

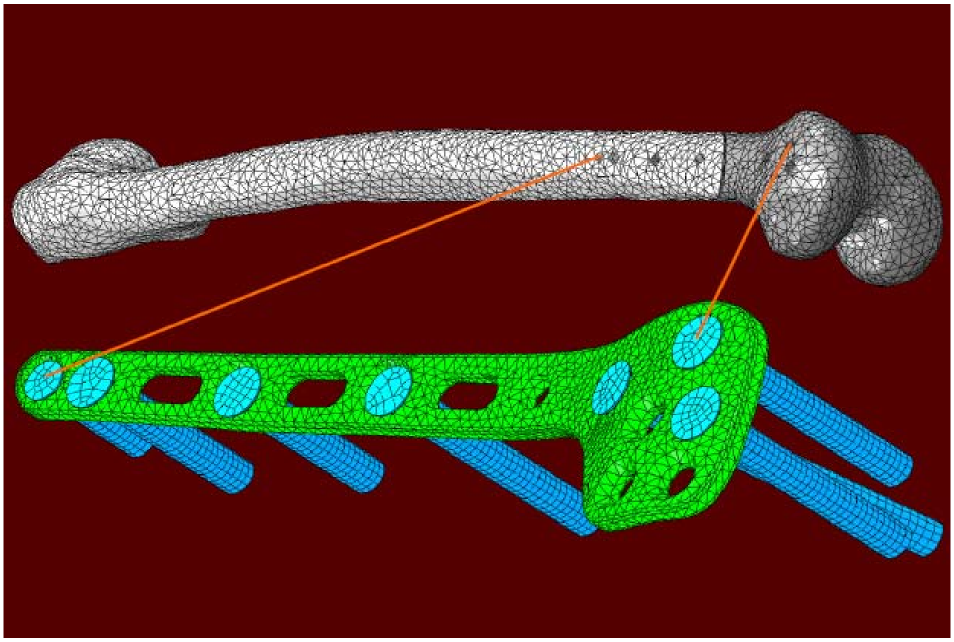

Figure 4-5. Typical finite-element meshes for the femur, fixation-plate implant and seven screws used in the quasi-static analysis of the implant longevity.

Material Models

The fixation-plate implant and the seven screws are assumed to be made of Ti-6Al-4V, a Ti-based alloy which is commonly used in fractured-bone fixation applications. Ti-6Al-4V is modeled as a linear-elastic/ideal-plastic material.

To provide a higher level of realism to the analysis, it is recognized that femur is built of two types of bone tissues (*cortical* and *trabecular*) and that density (and hence mechanical properties) of the two types of bone tissues are spatially non-uniform. To obtain the necessary data for defining the cortical-bone/trabecular-bone dividing surfaces and the spatial distribution of the density within each of the two bone tissues, Computed Tomography (CT) scans of the femur bone were analyzed [4.18]. An example of the CT scan of the femur bone is shown in Figure 4-6. For each bone tissue, the local gray-scale level is proportional to the local density. CT images like the one displayed in Figure 6 are analyzed using the Medical Imaging Software Mimics [4.19]. Within Mimics, the two bone tissues are differentiated by assigning two non-overlapping grayscale ranges, one for each bone tissue. Then, the gray-scale of each pixel within the two bone tissues is quantified using the Hounsfield Unit (*HU*) value. The latter are next converted into the corresponding bone-density values as: $\rho=1.9\ HU/1{,}700$, where the bone-density ρ is given in g/cm^3. Lastly, the relations listed in Table 4-1 in [4.18] were used to compute the young’s modulus as a function of the local density within the two bone tissues. A constant value of v = 0.3 was used for both bone tissues. No plasticity within the femur was considered. In other words, it was assumed that the femur was made of two isotropic heterogeneous linear-elastic materials.

The Analysis

The results of the AnyBody-based multi-body dynamic cycling analysis over a single revolution of the bicycle crank are exported at 100 equal time intervals. For each of these intervals, a quasi-static finite-element analysis of the femur/fixation-plate/screws assembly is carried out. At each of these time steps, the following AnyBody output information was used. (a) Spatial position of the femur/fixation-plate/screw assembly and the associated muscle-attachment and joint-reaction points; (b) muscle forces and joint-reaction forces and moments; and (c) the femur/plate/screws assembly (linear and angular) velocities and accelerations.

Table 4-1. Functional Relations Used to compute, from CT-scans, Density and the Young's Modulus in the Cortical and Trabecular Bones of the Radius.

Bone Region	**Density (ρ) vs.Hounsfield Unit (HU) Relationship**	**Young's Modulus (E) vs. Density (ρ) Relationship**
Cortical Bone	$\rho(g/cm^3) = 1.9\frac{HU}{1700}$	$E(MPa) = -13{,}430 + 1426\rho(g/cm^3)$
Trabecular Bone	$\rho(g/cm^3) = 1.9\frac{HU}{1700}$	$E(MPa) = 1310(\rho(g/cm^3))^{1.40}$

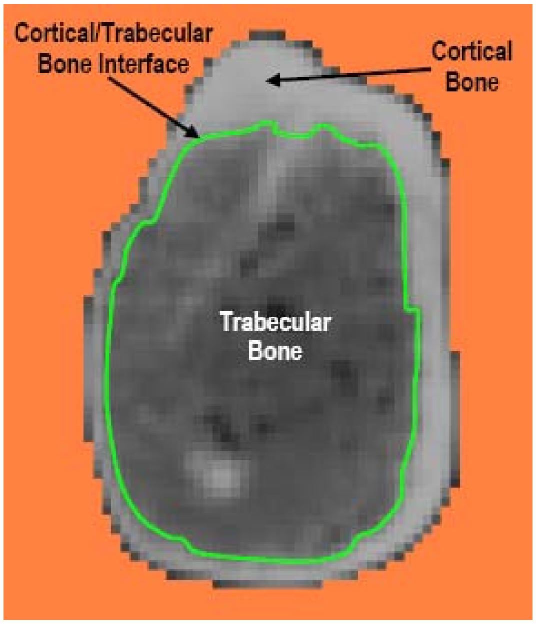

Figure 4-6. A typical computed tomography (CT) scan of the femur showing the presence of two bone tissues (cortical and trabecular bone tissues) and density variation within each bone-tissue.

The aforementioned AnyBody output data were used within the finite element model as follows: (a) the spatial position data were used to correctly position the finite-element model and the points for the application of concentrated forces and moments; (b) The muscle-force and joint-reaction force/moment data were used to define concentrated-load type of boundary conditions; and (c) The velocity and acceleration data were used to define distributed (gravity, inertia and centripetal) loading conditions.

The finite-element analysis results were used to determine: (a) if the fixation – plate implant has suffered (unacceptable) plastic deformation; (b) if the two contacting fractured surfaces of the femur have intruded into each other (also an unacceptable scenario); and (c) if the stress-state of the most critical elements (elements which control the fatigue life of the fixation-plate implant).

All the calculations pertaining to the quasi-static response of the femur/plate/screws assembly are done using ABAQUS/Standard, a commercially available general-purpose finite-element program [4.20].

IV.3.2. Design-Optimization Analysis

One of the main objectives of the present work was to carry out optimization of the femoral-fracture fixation plate implant design. For simplicity, the overall implant-design was assumed to remain fixed except for the plate thickness. Since the plate was modeled as a solid structure, changes in its thickness entailed re-meshing of this component during optimization. In addition, since the screws length also changed during optimization to comply with the plate thickness, the screws had to be re-meshed as well. In other words, while only the fixation-plate thickness was being altered, the optimization procedure was essentially a shape rather than a size based optimization.

IV.3.2.1. Structural Optimization

Structural optimization is a class of engineering optimization problems in which the evaluation of an objective function(s) or constraints requires the use of structural analyses (typically a finite element analysis, *FEA*). In compact form, the optimization problem can be symbolically defined as [4.21]:

Minimize the objective function $f(x)$

Subjected to the non-equality constraints $g(x) < 0$ and

to the equality constraints $h(x) = 0$

with the design variables x belonging to the domain D

where, in general, $g(x)$ and $h(x)$ are vector functions. The design variables x form a vector of parameters describing the geometry of a part/component. For example, x, $f(x)$, $g(x)$ and $h(x)$ can be part dimensions, part weight, a stress condition defining the onset of plastic yielding, and constraints on part dimensions, respectively. Depending on the nature of design variable in question, its domain D can be continuous, discrete or a mixture of the two. Furthermore, a structural optimization may have multiple objectives, in which case the objective function becomes a vector function.

Structural optimizations can be classified in many different ways. One of these classifications distinguishes between topology, size and shape optimization methods.

Topology Optimization: Topology optimization which is typically applied at the conceptual stage of part design represents the design domain as the continuum mixture of a solid material and "*voids*" and the optimal design is defined with respect to the distributions of the mixture density within the design space [e.g. 4.22].

Size Optimization: Within size optimization approach, the dimensions that describe part geometry are used as design variables, x. The application of size optimization is, consequently, mostly used at the detailed part-design stage where only fine tuning of the part geometry is necessary. Size optimization is typically quite straightforward and it generally requires no re-meshing of the finite element models during optimization iterations.

Shape Optimization: Shape optimization which is also mostly used at the detailed part-design stage, allows the changes in the boundary of part geometry. The boundaries are typically represented as smooth parametric curves/surfaces, since irregular boundaries typically deteriorate the accuracy of finite element analysis or may even cause the numerical instability of optimization algorithms. Because the product geometry can change dramatically during the optimization process, the automatic re-meshing of finite element models is usually required. Structural shape optimization methods are generally classified as: (a) direct geometry manipulation and (b) indirect geometry manipulation approaches. In the direct geometry manipulation approaches, design variable x is a vector of parameters representing the geometry of part boundary, e.g., the control points of the boundary surfaces. In the indirect geometry manipulation approaches, design variable x is a vector of parameters that indirectly defines the boundary of the product geometry. A comprehensive review of shape optimization based on the direct and the indirect geometry manipulation approaches can be found in Ref. [4.23].

IV.3.2.2. Fixation-plate Shape Optimization

The fixation-plate thickness optimization problem was defined as follows: The plate thickness is to be minimized while ensuring that during cycling no plastic deformation in the plate takes place, no interpenetration of the two fractured femur segments occur and that no high-cycle fatigue failure will take place after a preselected number of bicycle-crank revolutions (two million cycles, in accordance with a simple analysis presented in Section IV.4). Due to the three-dimensional nature of the fixation-plate implant, its thickness optimization was handled as a shape-optimization problem. Eight shape variables were used, one for the plate and the remaining ones for each of the seven screws of the fixation-plate. Each shape variable enables a proportional change in the geometry of the associated component while ensuring a high-quality of their finite-element mesh. This was accomplished by using mesh-morphing algorithm which preserves identity of the nodes and elements while simply repositioning the nodes. The fixation-plate thickness-optimization problem was implemented into and solved using HyperStudy [4.24], a general purpose multi-disciplinary multi-objective optimization software. For a defined optimization problem, this software invokes the pre-selected optimization algorithm (the Adaptive Response Surface Method [4.25], in the present case), morphs the component meshes, prepares an input file for the finite-element analysis, launches the finite-element solver and reads and interprets the finite-element results in order to determine the immediate direction of the design-optimization process.

IV.3.2.3. Fatigue-life Prediction

As mentioned earlier, one of the fixation-plate design-optimization constraints pertains to the attainment of a pre-selected lifecycle. Since this lifecycle is expected to be high-cycle fatigue controlled, a fatigue-based lifecycle prediction procedure had to be developed in the present work. The first step in this direction was to examine the temporal behavior of the muscle forces and reaction forces and moments during a single revolution of the bicycle crank. An example of the results obtained for the two joint-reaction force and moment components is displayed in Figures 4-7(a) & 4-7(b). Simple examination of the results displayed in these figures show that the temporal evolution of various forces and moments is not in phase and that these forces/moments are not associated with constant amplitude. These findings have important consequences to the type of fatigue life prediction analysis which should be employed. Firstly, the non-

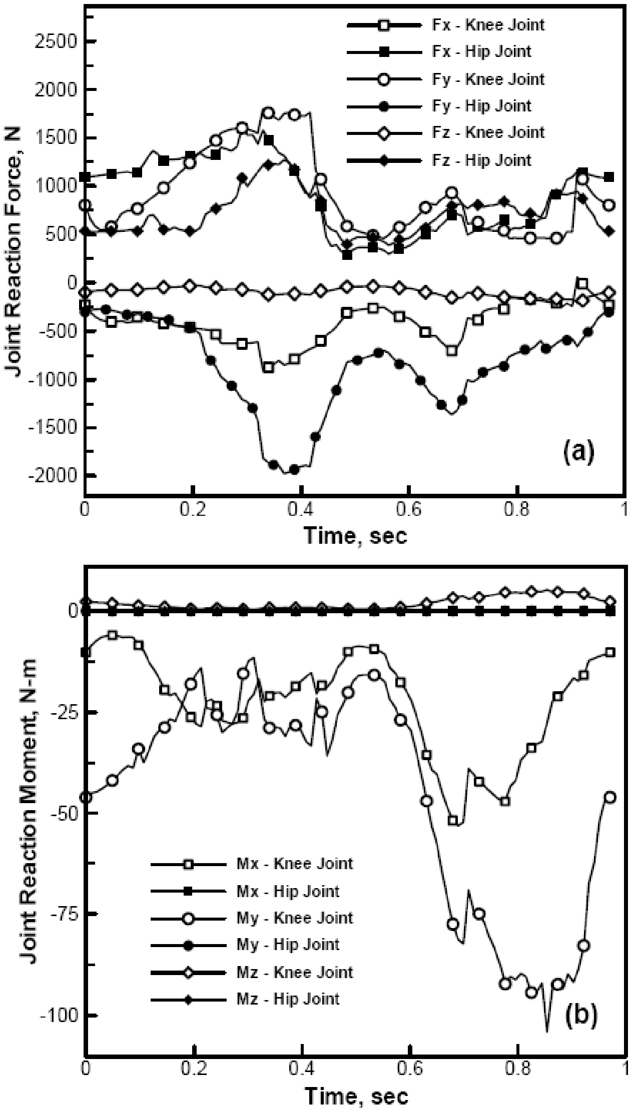

Figure 4-7. Temporal evolution of the hip and knee joint reaction forces and moments over a single revolution of the bicycle crank.

constant nature of the load amplitude implies that a cycle-counting procedure (e.g. the so-called *Rainflow Cycle-counting Analysis* [4.26]) should be employed in order to represent (highly-irregular) time-dependent loading as a collection of constant-amplitude (fixed mean-value) loading cycles. Secondly, since temporal evolution of the various muscle forces and joint-reaction forces and moments are out of phase, not only the magnitude of stresses/strains at an arbitrary point in the femur/plate/screw assembly varies as a function of time, but also the orientation of the associated principal coordinate system is time variant. The latter findings are what make the loading "*non-proportional*" and the fatigue-life prediction more complex. Specifically, the rain-flow cycle-counting analysis to be used should differentiate the load cycles not only on the basis of their amplitude and the mean value but also on the basis of the orientation of their stress/strain principal coordinate system.

High-cycle Stress-based Fatigue Analysis.

Due to a relatively simple geometry of the fixation-plate implant and the fact that a pre-defined high-cycle fatigue life is mandated for this component, it was deemed reasonable to assume that the fatigue-life of this component will be stress controlled. Furthermore it is assumed that the stress-based function responsible for the fatigue-induced failure is the maximum principal (tensile) stress. Next, stress-amplitude dependence of the number of cycles till failure is assumed to be defined by the traditional Basquin relation [e.g. 4.27] and the effect of the mean value of the maximum principal (tensile) stress is accounted for through the use of Goodman relation [e.g. 4.27]. The high-cycle fatigue parameters for Ti-6Al-4V are obtained from the Ansys fatigue material database [4.28].

High-cycle Stress-based Fatigue Analysis

To compute the number of cycles till failure for the given design/ thickness of the fixation-plate implant, the procedure developed in our previous work was utilized [4.29]. Due to space limitations, only a brief overview of this procedure will be provided here.

The main steps of this procedure applied to each finite element of the fixation-plate implant include: (a) utilization of the finite-element calculation results to determine temporal evolution of the maximum principal (tensile) stress; (b) application of the rain-flow cycle counting analysis to determine a three dimensional histogram relating the number of cycles with the maximum principal stress amplitude and the associated mean value; (c) calculation of the fractional damage associated with each load-cycle type (as characterized by a fixed value of the stress amplitude and the stress mean value); and (d) computation of the total fractional damage associated with all load-cycle types and computation of the corresponding number of cycles till failure as an inverse of this fractional damage.

The fixation-plate implant life cycle is then set to that of its element associated with the smallest number of cycle till failure.

IV.4. RESULTS AND DISCUSSION

IV.4.1. Musculoskeletal Cycling Analysis

As mentioned earlier the sole purpose of conducting the musculoskeletal cycling analysis was to obtain physiologically realistic loading conditions for the femur/fixation-plate/screws assembly. Specifically, at each of 100 time increment during a single rotation of the bicycle crank, the muscle forces and the joint reaction forces and moments as well as the spatial position of the muscle attachment/via points and the joint-reaction points had to be obtained from the musculoskeletal analysis. In addition, the spatial position and the orientation of the femur/plate/screws assembly at each time increment had to be obtained from the musculoskeletal analysis.

An example of the temporal evolution of the forces and moments acting on the femur (at the hip and knee joint points) was shown earlier, Figures 4-7(a) & (b). Similar results were obtained at muscle attachment/via points. As pointed out earlier these forces and moments are of non-constant amplitude and not in-phase resulting in non-proportional type of loading on the femur.

An example of the whole human-body/bicycle kinematics/muscle-activity results at four time intervals during a single revolution of the bicycle crank is shown in Figures 4-8(a) - (d). It should be noted that the activity of each muscle (i.e. the force produced by the muscle) is displayed pictorially in these figures by the thickness and the color shading of the line segments representing the muscles. The results displayed in Figures 4-8(a) - (d) then can be used to qualitatively assess how the activity/recruitment of different muscles is changing during a single revolution of the bicycle crank for e.g., variation in the activity of the *Biceps Femoris Caput Longum* muscle is marked in these figures.

IV.4.2. Finite Element Results

Since it was assumed throughout this work that the locking screws can secure well the fixation-plate implant to the two fractured-femur segments, the focus of the finite-element investigation was placed on the fixation-plate implant. The three primary functional requirements imposed onto the implant were: (a) sufficiently high strength to prevent any plastic deformation within the fixation plate; (b) adequate bending stiffness to prevent the two femur segments from intruding into each other; and (c) a pre-selected fatigue life expressed as a number of bicycle crank revolutions. Using an expected

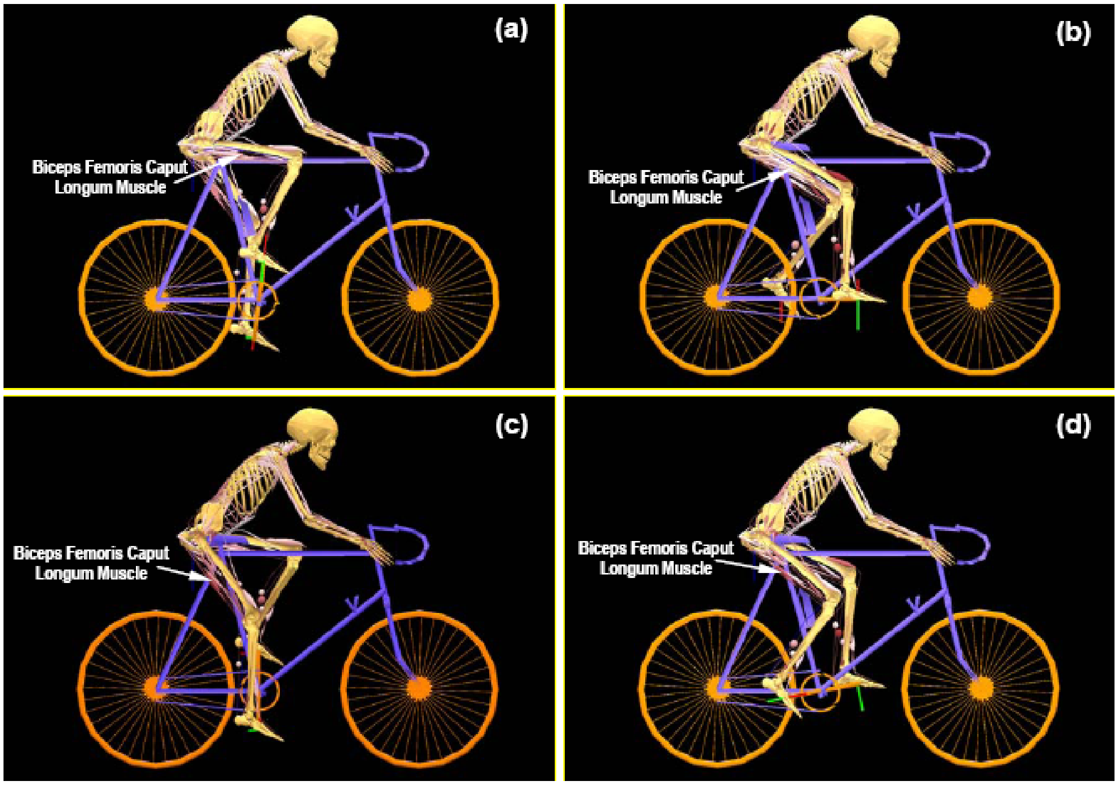

Figure 4-8. Temporal evolution of the human-body kinematics and muscles activity at four equally-spaced times during a single bicycle-crank revolution.

implant resident time of 6 years and an average cycling distance of 1,000km/year the implant fatigue life was set to two million cycles.

An example of the typical finite-element results is displayed in Figures 4-9(a) & (b). The results shown in Figure 4-9(a) show that the von-Mises equivalent stress is substantially lower than the Ti-6Al-4V yield strength (930*MPa*). Thus under all the loading and fixation-plate design conditions the implant strength requirement was found to be met. Likewise, the conditions regarding the maximum interpenetration of the fracture surfaces of the femur was found to be satisfied (i.e. <0.001*m*) for all combinations of loading conditions and the fixation-plate thickness. As far as the

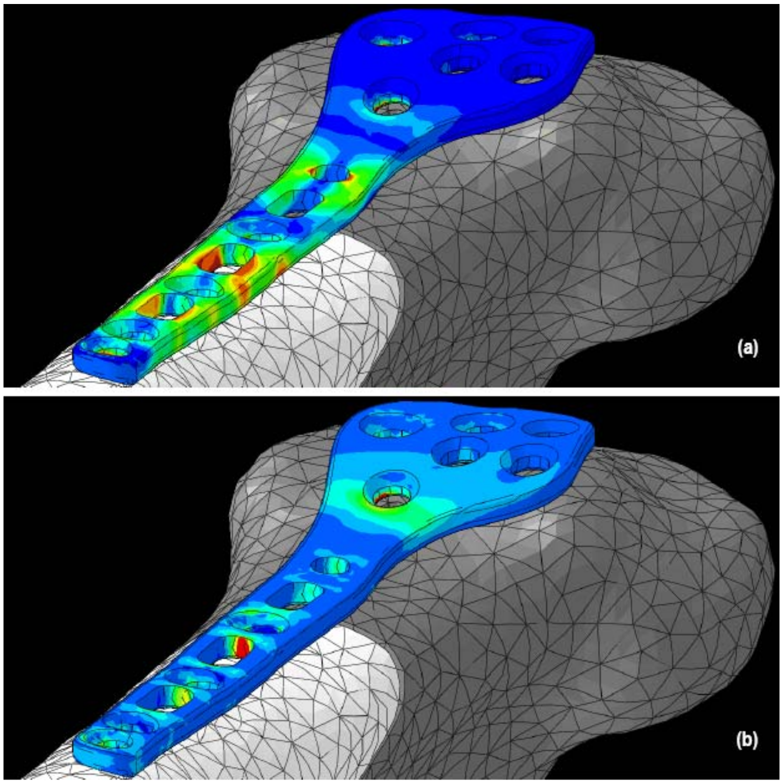

Figure 4-9. Typical results pertaining to the spatial distribution of: (a) von-Mises equivalent stress (red=30*Mpa* and blue=0.1*Mpa*); and (b) maximum principal stress (red=20*Mpa* and blue=-3*Mpa*).

fixation-plate implant fatigue-life requirements is concerned, it is found to be satisfied at the implant-thickness upper-bound (4.25*mm*) and not to be satisfied at the implant thickness lower-bound (3.25*mm*). As mentioned earlier the fatigue-life in the present case is controlled by the maximum principal stress. Figure 4-9(b) displays an example of the typical results pertaining to spatial distribution of this stress component. Clearly the elements surrounding some of the screw-holes are associated with the highest levels of the maximum principal stress and are likely to control the overall fatigue-life of the component.

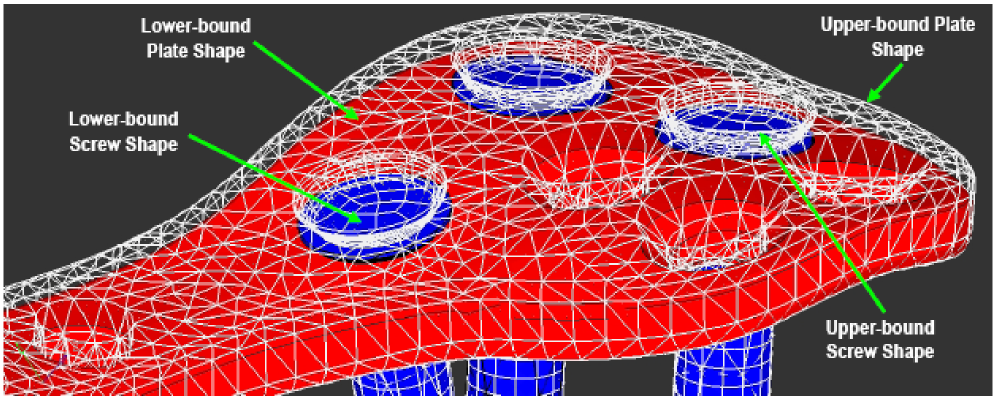

Figure 4-10. Upper-bound (wireframe) and lower-bound (shaded red for the plate and blue for the locking screws) shapes used in the fixation-plate thickness design optimization analysis.

IV.4.3. Design Optimization Results

As stated earlier, under all the implant-design and muscle/joint-imposed loading conditions, the functional requirements for the implant pertaining to its strength and bending stiffness were found to be satisfied. Hence, they will not be considered any further. The focus will be placed in this section on the functional requirement pertaining to the fatigue-life of the implant.

In accordance with the discussion presented in Section IV.3.2, the implant-thickness optimization problem was treated as a shape-design optimization problem. The implant thickness was defined as a single implant-shape variable. Definition of this shape variable is depicted in Figure 4-10. Additionally, the corresponding seven shape variables were defined (only three shown for brevity), one for each locking screw, in order to ensure that screws length is consistent with the implant thickness.

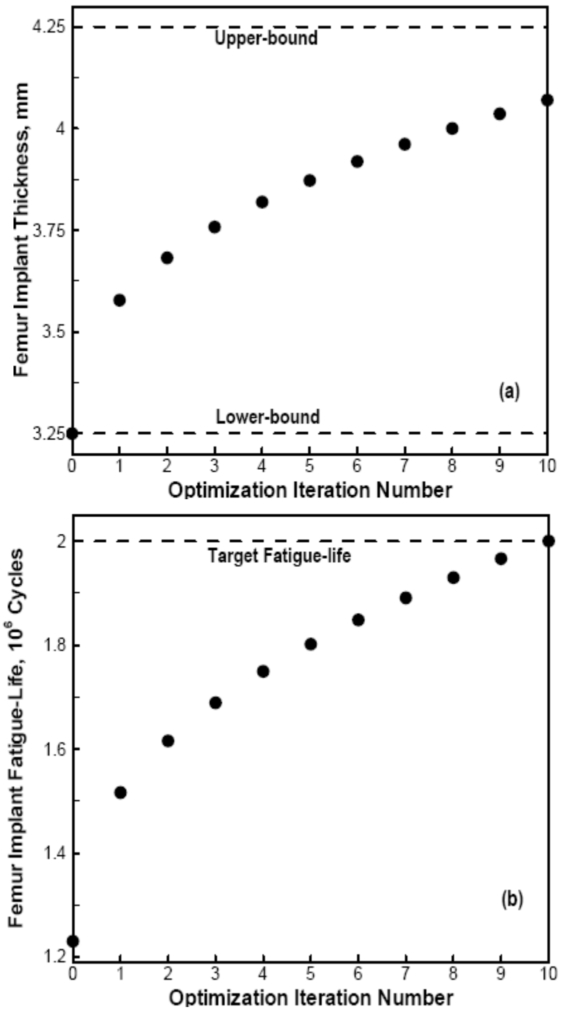

Figure 4-11. Variations of: (a) the femur fixation-plate implant thickness; and (b) femur implant fatigue-life, with the successive design-optimization iteration numbers.

The progress of the implant thickness optimization is displayed in Figures 4-11(a) & (b). In Figure 4-11(a), implant thickness is tracked as a function of the iteration number. In Figure 4-11(b), on the other hand, the implant fatigue life is monitored as a function of the optimization iteration number. The results displayed in Figures 4-11(a) & (b) show that the optimal thickness of the fractured-femur fixation-plate implant is around 4.07*mm*.

IV.4.4. Material Selection

Until this point in the present investigation, the same implant material, Ti-6Al-4V STA (*Solution Treated and Aged*) alloy was used. This is a commonly used fractured-femur fixation-plate implant material which provides a good combination of biocompatibility, mechanical performance and a low material/manufacturing cost. The present investigation has established that the key performance aspect of the fixation-plate implant under consideration is fatigue life. While retaining the requirements concerning low material/manufacturing cost and bio-compatibility (ensured by carrying out material selection within the family of Ti-based alloys), a material selection procedure was conducted in the present work in order to identify potential material substitutes for Ti-6Al-4V.

While examining different Ti-based material alternatives, it was found that in all cases considered, strength requirement can be readily attained. Consequently implant-material selection is carried out with respect to simultaneously, satisfying the implant stiffness and longevity requirements. In all the cases considered, it was found that the longevity requirement is more difficult to meet. Consequently, in defining a single material selection parameter, a higher weighting factor (w_{EL}=0.8) was selected for endurance limit and a lower weighting factor (w_{YM}=0.2) for the Young's modulus of the candidate material. For convenience, the endurance limit and then Young's modulus of each candidate material are normalized by their respective counterparts in Ti-6Al-4V. Thus, the material selection index for the fixation-plate implant is defined as:

$$M = w_{EL}\frac{\sigma_{EL}}{\sigma_{EL,Ti-6Al-4V}} + w_{YM}\frac{E}{E_{Ti-6Al-4V}} \tag{4.5}$$

where σ_{EL} denotes endurance limit while E is the Young's modulus.

Clearly, M = 1.0 for Ti-6Al-4V and for a material to be considered as a potential substitute for Ti-6Al-4V, its M must be larger than 1.0.

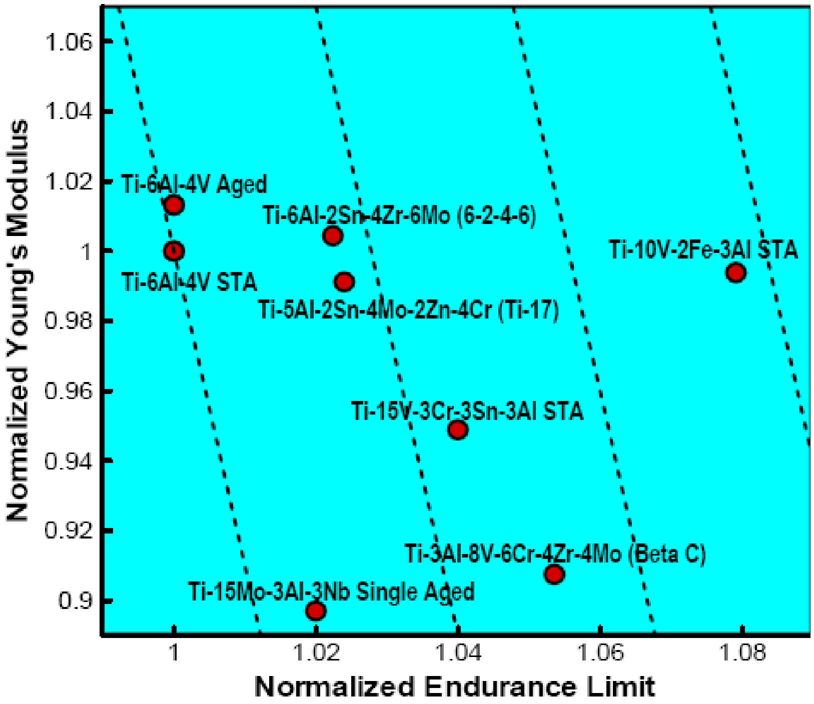

Figure 4-12. Material selection chart used in the analysis of potential replacement of Ti-6Al-4V as the fixation-plate implant material with other Ti-based alloys.

To assist the implant material-selection process, a normalized stiffness ($E/E_{Ti\text{-}6Al\text{-}4V}$) vs. normalized endurance limit ($\sigma/_{\sigma Ti\text{-}6Al\text{-}4V}$) plot is constructed in Figure 4-12. Few iso-M lines are also drawn in this figure. The results displayed in Figure 4-12 show that, with respect to the implant performance (as defined by its strength, stiffness, and longevity), Ti-10V-2Fe-3Al STA, Ti-3Al-8V-6Cr-4Zr-4Mo (Beta C) or Ti-15V-3Cr-3Sn-3Al STA may be a better alternative for the implant than Ti-6Al-4V. However, the final decision regarding the substitution of Ti-6Al-4V with these material alternatives should also account for material/manufacturing cost. Due to a lack of reliable/stable data pertaining to the cost of the materials in question, the effect of cost on material selection could not be taken into account in the present work.

IV.5. SUMMARY AND CONCLUSIONS

Based on the work conducted and the results obtained in the present investigation, the following main summary remarks and conclusions can be drawn:

1. Design (more specifically thickness) optimization of a fractured-femur fixation-plate implant is investigated computationally. To provide the realistic physiological loading conditions experienced by the implant during normal daily activities of the patient, a musculoskeletal multi-body dynamics analysis is coupled with implant finite-element/design-optimization methods.

2. The results show that out of the three functional requirements placed on the implant, (i.e. its strength, bending stiffness and longevity), it is longevity which typically controls the implant optimal design/thickness.

3. Under the assumption that bicycle riding provides the most critical loading conditions experienced by the femur-fixation implant during normal daily activities of the human with a surgically implanted femur-fixation plate, the optimal implant thickness was determined.

4. Potential material replacements have been considered for Ti-6Al-4V, the alloy used in the present finite-element/design-optimization analysis of a femur-fixation implant, in order to further reduce implant thickness.

REFERENCES

[4.1]. K. C. Kim, J. K. Lee, D. S. Hwang, J. Y. Yang, Y. M. Kim, “*Distal Hybrid Interlocking in the Femoral Shaft Fracture,*” Orthopedics, 30:605, 2007.

[4.2]. M. Sivasankar, S. K. Dwivedy, D. Chakraborty, “*Fatigue Analysis of Artificial Hip Joints for Different Activities,*” 2nd International Congress on Computational Mechanics and Simulation, Guwahati, India, 2006.

[4.3]. D. D. D’Lima, N. Steklov, B. J. Fregly, S. A. Banks, C.W. Colwell Jr., “*In Vivo Contact Stresses during Activities of Daily Living after Knee Arthroplasty,*” J Orthop Res, 26, 2008.

[4.4]. L. Cristofolini, P. Savigni, A. S. Teutonico, M. Viceconti, “*In Vitro Load History to Evaluate the Effects of Daily Activities on Cemented Hip Implants,*” Acta of Bioengineering and Biomechanics, 5(2), 2003.

[4.5]. D. O. O'Connor, D. W. Burke, M. Jasty, R. C. Sedlacek, W. H. Harris, “*In vitro measurement of strain in the bone cement surrounding the femoral component of total hip replacements during simulated gait and stair-climbing,*” J Orthop Res, 14(5), 1996.

[4.6]. *AnyBody 3.0*, AnyBody Technology A/S, Aalborg, Denmark, 2008.

[4.7]. M. Damsgaard, J. Rasmussen, S.T. Christensen, E. Surma and M. de Zee, “*Analysis of Musculoskeletal Systems in the AnyBody Modeling System,*” Simul. Model. Pract. Theory, 14, 2006, 1100–1111.

[4.8]. J. Rasmussen and M. de Zee, “*Design Optimization of Airline Seats,*” SAE Conference, SAE no. 2008-01-1863, 2008.

[4.9]. S. Dendorfer and S. Torholm, “*Final Report on Feasibility Study,*” Report no: 21385/08/NL/PA, presented to ESTEC/ESA by AnyBody Technology A/S, May, 2008.

[4.10]. *AnyScript Model Repository 7.1*, AnyBody 3.0, AnyBody Technology A/S, Aalborg, Denmark, 2009.

[4.11]. F.C.T. Van der Helm, “*A Finite Element Musculoskeletal Model of the Human Shoulder Mechanism,*” J. Biomech., 27, 1994, 551–569.

[4.12]. M. de Zee, L. Hansen, C. Wong, J. Rasmussen and E.B. Simonsen, "*A Generic Detailed Rigid-body Lumbar Spine Model,*" J. Biomech., 40, 2007, 1219–1227.

[4.13]. H. Wilke, P. Neef, B. Hinz, H. Seidel and L. Claes, "*Intradiscal Pressure Together with Anthropometric Data – a Data Set for the Validation of Models,*" Clin Biomech., 16 (Suppl. 1), 2001, S111–S126.

[4.14]. P. de Jong, M. de Zee, P.A.J. Hilbers, H.H.C.M. Savelberg, F.N. van de Vosse, A. Wagemakers and K. Meijer, "*Multi-body Modeling of Recumbent Cycling: An Optimization of Configuration and Cadence,*" Master's Thesis Medica Engineering, TU/e Biomodelling and Bioinformatics, University of Maastricht, Movement Sciences, Aalborg University, 2006.

[4.15]. K.N. An, B.M. Kwak, E.Y. Chao and B.F. Morrey, "*Determination of Muscle and Joint Forces: A New Technique to Solve the Indeterminate Problem,*" J. Biomech. Eng., 106, 1984, 364–367.

[4.16]. J. Rasmussen, S. Torholm and M. de Zee, "*Computational Analysis of the Influence of Seat Pan Inclination and Friction on Muscle Activity and Spinal Joint Forces,*" International Journal of Industrial Ergonomics, 39, 2009, 52-57.

[4.17]. J. A. Bell and M. Stigant, "*Development of a Fibre Optic Goniometer System to Measure Lumbar and Hip Movement to Detect Activities and their Lumbar Postures,*" J. Med. Eng. Technol., 31, 2007, 361–366.

[4.18]. Z. Yosibash, R. Padan, L. Joscowicz, C. Milgrom, "*A CT-based high-order finite element analysis of the human proximal femur compared to in-vitro experiments,"* ASME, Journal of Biomechanical Engineering, 129 (3), 297–309, 2007.

[4.19]. *Mimics*, Medical Imaging Software, Materialise, User Documentation, 2009

[4.20]. *ABAQUS Version 6.8-1*, User Documentation, Dassault Systems, 2009.

[4.21]. P. Y. Papalambros and D. J. Wilde, "*Principles of Optimal Design: Modeling and Computation,*" Cambridge University Press, 2000, 2nd ed., Cambridge, UK.

[4.22]. M. P. Bendsoe and N. Kikuchi, "*Generating Optimal Topologies in Structural Design Using a Homogenization Method,*" Comput. Methods Appl. Mech. Eng., 1988, 71 2 , pp. 197-224.

[4.23]. R. T. Haftka and R. V. Grandhi, "*Structural Shape Optimization: A Survey,*" Comput. Methods Appl. Mech. Eng., 1986, 57(1), pp. 91-106.

[4.24]. "*HyperStudy, User Manual*", Altair Engineering Inc., Troy, MI, 2009.

[4.25]. U. Schramm, "*Multi-Disciplinary Optimization for NVH and Crashworthiness,*" Altair Engineering Inc., Troy, MI, 2007.

[4.26]. M. Matsuishi, T. Endo, "*Fatigue of Metals subjected to Varying Stress,*" Proceedings of Kyushi Branch, 1987.

[4.27]. P. Brondsted, H. Lilholt, A. Lystrup, "*Composite Materials for Wind Power Turbine Blades,*" Annual Review of Materials Research, 35:505-38, 2005

[4.28]. *ANSYS Version 12*, User Documentation, Ansys Inc., 2009.

[4.29]. M. Grujicic, G. Arakere, W. C. Bell, H. Marvi, H. V. Yalavarthy, B. Pandurangan, I. Haque and G. M. Fadel, "*Reliability-based Design Optimization for Durability of Ground-vehicle Suspension-system Components,*" Journal of Materials Engineering and Performance, accepted for publication, April 2009.

CHAPTER FIVE

DESIGN-OPTIMIZATION AND MATERIAL SELECTION FOR A PROXIMAL RADIUS FRACTURE-FIXATION IMPLANT

ABSTRACT

The problem of optimal size, shape and placement of a proximal radius-fracture fixation-plate is addressed computationally using a combined finite-element/design-optimization procedure. To expand the set of physiological loading conditions experienced by the implant during normal everyday activities of the patient, beyond those typically covered by the pre-clinical implant-evaluation testing procedures, the case of a wheel-chair push exertion is considered. Toward that end, a musculoskeletal multi-body inverse-dynamics analysis is carried out of a human propelling a wheelchair. The results obtained are used as input to finite-element structural analyses for evaluation of the maximum stress and fatigue life of the parametrically defined implant design. While optimizing the design of the radius-fracture fixation-plate, realistic functional requirements pertaining to the attainment of the required level of the devise safety factor and longevity/lifecycle were considered. It is argued that the type of analyses employed in the present work should be: (a) used to complement the standard experimental pre-clinical implant-evaluation tests (the tests which normally include a limited number of daily-living physiological loading conditions and which rely on single pass/fail outcomes/decisions with respect to a set of lower-bound implant-performance criteria)

and (b) integrated early in the implant design and material/manufacturing route selection process.

V.1. INTRODUCTION

It is common practice nowadays to judge the success of a surgery involving an implantable device (e.g. radius-or femoral-fracture fixation-plate implant, total hip replacement, etc.) by how quickly the patient can return to his/her normal activities of daily living following the surgical procedure [5.1]. Another measure of the success of these surgeries is the longevity of the implanted device subjected to the physiological forces associated with the normal daily activities performed by the patient. However, as people are living longer and continuing to maintain active lifestyles, the paradigm of "*everyday activities*" must also evolve. This is critical since physiological loading conditions associated with these daily activities should be included in the pre-clinical implant-evaluation testing procedures. For example, long-term fatigue-controlled stability of hip implants has been evaluated under the conditions of normal walking [5.2, 5.3, 5.5], sit-to-stand [5.2], and stair climbing [5.3, 5.5] and in a combination of these daily activities [5.4]. However, only a relatively small number of the physiological loading conditions (derived from everyday activities of the patient), such as the ones just mentioned, are normally covered by the pre-clinical implant evaluation studies. The main reason for this is that the inclusion of more complex physiological loading conditions in the experimental pre-clinical implant evaluation testing procedures could be quite challenging and costly.

The additional shortcoming of the current pre-clinical implant evaluation studies is that they are used to mainly evaluate already designed and manufactured implant devices. This ensures that these devices will meet a predefined set of functional and longevity criteria. However, the results of these tests, unless the devise has failed to meet the performance/longevity criteria, are rarely integrated in the overall implant-design process. Consequently what is left unanswered is if the accepted new implant can meet the performance and longevity requirements under other physiological loading conditions associated with normal daily living and if the design (including the material selected for the implant) is optimal (with respect to its size, shape, placement, weight, cost, etc.).

The main objective of the present work is to demonstrate how musculoskeletal modeling can be used to generate physiological loading conditions not normally covered by the pre-clinical implant-evaluation tests, although they may be associated with the fairly normal daily activities. Within the present work, the recently-developed novel technology for computer modeling of the human-body mechanics and dynamics, namely the AnyBody Modeling System [5.6] and its associated public domain library of body models are being fully utilized and further developed. In its most recent rendition [5.7], the AnyBody Modeling System enables creation of a detailed computer model for the human body (including all important components of the musculoskeletal system) as well as examination of the influence of different postures and the environment on the internal joint forces and muscle activity.

The second main objective of the present paper is to demonstrate how the loading conditions derived using musculoskeletal modeling can be utilized within a combined finite-element/design-optimization procedure to carry out optimization of the design of an implanted device. Specifically, optimal thickness, angular size and placement of a proximal radius-fracture fixation-plate under wheel-chair push exertion loading conditions is investigated. Optimization of the implant thickness, angular size and placement is carried out with respect to its ability to meet several functional requirements pertaining to both the necessary level of fractured-radius fixation and to meeting the longevity/lifespan constraints. Details regarding these functional requirements are presented in the next section.

The organization of the paper is as follows. A brief overview of the AnyBody Modeling System is provided in Section V.2.1. The musculoskeletal human-body model, the concepts of muscle recruitment and muscle activity envelope, the wheel-chair model and the issues related to human/wheel-chair kinematics and contact interactions are discussed in Sections V.2.2 - V.2.5. The definition of the musculoskeletal problem of a human propelling the wheel-chair analyzed in the present work is discussed in Section V.2.6. The finite-element/design-optimization problem and analysis for the proximal radius-fracture fixation-plate implant are presented in Section V.3. The results obtained in the present work are presented and discussed in Section V.4. The main conclusions resulting from the present work are summarized in Section V.5.

V.2. MUSCULOSKELETAL MODELING AND SIMULATIONS

Within the present work, two distinct computational analyses are carried out. Within the first analysis (discussed in this section), a musculoskeletal investigation of a person propelling a wheel-chair is carried out. The resulting forces, moments, angular velocities and angular accelerations, as functions of the time, acting on the fractured right radius of the person propelling the wheel-chair are next used in a finite-element/design-optimization analysis of the proximal radius-fracture fixation-plate implant.

V.2.1. The AnyBody Modeling System [4.6]

All the musculoskeletal modeling and simulation analyses carried out in the present work were done using the AnyBody Modeling System [5.6] developed at Aalborg University. The essential features of this computer program can be summarized as follows:

(a) The musculoskeletal model is typically constructed as a standard multi-body dynamics model consisting of rigid bodies, kinematic joints, kinematic drivers and force/moment actuators (i.e. muscles). The kinematic and dynamic behavior of this model can be determined using standard multi-body dynamics simulation methods;

(b) Complex geometries of the muscles and their spatial arrangement/ interactions (e.g. muscles wrapping around other muscles, bones, ligaments, etc.) can be readily modeled within AnyBody Modeling System [5.6];

(c) It is well-established that a typical musculoskeletal system suffers from the so-called *"muscle redundancy problem"*: i.e. the number of muscles available is generally larger than those needed to drive various body joints. Within the living humans and animals, this problem is handled by their Central Nervous System (*CNS*) which controls muscles activation/recruitment. To mimic this role of the CNS, the AnyBody Modeling System [5.6] offers the choice of several optimization-based muscle-recruitment algorithms;

(d) A typical musculoskeletal multi-body dynamics problem is solved using one of the computationally-efficient inverse dynamics methods within which the desired body motion is prescribed while the muscle forces required to produce this motion is computed;

(e) Within the AnyBody Modeling System [5.6], the muscle recruitment problem is solved using an optimization-based approach in the form:

Minimize the objective function:

$$G(f^{(M)}) \tag{5.1}$$

Subjected to the following constraints:

$$Cf = d \tag{5.2}$$

$$f_i^{(M)} \geq 0,\ i \in \{1,\ldots,n^{(M)}\} \tag{5.3}$$

where the objective function G (a scalar function of the vector of $n^{(M)}$ unknown muscle forces, $f^{(M)}$), defines the minimization object of the selected muscle-recruitment criterion (assumed to mimic the one used by the CNS). Eq. 5.2 defines the condition for dynamic mechanical equilibrium where C is the coefficient matrix for the "*unknown*" forces/moments in the system while d is a vector of the "*known*" (applied or inertia) forces. The forces appearing in vector f in Eq. 5.2 include the unknown muscle forces, $f^{(M)}$, and the joint-reaction forces, $f^{(R)}$. Eq. 5.3 simply states that muscles can only pull (not push) and that the upper bound for the force in each muscle $f_i^{(M)}{}_i$ is the corresponding muscle strength, N_i;

(f) While there are a number of functional forms for the objective function, *G,* the one used in the present work is the so-called "*min/max*" form within which the objective function (to be minimized) is defined as the maximum muscle activity defined for each muscle *i* as $f_i^{(M)}/N_i$, i.e. ;

$$G(f^{(M)}) = \max(f_i^{(M)} / N_i); \tag{5.4}$$

This formulation offers several numerical advantages over other popular forms of *G* and, in addition, it appears to be physiologically sound. That is, under the assumption that muscle fatigue is directly proportional to its activity, Eqs. 5.1 and 5.4 essentially state that muscle recruitment is based on a minimum muscle-fatigue criterion. Also, this expression for *G* has been found to asymptotically approach other formulations of *G* (e.g. the so-called "*Polynomial*" form [5.8]).

(g) The problem defined by Eqs. 5.1 – 5.4 can be linearized using the so-called "*bound formulation*" [5.9] resulting in a linear programming problem with muscle forces and joint reaction forces as free variables. Relations between these two types of forces are next used to eliminate the joint reaction forces yielding a linear programming problem with the number of unknowns equal to the number of muscles in the system; and

(h) While for a fairly detailed full-body model containing around one thousand muscles, this constitutes a medium-to-large size problem which can be readily solved by a variety of design-optimization methods (e.g. Simplex, Interior-point methods, etc.), the min/max problem is inherently indeterminate and must be solved iteratively. This can be rationalized as follows: The min/max criterion only deals with the maximally-activated muscles and with muscles which help support the maximally-activated muscles. Since the system, in general, may contain muscles that have no influence on the maximum muscle activity in the system, the forces in these muscles are left undetermined by the min/max formulation presented above. To overcome this shortcoming, the muscle-recruitment optimization problem is solved iteratively, so that each iteration eliminates the muscles with uniquely determined forces and the procedure is repeated until all muscle forces are determined.

V.2.2. Musculoskeletal Human-body Model

The human body musculoskeletal model used in the present work was downloaded from the public domain AnyScript Model Repository [5.10]. The model was originally constructed by AnyBody Technology using the AnyBody Modeling System [5.6] following the procedure described in details by Damsgaard et al. [5.7].

Model Taxonomy: The musculoskeletal human-body model includes: (a) an arm/shoulder assembly containing 114 muscle units on each side of the body and having a morphology defined by Van der Helm [5.11], (b) a spine model developed by de Zee et al. [5.12] comprising sacrum, all lumbar vertebrae, a rigid thoracic-spine section, and a total of 158 muscles, and (c) a pelvis and lower extremity model with a total of 70 muscles. In total, the model contains more than 500 individual muscle units and, hence, can be considered as a fairly detailed description of the human musculoskeletal system. The anthropometrical dimensions of the model are selected in such a way that they roughly correspond to a 50th percentile European male.

Segments and Joints: Within the model, the bodies (referred to as the "*segments*" within the AnyBody Modeling System) are treated as rigid with their mass/inertia properties derived from mass and shape of the associated bone and the soft tissue that is allotted to the bone. Joints in the human body are treated as idealized frictionless kinematic constraints between the adjoining segments. Both standard kinematic joints (e.g. spherical joints for the hips, hinge joints for the knees, etc.) as well as specially-developed joints (e.g. those used to represent kinematic constraints associated with floating of the scapula on the thorax) are employed.

Muscles: Muscles are treated as string contractile force –activation elements which span the distance between the *origin* and the *insertion points* through either the *via points* or by wrapping over the surfaces which stand on their way. Muscle wrapping problem is treated using a shortest-path contact-mechanics algorithm. Due to the fact that the problem considered in the present work is dynamic, muscles are modeled as being *non-isometric* (i.e. muscle strength is considered to be a function of the body posture and the rate of contraction). Also, *passive elasticity* of muscles (i.e. the resistance of the muscles to stretching) was considered.

Model Validations: The mechanics of the model is implemented as a full three-dimensional Cartesian formulation and includes inertial and gravity body forces. Integral validation of whole-body musculoskeletal models is very difficult to conduct. To the best knowledge of the present authors, validation of the whole-body musculoskeletal model is still lacking (due to major challenges which would be associated with such validation). However, various subsystems of the whole-body model were validated separately. For example: (a) The lumbar spine model was validated by de Zee et al., [5.12] by comparing the model prediction with *in vivo L4-5 intradiscal* pressure measurements of Wilke et al.

[5.13]; (b) de Jong et al. [5.14] validated the lower extremity model by comparing model-predicted muscle activations and pedal forces with their experimental counterparts obtained in pedaling experiments; and (c) The shoulder model was validated in the early work of Van der Helm [5.11].

V.2.3. The Muscle Activity Envelope

As originally recognized by An et al. [5.15], the *min/max* muscle-recruitment formulation, discussed in Section V.2.1, defines effectively a *minimum fatigue criterion* as the basis for muscle recruitment, i.e. the aim of the proposed muscle-recruitment strategy is to postpone fatigue of the "*hardest-working*" muscle(s) as far as possible. The physiological consequence of this strategy is that muscles tend to form groups with muscles within the same group having comparable activity levels. In particular, in the muscle group associated with the maximum muscle activity there will be usually many muscles which, in a coordinated manner, carry a portion of the load comparable with their individual strengths. Consequently, in this group, many muscles will have the same activity level, which will be referred to as *"the muscle activity envelope*". The linearity of the reformulated *min/max* criterion discussed earlier guarantees that the optimization problem defined by Eqs. 5.1 – 5.3, is convex and, hence, that the solution to the problem is unique and corresponds to the global optimum. In other words, there is no other muscle recruitment strategy which can reduce the muscle-activity envelope further. Moreover, since the muscle activity envelope represents the maximum muscle activation in the model, it can be interpreted as the fraction of maximum voluntary contraction necessary to support the imposed loads (wheel-chair push-exertion and gravity forces, in the present case) while maintaining the prescribed posture.

V.2.4. Wheel-Chair Model

The wheel-chair is modeled using four segments, i.e. the two wheels, the seat and the back-rest. These segments are constrained to the global reference frame and used merely for the visual representation of the wheel-chair. That is, these directly used in the musculoskeletal analysis of the wheel-chair propulsion problem. Instead, as explained in the next section, the interactions between the human and wheel-chair was modeled implicitly by prescribing the time-dependent motion to various human-body segments and the time-dependent force experienced by the right hand during wheel-chair propulsion.

V.2.5. Musculoskeletal Definition of the Wheel-Chair Propulsion Problem

As mentioned above, wheel-chair/human-body interactions were modeled implicitly by prescribing time-dependent motions and forces to the body, Figure 5-1. Specifically, seven points in the body (three of which were located on the thorax and one on the right humerus, the right radius, the right ulna and the right hand each) were used in the present case. Time-dependent positions of these points were obtained in a set of motion-capture laboratory experiments. Within these experiments, a male individual experienced with the use of a wheel-chair was instrumented with seven reflective markers on the outside of his spine, the right shoulder and the right arm. After a wheel-chair specialist adjusted the wheel-chair to match the anthropometry of the person propelling the chair, the individual was asked to propel the wheel-chair at a comfortable speed while

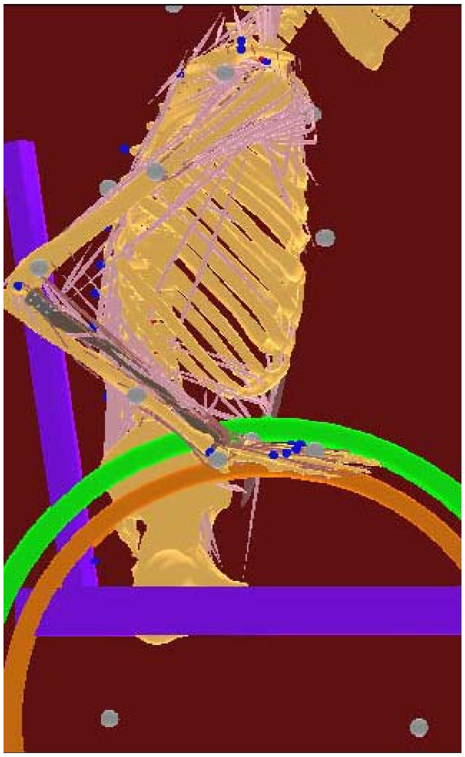

Figure 5-1. Scaled musculoskeletal model of a person propelling the wheel-chair (not scaled to size).

seven cameras recorded motion of the upper-body markers. Meanwhile, motion capture measurements were taken in order to locate and track the position of the reflective markers. The markers-position data recorded as a function of time were then used as input to the AnyBody Modeling System to drive the human body model during the simulated wheel-chair ride, Figure 5-2 [5.30]. The remainder of the body was then allowed to acquire the appropriate posture by adjusting kinematics of the spine in accordance with the so-called "*spinal rhythm*" algorithm. Within this algorithm, a single input, the pelvis-thorax angle, is used to determine the three rotational-joint angles of adjacent vertebrae (under a condition that the passive-elastic elements of the spine are able to force the spine to act cinematically as an elastic beam). The physical soundness of the spinal-rhythm algorithm for the seating posture has been validated by Rasmussen and de Zee using motion capture experiments [5.16].

Figure 5-2. Participant in the wheel-chair motion-capture experiments [5.30].

Time-dependent loads experienced by the right hand during wheel-chair propulsion were obtained using laboratory experiments and involved force-sensing push-rims operated by the laboratory participant. The data were collected at a sampling frequency of 240Hz. The collected data were next filtered using a forth-order, 20Hz low-pass Butterworth filter and then the resulting forces in Newtons were obtained via simple conversion from the collected data in Volts.

The markers-position and hand-force recorded data were finally fitted using an eight-order B-spline function, which enabled determination of instantaneous values of the marker locations and hand-push forces as required in the musculoskeletal analysis of wheel-chair propulsion.

V.3. FINITE-ELEMENT AND DESIGN-OPTIMIZATION PROCEDURES

As mentioned earlier, the results of the musculoskeletal wheel-chair propulsion analysis in the form of: (a) fractured-radius/implant assembly reference-frame/center-of-mass coordinates, orientations, velocities and accelerations as a function of time; (b) temporal variations of the spatial coordinates of the muscle attachment/via points and of the muscle forces; and (c) temporal variations of the spatial coordinates of the radius/elbow and radius/wrist joint reaction forces and moments, are exported from the AnyBody Modeling System and used, as input, in a finite-element/design-optimization analysis of the proximal radius-fracture fixation-plate implant. Some details pertaining to the finite-element/design-optimization analysis are presented in the remainder of this section. In Figure 5-3, the names and the spatial locations of the muscle-attachment/via points and the elbow and wrist joints are provided for the right radius. In this figure, there are 45 muscle attachment/via points and two joint points. Moments are transferred to the radius only at the two joint points since muscles, being contractile linear elements, can each provide only a force.

In Figure 5-4, a close-up is provided of the right radius along with the adjoining bones. As can be seen, the radius contains a proximal (i.e. next to the elbow) fracture and it is fixed with a lateral fracture fixation-plate implant. The implant is attached to the two segments of the fractured radius using six screws.

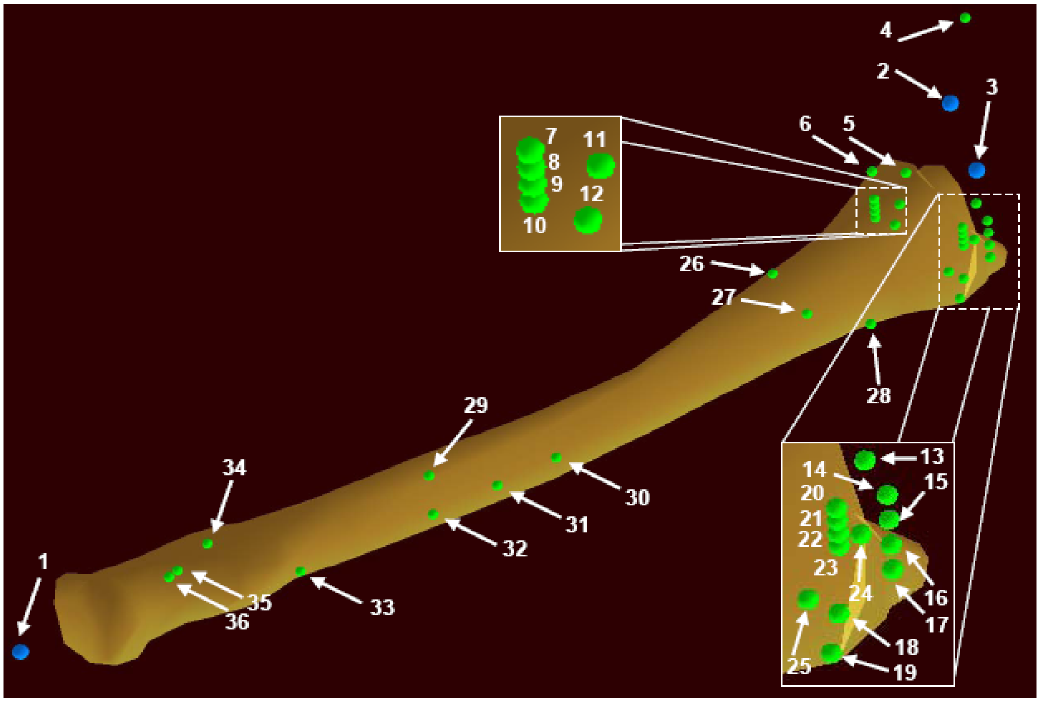

1 – PointPS2 Node (Elbow Joint Node)
2 – PS Node (Distal Pronation Supination Joint Node)
3 – Wrist Joint Node
4 – MedialExtensorCyl Node
5 – Via_Extensor_Indicis Node
6 – Via_Extensor_Digiti_Minimi Node
7– Via_Extensor_Digitorum_Digit5 Node
8 – Via_Extensor_Digitorum_Digit4
9 – Via_Extensor_Digitorum_Digit3
10 – Via_Extensor_Digitorum_Digit2 Node
11– Via_Extensor_Pollicis_Longus Node/Via_Abductor_Pollicis_Longus Node/Via_Extensor_Carpi_Radialis_Longus Node
12 – Via_Extensor_Carpi_Radialis_Brevis Node
13– Via_Palmaris_Longus Node
14 – Via_Flexor_Digitorum_Superficialis_Digit5 Node
15 – Via_Flexor_Digitorum_Superficialis_Digit4 Node
16 – Via_Flexor_Digitorum_Superficialis_Digit3 Node
17– Via_Flexor_Digitorum_Superficialis_Digit2 Node
18 – Via_Flexor_Pollicis_Longus Node
19 – I_Brach_rad_1 Node/I_Brach_rad_2 Node

20 – Via_Flexor_Digitorum_Profundus_Digit5 Node
21– Via_Flexor_Digitorum_Profundus_Digit4 Node
22 – Via_Flexor_Digitorum_Profundus_Digit3 Node
23 – Via_Flexor_Digitorum_Profundus_Digit2 Node
24– Via_Flexor_Carpi_Radialis Node
25– I_Pron_quadr_2 Node
26 – O_Extensor_Pollicis_Brevis Node
27 – SupinatorCyl Node
28 – I_Pron_quadr_1 Node
29 – BicepsCyl Node
30 – O_Flexor_Pollicis_Longus Node
31 – I_Pronator_teres_caput_humeral_1 Node/ I_Pronator_teres_caput_humeral_2 Node/I_Pronator_teres_caput_ulnare_1 Node
32 – I_Supinator_ulna_part_2 Node/I_Supinator_humerus_part_2 Node
33 – I_Supinator_ulna_part_1 Node/I_Supinator_humerus_part_1 Node
34 – I_Biceps_LH Node/I_Biceps_SH Node
35 – RadiusMuscleCy Node
36 – PronatorTeresCyl Node

Figure 5-3. Spatial location of various muscle attachment points to the right radius.

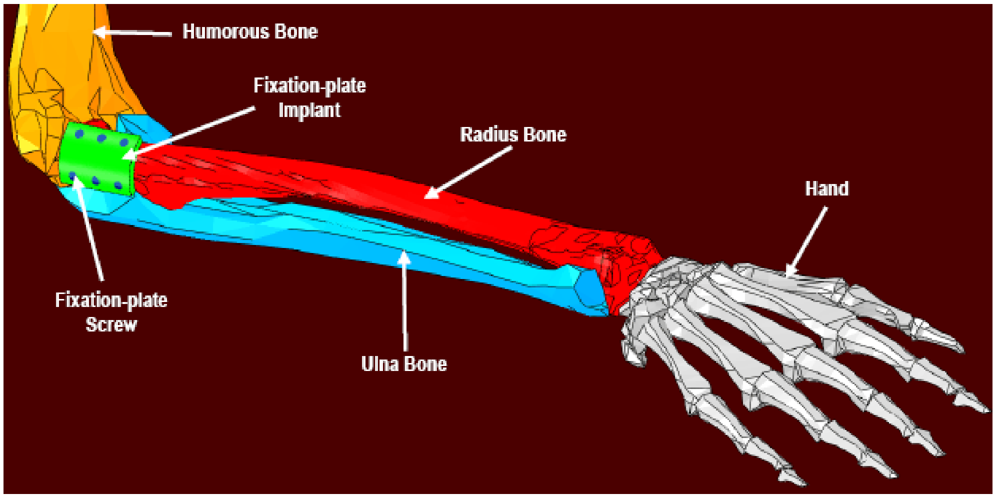

Figure 5-4. A close-up view of the fractured right radius (with a lateral fixation-plate implant and locking screws) and the adjoining bones at one time instant during a wheel-chair propulsion-simulation run.

V.3.1. Finite Element Model and Analysis

The Model

The finite element model analyzed consisted of a fractured right radius, a fixation-plate implant and six locking screws. Typical finite element meshes used are displayed in Figure 5-5. The radius, the plate and each of the screws were discretized using ca. 13,000 ten-node second-order tetrahedral solid elements, ca. 2,200 twenty-node second-order brick elements and ca. 200 twenty-node second-order brick elements, respectively.

To apply the muscle forces and joint-reaction forces and moments to the radius, each muscle-attachment/joint point is combined with a neighboring section of the radius surface to form a coupling. In this way, forces/moments acting at a muscle-attachment/joint point are transferred to the radius over a larger surface area preventing (unrealistic) stress-concentration artifacts.

To fasten the screws to the fixation plate and to the two bone segments, the outer surfaces of the screws are tied to the mating surfaces of the plate/radius. In other words, a "*perfect fastening*" condition is assumed to have been achieved using the screws.

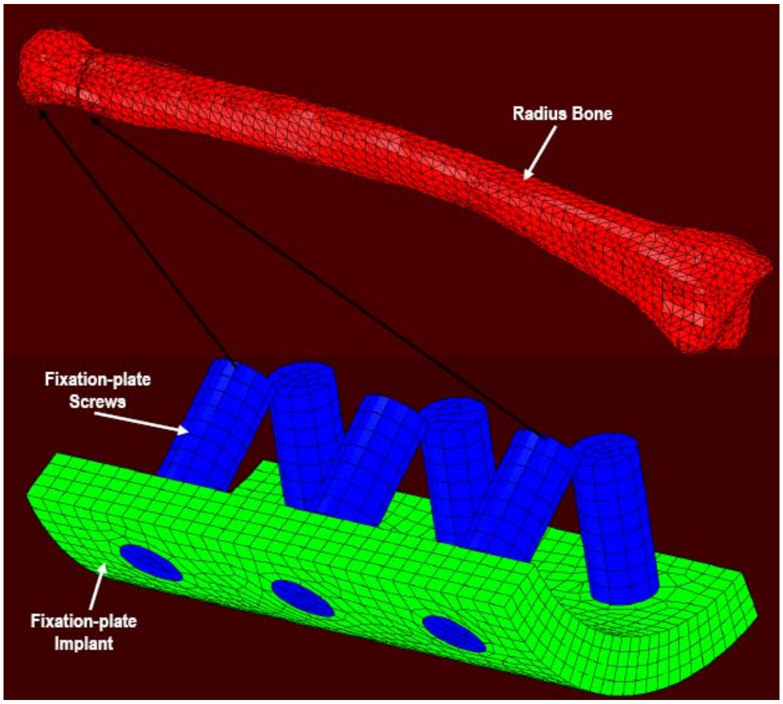

Figure 5-5. Typical finite-element meshes for the radius, the fixation-plate implant and six screws used in the quasi-static analysis of the implant longevity.

To prevent sections of the bottom surface of the fixation-plate implant between the screws from penetrating the radius, a "*penalty-type*" contact algorithm was employed. Within this algorithm, penetration of the contacting surfaces is opposed by a set of contact springs. Any level of contact pressure can be transmitted through the contact interface. Shear stresses are transmitted across the contact-interface in accordance with the Coulomb friction law.

Material Models

The fixation-plate implant and the seven screws are assumed to be made of Ti-6Al-4V, a Ti-based alloy which is commonly used in fractured-bone fixation applications. Ti-6Al-4V is modeled as a linear-elastic/ideal-plastic material.

To provide a higher level of realism to the analysis, it is recognized that radius is built of two types of bone tissues (*cortical* and *trabecular*) and that density (and hence mechanical properties) of the two types of bone tissues are spatially non-uniform. To obtain the necessary data for defining the cortical-bone/trabecular-bone dividing surfaces and the spatial distribution of the density within each of the two bone tissues,

Computed Tomography (CT) scans of the radius bone were analyzed [5.18]. An example of the CT scan of the radius bone is shown in Figure 5-6. For each bone tissue, the local gray-scale level is proportional to the local density. CT images like the one displayed in Figure 5-6 are analyzed using the Medical Imaging Software Mimics [5.19]. Within Mimics, the two bone tissues are differentiated by assigning two non-overlapping grayscale ranges, one for each bone tissue. Then, the gray-scale of each pixel within the two bone tissues is quantified using the Hounsfield Unit (HU) value. The latter are next converted into the corresponding bone-density values as: $\rho=1.9\cdot HU/1{,}700$, where the bone-density ρ is given in g/cm^3. Lastly, the relations listed in Table 4-1 in [5.18] were used to compute the Young's modulus as a function of the local density within the two bone tissues. A constant value of $\nu=0.3$ was used for both bone tissues. No plasticity within the radius was considered. In other words, it was assumed that the radius was made of two isotropic heterogeneous linear-elastic materials.

The Analysis

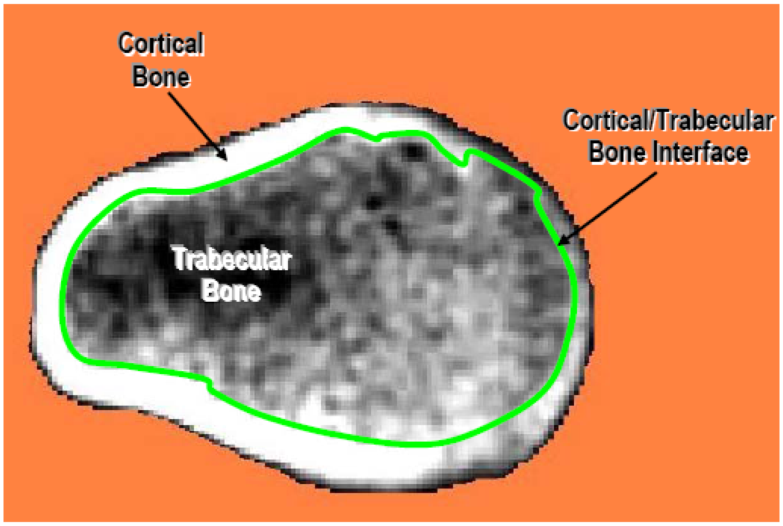

Figure 5-6. A typical Computed Tomography (CT) scan of the radius showing the presence of two bone tissues (the cortical and the trabecular) and the associated density variation within each bone tissue.

The results of the AnyBody-based multi-body dynamic wheel-chair propulsion analysis over a single hand-push cycle are exported at 100 equal time intervals. For each of these intervals, a quasi-static finite-element analysis of the radius/fixation-plate/screws assembly is carried out. At each of these time steps, the following AnyBody output information was used as input boundary/loading conditions (a) Spatial position of the radius/fixation-plate/screw assembly and the associated muscle-attachment and joint-reaction points; (b) muscle forces and joint-reaction forces and moments; and (c) the radius/plate/screws assembly (linear and angular) velocities and accelerations

The aforementioned AnyBody output data were used within the finite element model as follows: (a) the spatial position data were used to correctly position the finite-element model and the points for the application of concentrated forces and moments; (b) The muscle-force and joint-reaction force/moment data were used to define concentrated-load type of boundary conditions; and (c) The velocity and acceleration data were used to define distributed (gravity, inertia and centripetal) loading conditions.

The finite-element analysis results were used to determine: (a) if the fixation–plate implant has suffered (unacceptable) plastic deformation; (b) if the two contacting fractured surfaces of the radius have intruded into each other (also an unacceptable scenario); and (c) the stress-state of the most critical elements (elements which control the fatigue life of the fixation-plate implant).

All the calculations pertaining to the quasi-static response of the radius/plate/screws assembly are done using ABAQUS/Standard, a commercially available general-purpose finite-element program [5.20].

V.3.2. Design-Optimization Analysis

One of the main objectives of the present work was to carry out optimization of the proximal radius-fracture fixation plate implant design. The overall implant design/geometry was parameterized in terms of the following three parameters: (a) plate thickness (2-4 *mm*); (b) angular plate-size (35-45º); and (c) angular plate-position (10-170º), Figure 5-7: The information listed within the parentheses denotes the range of the parameter in question with the 100° angular plate-position being located on the proximal lateral side of the radius. Since the plate was modeled as a solid structure, changes in its geometry entailed continued re-meshing of this component during optimization. In addition, since the screws length also changed during optimization (in order to comply with the changing plate thickness), the screws had to be re-meshed as well. Likewise, since the depth/location of the holes within the radius changed during implant optimization, the two bone fragments had to be repeatedly re-meshed.

V.3.2.1. Structural Optimization

Structural optimization is a class of engineering optimization problems in which the evaluation of an objective function(s) or constraints requires the use of structural analyses (typically a finite element analysis, *FEA*). In compact form, the optimization problem can be symbolically defined as [5.21]:

Minimize the objective function $f(x)$

Subjected to the non-equality constraints $g(x) < 0$ and

to the equality constraints $h(x) = 0$

with the design variables x belonging to the domain D

where, in general, $g(x)$ and $h(x)$ are vector functions. The design variables x form a vector of parameters describing the geometry of a part/component. For example, x, $f(x)$, $g(x)$ and $h(x)$ can be part dimensions, part weight, a stress condition defining the onset of plastic yielding, and constraints on part dimensions, respectively. Depending on the nature of design variable in question, its domain D can be continuous, discrete or a mixture of the two. Furthermore, a structural optimization may have multiple objectives, in which case the objective function becomes a vector function.

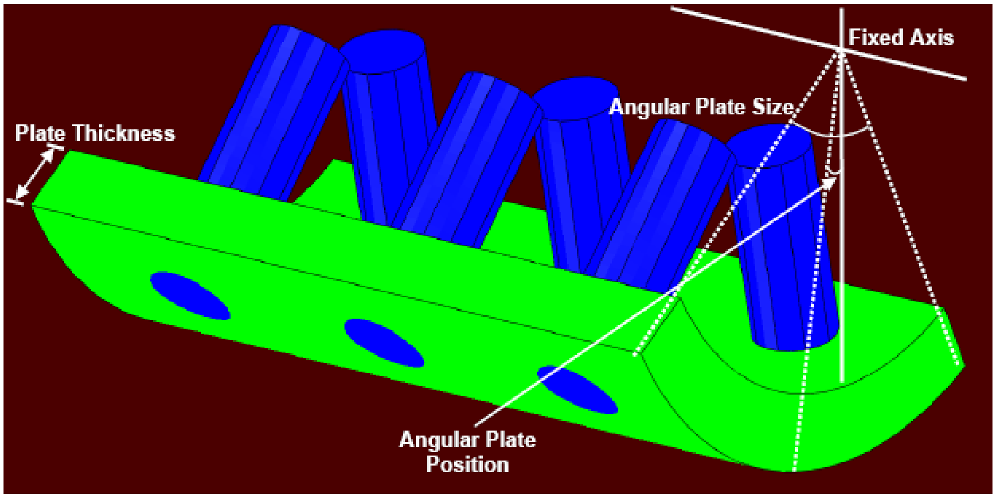

Figure 5-7. Definitions of the fractured-radius fixation-plate design/positioning variables used in the present implant optimization work.

Structural optimizations can be classified in many different ways. One of these classifications distinguishes between topology, size and shape optimization methods.

Topology Optimization: Topology optimization which is typically applied at the conceptual stage of part design represents the design domain as the continuum mixture of a solid material and "*voids*" and the optimal design is defined with respect to the distributions of the mixture density within the design space [e.g. 5.22].

Size Optimization: Within size optimization approach, the dimensions that describe part geometry are used as design variables, x. The application of size optimization is, consequently, mostly used at the detailed part-design stage where only fine tuning of the part geometry is necessary. Size optimization is typically quite straightforward and it generally requires no re-meshing of the finite element models during optimization iterations.

Shape Optimization: Shape optimization which is also mostly used at the detailed part-design stage, allows the changes in the boundary of part geometry. The boundaries are typically represented as smooth parametric curves/surfaces, since irregular boundaries typically deteriorate the accuracy of finite element analysis or may even cause the numerical instability of optimization algorithms. Because the product geometry can change dramatically during the optimization process, the automatic re-meshing of finite element models is usually required. Structural shape optimization methods are generally classified as: (a) direct geometry manipulation and (b) indirect geometry manipulation approaches. In the direct geometry manipulation approaches, design variable x is a vector of parameters representing the geometry of part boundary, e.g., the control points of the boundary surfaces. In the indirect geometry manipulation approaches, design variable x is a vector of parameters that indirectly defines the boundary of the product geometry. A comprehensive review of shape optimization based on the direct and the indirect geometry manipulation approaches can be found in Ref. [5.23].

V.3.2.2. Fractured-radius Fixation-plate Design/Positioning Optimization

The fractured-radius fixation-plate design/positioning optimization problem was defined as follows: The plate mass is to be minimized while ensuring that during wheel-chair propulsion no plastic deformation in the plate takes place, no interpenetration of the two fractured radius segments occurs and that no high-cycle fatigue failure will take place after a pre-selected number of hand-push crank revolutions (set to two million cycles, in accordance with a simple analysis presented in Section V.4).

The fractured-radius fixation-plate design/positioning optimization is carried out as a two-step procedure;

(a) within the first step, a full-factorial Design of Experiments (DOE) study was conducted using three design variables: the plate thickness (2.0, 2.5, 3.0, 3.5 and 4.0 *mm*), plate angular size (35, 37, 39, 41, 43 and 45 degrees) and plate angular position (10, 55, 100, 145 and 190 degrees), where the numbers within the parentheses represent the levels of each of the three design variables. The full-factorial matrix includes 5×6×5=150 discrete designs. Three of these designs, each associated with the same level of plate thickness (3 *mm*) and the angular-size (45º) but at three different angular positions (10, 100 and 190 º) are displayed in Figure 5-8; and

(b) once the DOE results are obtained and fitted to a higher-order mathematical function (the so-called "*Response Surface*"), the resulting meta-model is subjected to the standard three design variable optimization procedure. In other words, the optimization algorithm is applied to the higher-order mathematical function without the use of costly finite-element analyses. An example of the resulting maximum von Mises response surface for the complete ranges of the fixation-plate design at three different angular positions is shown respectively in Figures 5-8(a)-(c).

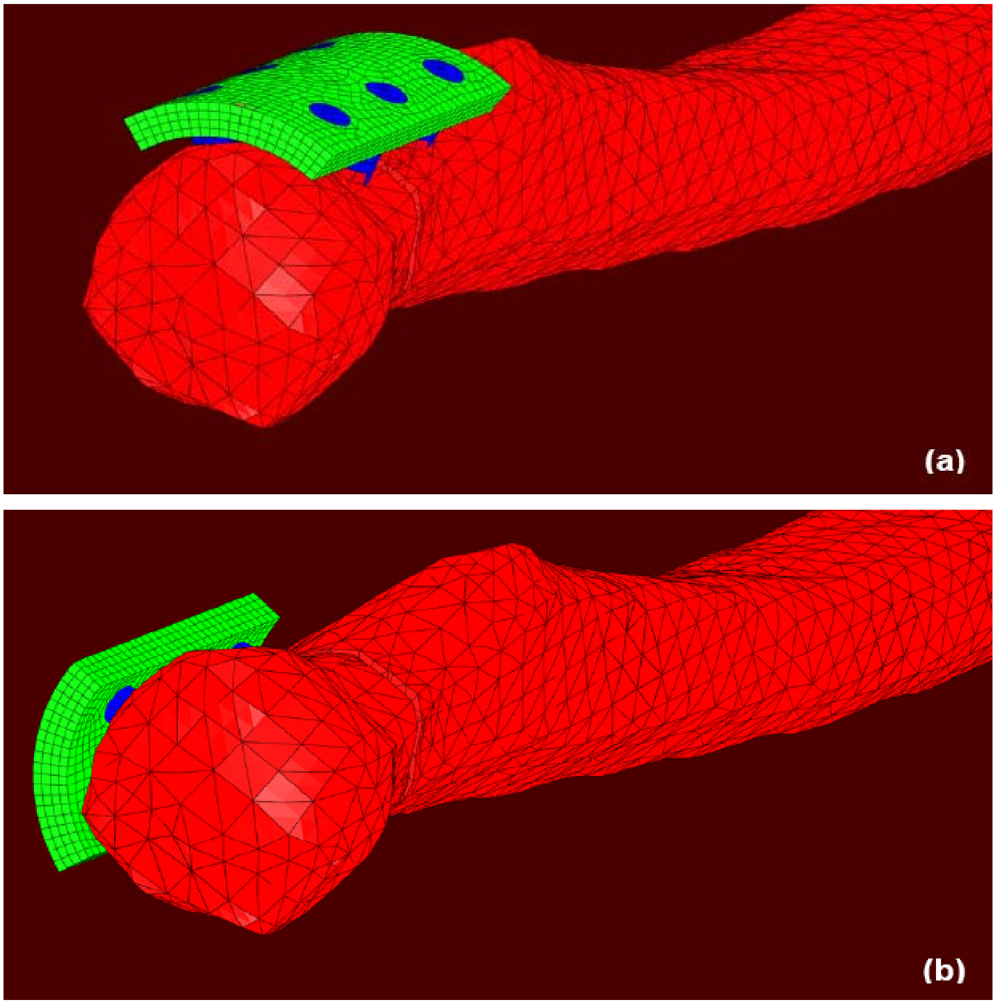
(a)
(b)

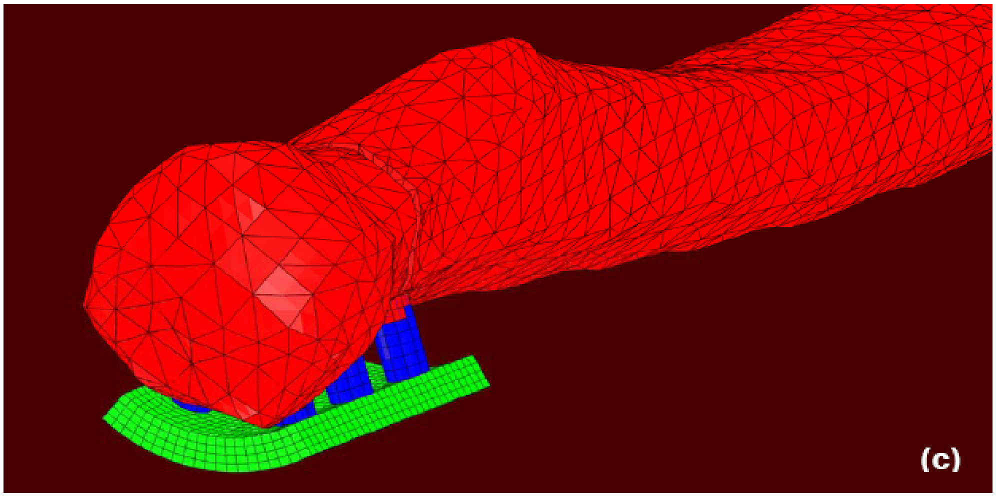

Figure 5-8. Examples of the fixation-plate design at three different angular positions. Please see text for details.

The fixation-plate design/positioning optimization problem was implemented into and solved using HyperStudy [5.24], a general purpose multi-disciplinary multi-objective optimization software. For a defined optimization problem, this software invokes a pre-selected DOE algorithm (a full-factorial method, in the present case) and an optimization algorithm (the Adaptive Response Surface Method [5.25], in the present case), prepares the appropriate input files for the finite-element analysis, launches the finite-element solver and reads and interprets the finite-element results in order to construct the response surface in the DOE case and to determine the immediate search direction in the design-optimization case.

V.3.2.3. Implant Fatigue-life Prediction

As mentioned earlier, one of the fractured-radius fixation-plate design-optimization constraints pertains to the attainment of a pre-selected lifecycle. Since this lifecycle is expected to be high-cycle fatigue controlled, a fatigue-based lifecycle prediction procedure had to be developed in the present work. The first step in this direction was to examine the temporal behavior of the muscle forces and reaction forces and moments during a single hand-push cycle. An example of the results obtained for the two (elbow and wrist) joint-reaction force and moment components is displayed in Figures 5-9(a) – (b). Simple examination of the results displayed in these figures show that the temporal evolution of various forces and moments is not in phase and that these forces/moments are not associated with constant amplitude. These findings have important consequences to the type of fatigue life prediction analysis which should be employed. Firstly, the non-constant nature of the load amplitude implies that a cycle-counting procedure (e.g. the so-called *Rainflow Cycle counting Analysis* [5.26]) should be employed in order to represent (highly-irregular) time-dependent loading as a collection of constant-amplitude (fixed mean-value) loading cycles. Secondly, since temporal evolution of the various muscle forces and joint-reaction forces and moments are out of phase, not only the magnitude of stresses/strains at an arbitrary point in the radius/plate/screw assembly varies as a function of time, but also the orientation of the associated principal coordinate system is time variant. The latter findings are what makes the loading "*non-proportional*" and the fatigue-life prediction more complex. In other words, the stress state in general, and the maximum principal stress specifically do not scale linearly with the overall load magnitudes. Consequently, to reveal the stress state history of the fixation-plate during a single hand-push cycle, finite-element analyses of the fractured radius subjected to the time-varying muscle forces and joint reaction-forces and moments had to be carried out multiple times (100 times in the present case) over a single hand-push cycle period.

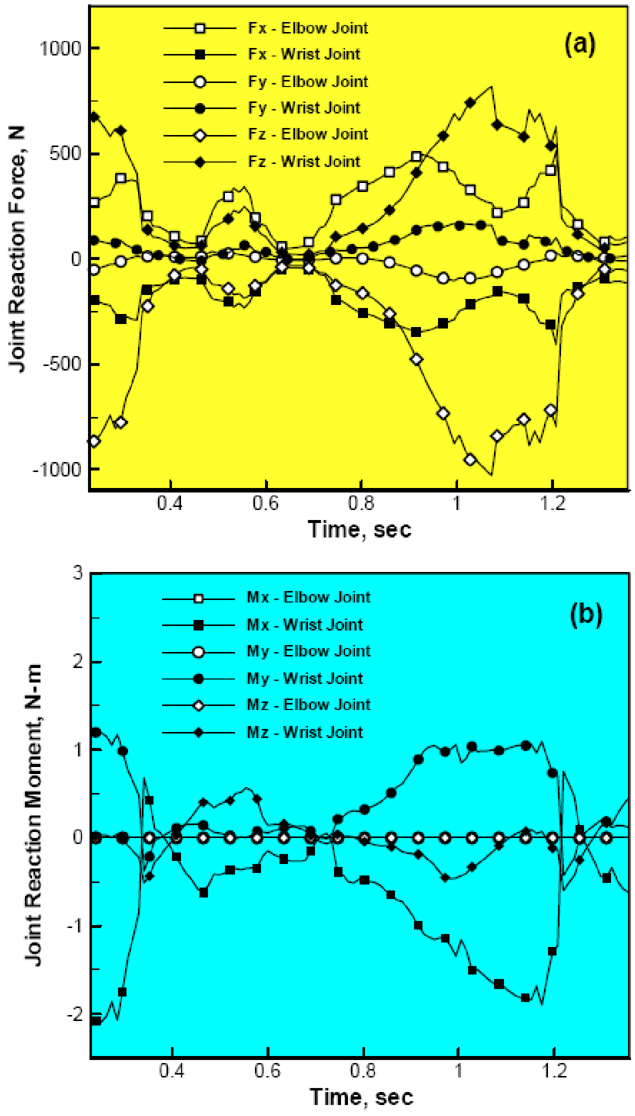

Figure 5-9. Temporal evolution of the elbow and wrist joint reaction forces and moments over a single hand-push cycle.

High-cycle Stress-based Fatigue Analysis

Due to a relatively simple geometry of the fractured-radius fixation-plate implant and the fact that a pre-defined high-cycle fatigue life is mandated for this component, it was deemed reasonable to assume that the fatigue-life of this component will be stress controlled. Furthermore it is assumed that the stress-based function responsible for the fatigue-induced failure is the maximum principal (tensile) stress. Next, stress-amplitude dependence of the number of cycles till failure is assumed to be defined by the traditional Basquin relation [e.g. 5.27] and the effect of the mean value of the maximum principal (tensile) stress is accounted for through the use of Goodman relation [e.g. 5.27]. The high-cycle fatigue parameters for Ti-6Al-4V are obtained from the Ansys fatigue material database [5.28].

To compute the number of cycles till failure for the given design/thickness of the fractured-radius fixation-plate implant, the procedure developed in our previous work was utilized [5.29]. Due to space limitations, only a brief overview of this procedure will be provided here. The main steps of this procedure applied to each finite element of the fixation-plate implant include:

(a) utilization of the finite-element calculation results to determine temporal evolution of the maximum principal (tensile) stress/strain;

(b) application of the rainflow cycle counting analysis to determine a three dimensional histogram relating the number of cycles with the maximum principal stress/strain amplitude and the associated mean value. An example of the typical results obtained in this portion of the work is displayed in Figure 5-10(a);

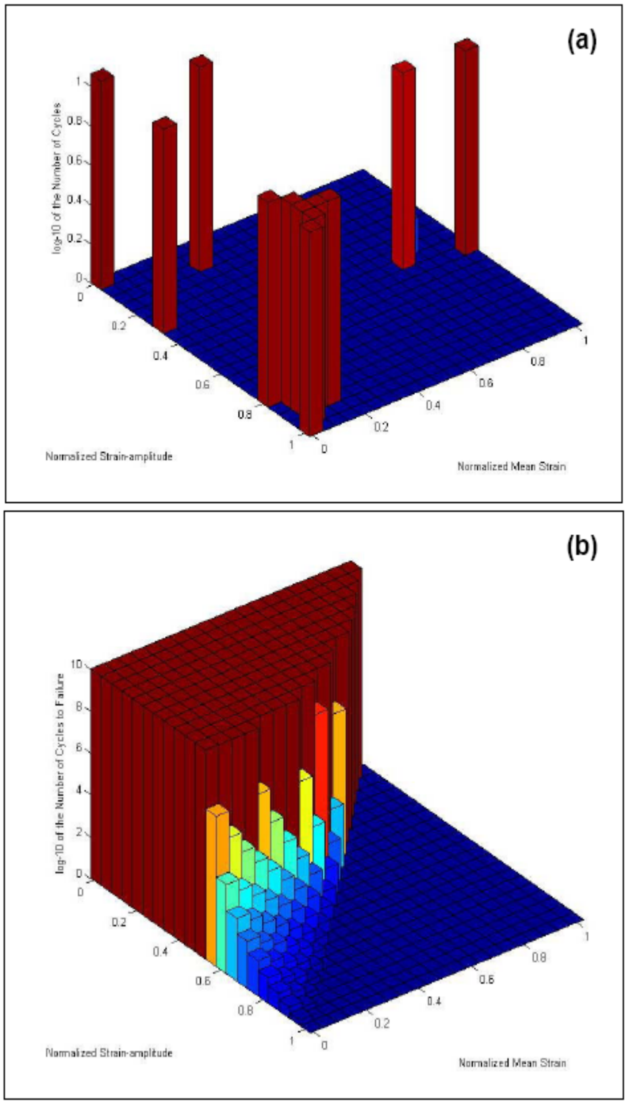

Figure 5-10. Typical: (a) Rainflow cycle-counting analysis; and (b) Goodman-diagram procedure results obtained in the fixation-plate implant fatigue-life assessment procedure.

(c) the use of the Goodman diagram for the calculation of the fractional damage associated with each load-cycle type (as characterized by a fixed value of the stress/strain amplitude and the stress/strain mean value). An example of the typical results obtained in this portion of the work is displayed in Figure 5-10(b); and

(d) computation of the total fractional damage associated with all load-cycle types and the use of the Miner's rule to compute the corresponding number of cycles till failure as an inverse of this fractional damage.

The fractured-radius fixation-plate implant life cycle is then set to that of its element associated with the smallest number of cycle till failure.

V.4. RESULTS AND DISCUSSION

V.4.1. Musculoskeletal wheel-chair Propulsion Analysis

As mentioned earlier the sole purpose of conducting the musculoskeletal wheelchair propulsion analysis was to obtain physiologically realistic loading conditions for the radius/fixation-plate/screws assembly. Specifically, at each of 100 time increments during a single hand-push cycle, the muscle forces and the joint reaction forces and moments as well as the spatial position of the muscle attachment/via points and the joint-reaction points had to be obtained from the musculoskeletal analysis. In addition, the spatial position and the orientation of the radius/plate/screws assembly at each time increment had to be obtained from the musculoskeletal analysis.

An example of the temporal evolution of the forces and moments acting on the radius (at the elbow and wrist joint points) was shown earlier, Figures 5-9(a) – (b). Similar results were obtained at muscle attachment/via points. As pointed out earlier these forces and moments are of non-constant amplitude and not in-phase resulting in non-proportional type of loading on the radius.

An example of the human-body/wheel-chair kinematics/muscle-activity results at four time intervals during a single hand-push cycle is shown in Figures 5-11(a) - (d). It should be noted that the activity of each muscle (i.e. the force produced by the muscle) is displayed pictorially in these figures by the thickness and the color shading of the line segments representing the muscles. Hence, the results displayed in Figures 5-11(a) - (d) can be used to qualitatively assess how the activity/recruitment of different muscles is changing during a single hand-push cycle, e.g., variation in the activity of the *Brachialis* muscle is marked in these figures.

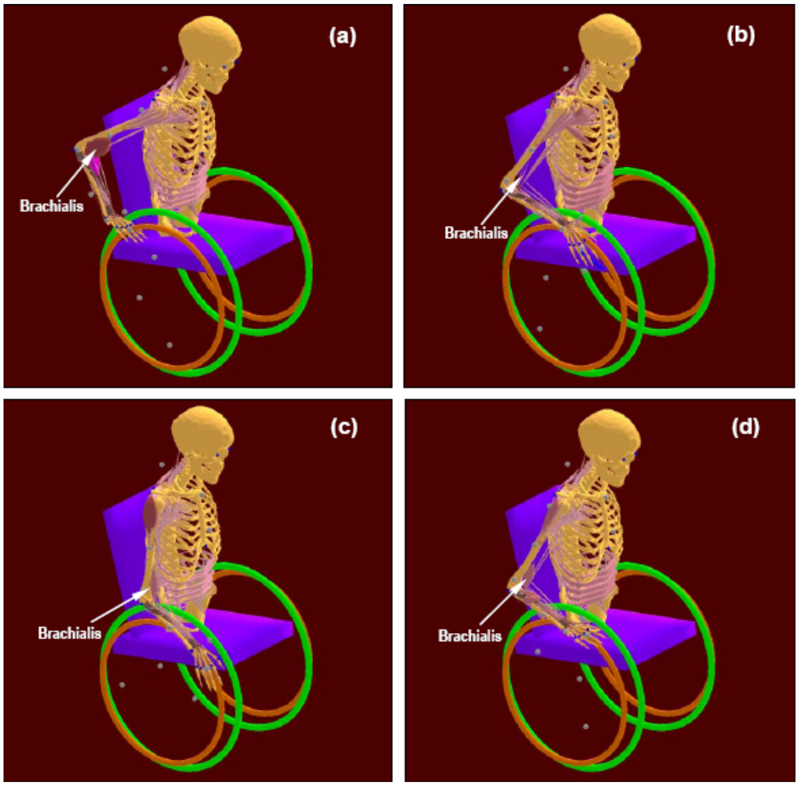

Figure 5-11. Temporal evolution of the human-body kinematics and muscles activity at four equally-spaced times during a single hand-push cycle.

V.4.2. Finite Element Results

Since it was assumed throughout this work that the locking screws can secure well the fixation-plate implant to the two fractured-radius segments, the focus of the finite-element investigation was placed on the fixation-plate implant. The three primary functional requirements imposed onto the implant were: (a) sufficiently high strength to prevent any plastic deformation within the fixation plate; (b) adequate bending stiffness to prevent the two radius segments from intruding into each other; and (c) a pre-selected fatigue life expressed as a number of hand-push cycles. Using an expected implant resident time of 3 years and an average daily number of hand-push cycling of 1,000, the implant fatigue life was set to two million cycles.

An example of the typical finite-element results is displayed in Figures 5-12(a) - (b). The results displayed in Figure 5-12(a) show that the von-Mises equivalent stress is substantially lower than the Ti-6Al-4V yield strength (930*MPa*). Thus under all the loading and fixation-plate design conditions the implant strength requirement was found to be met. Likewise, the condition regarding the maximum interpenetration of the fracture surfaces of the radius was found to be satisfied (i.e. <0.001m) for all combinations of loading conditions and the fixation-plate thickness.

As far as the fixation-plate implant fatigue-life requirements is concerned, it is found to be satisfied at some of the limits and not to be satisfied at the other limits of the implant-design/positioning optimization variables. As mentioned earlier the fatigue-life in the present case is controlled by the maximum principal stress. Figure 5-12(b) displays an example of the typical results pertaining to spatial distribution of this stress component. Clearly the elements surrounding some of the screw-holes are associated with the highest levels of the maximum principal stress and are likely to control the overall fatigue-life of the component.

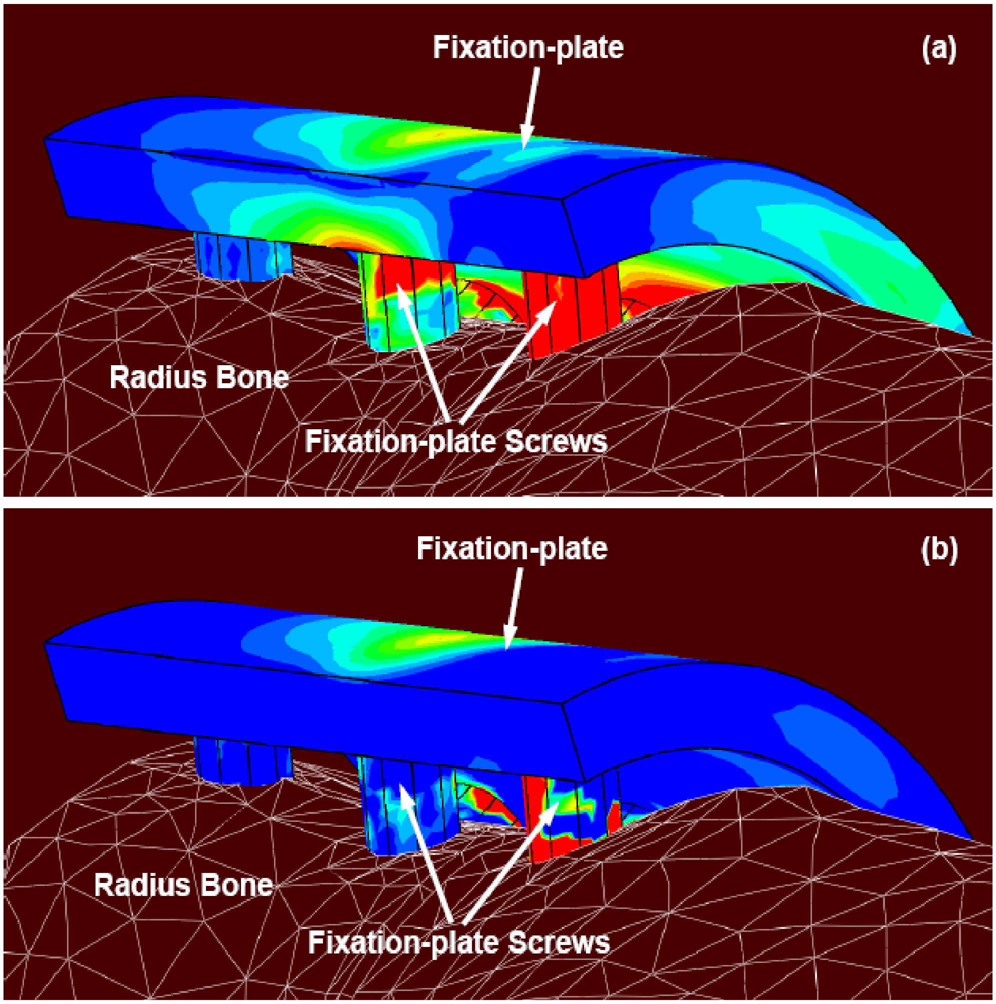

Figure 5-12. Typical results pertaining to the spatial distribution of: (a) von-Mises equivalent stress (red=30Mpa and blue=0.1Mpa); and (b) maximum principal stress (red=20Mpa and blue=-3Mpa).

V.4.3. Implant-Design/Optimization Results

As stated earlier, under all the implant-design and muscle/joint-imposed loading conditions, the functional requirements for the implant pertaining to its strength and bending stiffness were found to be satisfied. This is documented for the strength case in

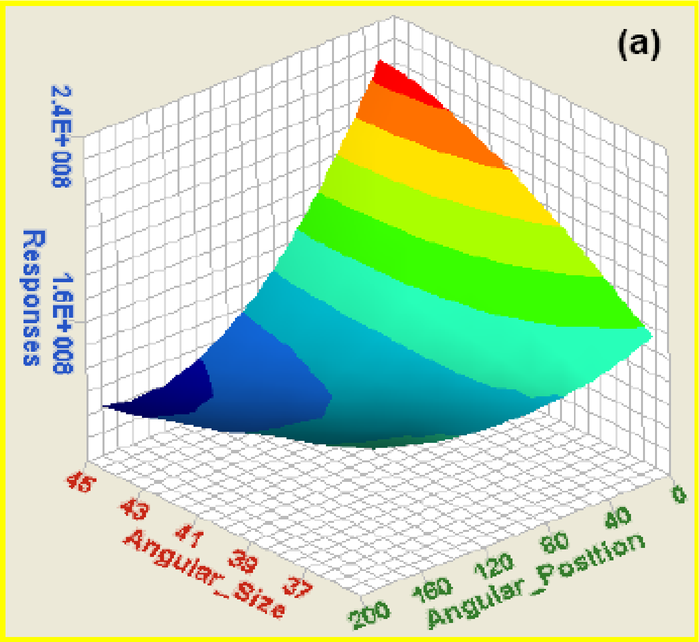
(a)
2.4E+008
Responses
1.6E+008
45
43
41
39
37
Angular_Size
200
160
120
80
40
0
Angular_Position

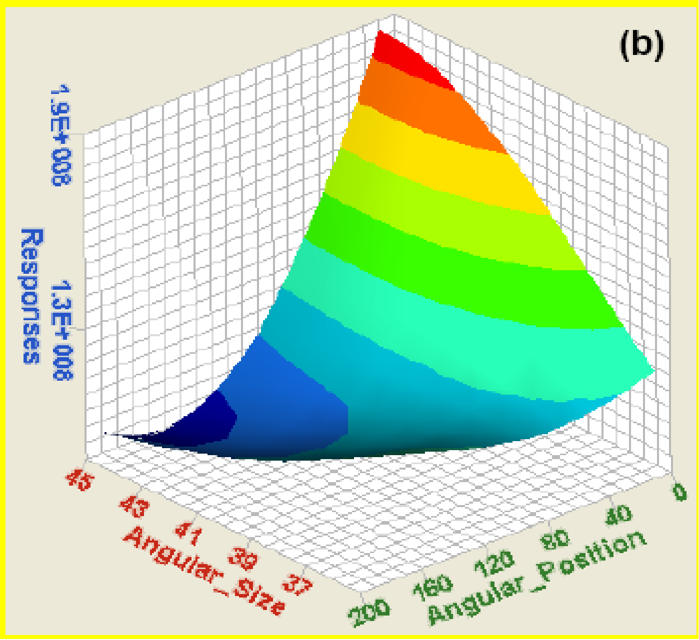
(b)
1.9E+008
Responses
1.3E+008
45
43
41
39
37
Angular_Size
200
160
120
80
40
0
Angular_Position

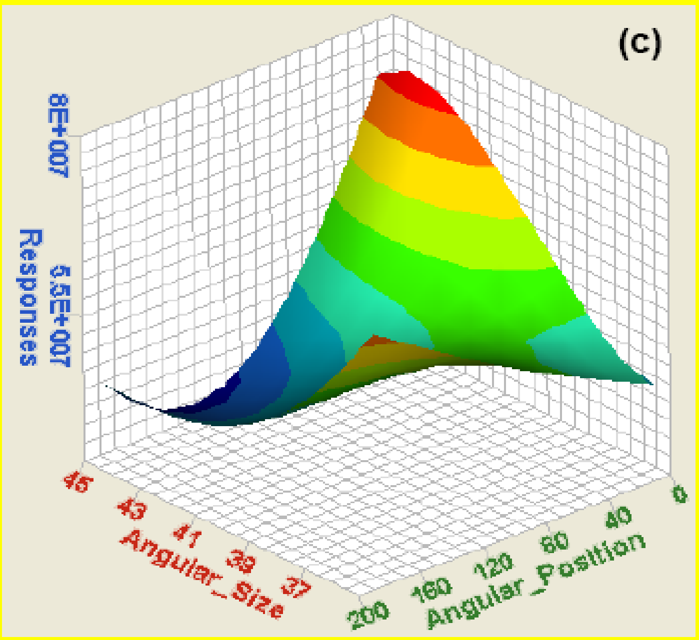

Figure 5-13. Typical results of the Design of Experiments study pertaining to the variation of the maximum von Mises stress as a function of the fixation-plate angular size and angular position at three levels of the plate thickness: (a) 2mm; (b) 3mm; and (c) 4mm.

Figures 5-13(a) - (c) in which the results of the DOE study are displayed for the von Mises stress as a function of the implant angular-size and angular-position at three different levels of the fixation-plate implant thickness. It is evident that the maximum von Mises stress for all the designs and all loading conditions represents only a minor fraction of the implant-material yield strength (930*MPa*). Based on these findings and the fact that the implant-design/positionining optimization is carried out within the same design domain used in the DOE study, the stiffness and strength requirements were not considered any further. The focus will be placed in this section on the functional requirement pertaining to the fatigue-life requirement of the implant.

Typical results pertaining to the progress of the implant design/positioning optimization are displayed in Figures 5-14(a) - (b). In Figure 5-14(a), the implant mass (objective function which is being minimized) is monitored as a function of the optimization iteration number. In Figure 5-14(b), on the other hand, the corresponding implant fatigue-life (one of the constraining function, the minimum acceptable value which is set to two million cycles) is also monitored as a function of the optimization iteration number. The results displayed in Figures 5-14(a) - (b) show that the optimized mass of the fractured-radius fixation-plate implant is around 6.07*g*. This optimal implant design is associated with the following values of the three design/positioning variables: (a) implant thickness of 3.06 *mm*; (b) implant angular-size of 41.090; and (c) implant angular-position of 105.7°.

V.4.4. Material Selection

Until this point in the present investigation, the same implant material, Ti-6Al-4V STA (*Solution Treated and Aged*) alloy was used. This is a commonly used fractured-radius fixation-plate implant material which provides a good combination of biocompatibility, mechanical performance and a low material/manufacturing cost. The present investigation has established that the key performance aspect of the fixation-plate implant under consideration is fatigue life. While retaining the requirements concerning low material/manufacturing cost and bio-compatibility (ensured by carrying out material selection within the family of Ti-based alloys), a material selection procedure was conducted in the present work in order to identify potential material substitutes for Ti-6Al-4V.

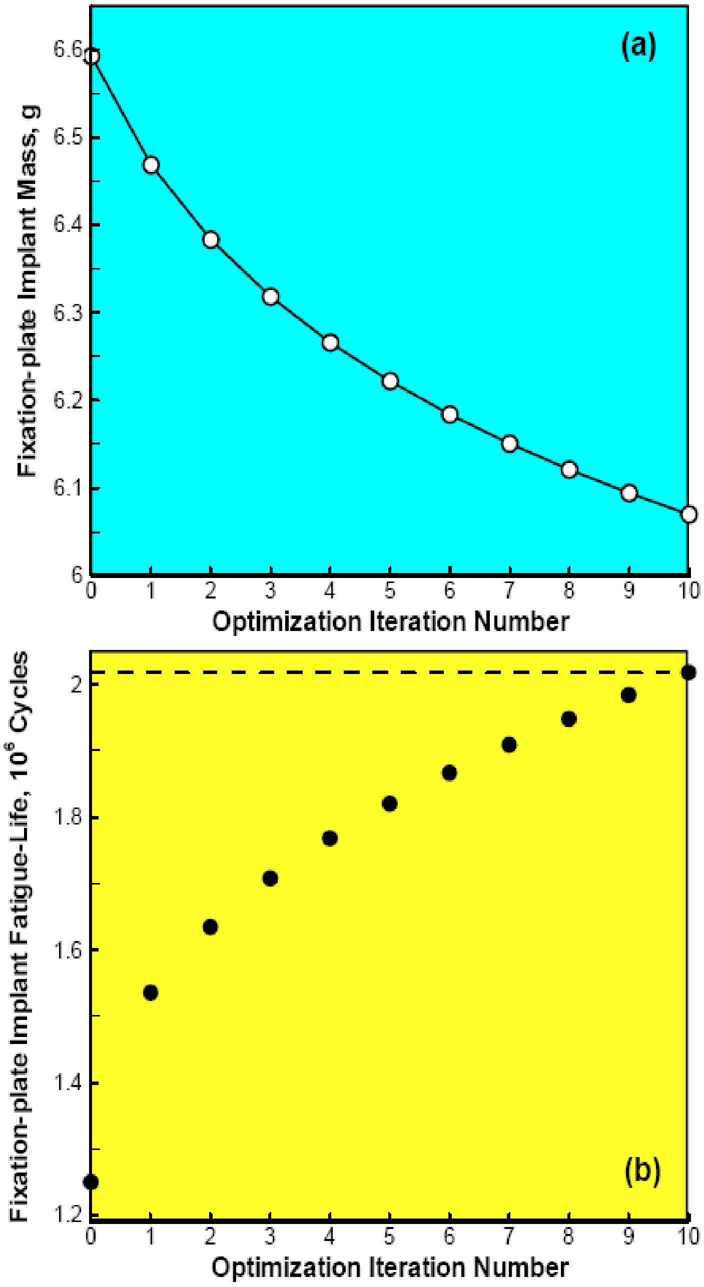

Figure 5-14. Variations of: (a) the radius fixation-plate implant mass; and (b) radius implant fatigue-life, with the successive design-optimization iteration numbers.

While examining different Ti-based material alternatives, it was found that in all cases considered, strength requirement can be readily attained. Consequently, implant-material selection was carried out with respect to simultaneously, satisfying the implant stiffness and longevity requirements only and, at the end of the material-selection process, it was confirmed that the strength requirements were indeed satisfied. In all the cases considered, it was found that the longevity requirement is more difficult to meet. Consequently, in defining a single material selection parameter, a higher weighting factor (w_{EL}=0.8) was selected for endurance limit and a lower weighting factor (w_{YM}=0.2) for the Young's modulus of the candidate material. For convenience, the endurance limit and the Young's modulus of each candidate material are normalized by their respective counterparts in Ti-6Al-4V. Thus, the material selection index for the fixation-plate implant is defined as:

$$M = w_{EL} \frac{\sigma_{EL}}{\sigma_{EL,Ti-6Al-4V}} + w_{YM} \frac{E}{E_{Ti-6Al-4V}} \tag{5.5}$$

where σ_{EL} denotes endurance limit while E is the Young's modulus. Clearly, M = 1.0 for Ti-6Al-4V and for a material to be considered as a potential substitute for Ti-6Al-4V, its M must be larger than 1.0.

It should be noted that the endurance limit of a material is typically obtained under zero mean-stress/strain loading conditions. Consequently, the use of this parameter in a material selection process does not take into account the important effect that mean stress/strain can have on the *"infinite-life"* material strength (i.e. the endurance limit). To overcome this problem, and still keep the material selection procedure relatively simple and manageable, a variable-mean stress/strain effective endurance limit is defined and used in Eq. 5.5. This quantity is defined as a weighted average of the endurance-limit values associated with different mean-stress/strain levels encountered during a simple hand-push cycle. The weighting factors in these calculations were set to the corresponding number fractions of the given mean-stress/ strain level encountered during a simple hand-push cycle.

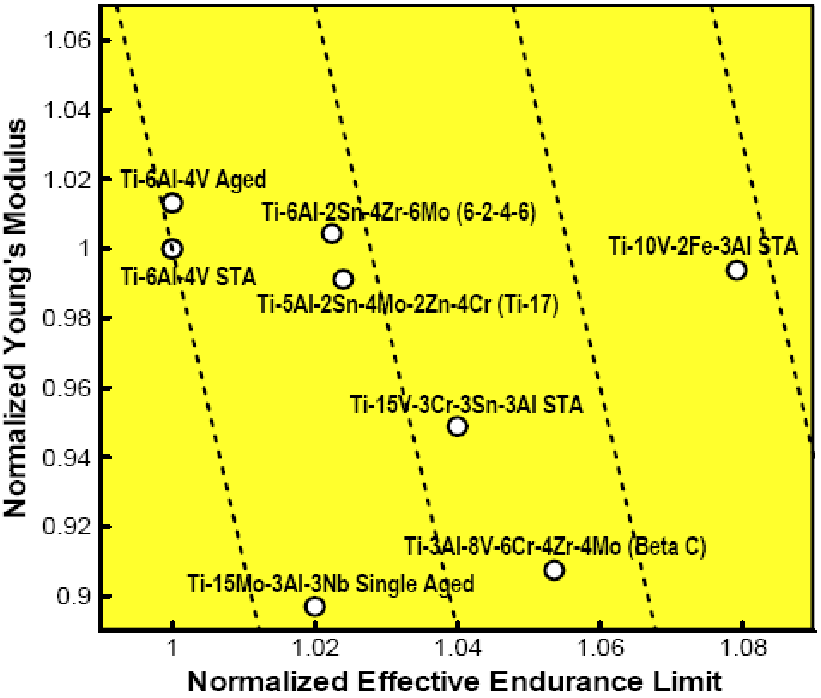

Figure 4-15. Material selection chart used in the analysis of potential replacement of Ti-6Al-4V as the fixation-plate implant material with other Ti-based alloys.

To assist the implant material-selection process, a normalized stiffness ($E/E_{Ti\text{-}6Al\text{-}4V}$) vs. normalized endurance limit ($\sigma/\sigma_{Ti\text{-}6Al\text{-}4V}$) plot is constructed in Figure 5-15. Few iso-*M* lines are also drawn in this figure. The results displayed in Figure 5-15 show that, with respect to the implant performance (as defined by its strength, stiffness, and longevity), Ti-10V-2Fe-3Al STA, Ti-3Al-8V-6Cr-4Zr-4Mo (Beta C) or Ti-15V-3Cr-3Sn-3Al STA may be a better alternative for the implant than Ti-6Al-4V. However, the final decision regarding the substitution of Ti-6Al-4V with these material alternatives should also account for material/manufacturing cost. Due to a lack of reliable/stable data pertaining to the cost of the materials in question, the effect of cost on material selection could not be taken into account in the present work.

V.5. SUMMARY AND CONCLUSIONS

Based on the work conducted and the results obtained in the present investigation, the following main summary remarks and conclusions can be drawn:

1. Design/positioning optimization of a fractured-radius fixation-plate implant is investigated computationally. To provide the realistic physiological loading conditions experienced by the implant during normal daily activities of the patient, a musculoskeletal multi-body dynamics analysis is coupled with implant finite-element/design-optimization methods.

2. The results show that out of the three functional requirements placed on the implant, (i.e. its strength, bending stiffness and longevity), it is longevity which typically controls the implant optimal design/positioning.

3. Under an assumption that the musculoskeletal multi-body dynamics analysis of the wheel-chair propulsion can be used to mimic the most critical loading conditions experienced by the radius-fixation implant during normal daily activities of the human with a surgically implanted radius-fixation plate, the optimal implant design and positioning were determined with respect to the attainment of a minimal implant mass.

4. In the final portion of the paper, potential material replacements have been considered for Ti-6Al-4V, the alloy used in the present finite-element/design-

optimization analysis of a radius-fixation implant, in order to further reduce implant thickness.

REFERENCES

[5.1]. K. C. Kim, J. K. Lee, D. S. Hwang, J. Y. Yang, Y. M. Kim, “*Distal Hybrid Interlocking in the Femoral Shaft Fracture,*” Orthopedics, 30:605, 2007.

[5.2]. M. Sivasankar, S. K. Dwivedy, D. Chakraborty, “*Fatigue Analysis of Artificial Hip Joints for Different Activities*,” 2nd International Congress on Computational Mechanics and Simulation, Guwahati, India, 2006.

[5.3]. D. D. D’Lima, N. Steklov, B. J. Fregly, S. A. Banks, C.W. Colwell Jr., “*In Vivo Contact Stresses during Activities of Daily Living after Knee Arthroplasty*,” J Orthop Res, 26, 2008.

[5.4]. L. Cristofolini, P. Savigni, A. S. Teutonico, M. Viceconti, “*In Vitro Load History to Evaluate the Effects of Daily Activities on Cemented Hip Implants*,” Acta of Bioengineering and Biomechanics, 5(2), 2003.

[5.5]. D. O. O'Connor, D. W. Burke, M. Jasty, R. C. Sedlacek, W. H. Harris, “*In vitro measurement of strain in the bone cement surrounding the femoral component of total hip replacements during simulated gait and stair-climbing*,” J Orthop Res, 14(5), 1996.

[5.6]. *AnyBody 3.0*, AnyBody Technology A/S, Aalborg, Denmark, 2008.

[5.7]. M. Damsgaard, J. Rasmussen, S.T. Christensen, E. Surma and M. de Zee, “*Analysis of Musculoskeletal Systems in the AnyBody Modeling System*,” Simul. Model. Pract. Theory, 14, 2006, 1100–1111.

[5.8]. J. Rasmussen and M. de Zee, “*Design Optimization of Airline Seats*,” SAE Conference, SAE no. 2008-01-1863, 2008.

[5.9]. S. Dendorfer and S. Torholm, “*Final Report on Feasibility Study,*” Report no: 21385/08/NL/PA, presented to ESTEC/ESA by AnyBody Technology A/S, May, 2008.

[5.10]. *AnyScript Model Repository 7.1*, AnyBody 3.0, AnyBody Technology A/S, Aalborg, Denmark, 2009.

[5.11]. F. C. T. Van der Helm, “*A Finite Element Musculoskeletal Model of the Human Shoulder Mechanism,*” J. Biomech., 27, 1994, 551–569.

[5.12]. M. de Zee, L. Hansen, C. Wong, J. Rasmussen and E. B. Simonsen, “*A Generic Detailed Rigid-body Lumbar Spine Model,*” J. Biomech., 40, 2007, 1219–1227.

[5.13]. H. Wilke, P. Neef, B. Hinz, H. Seidel and L. Claes, “*Intradiscal Pressure Together with Anthropometric Data – a Data Set for the Validation of Models,*” Clin. Biomech., 16 (Suppl. 1), 2001, S111–S126.

[5.14]. P. de Jong, M. de Zee, P.A.J. Hilbers, H. H. C. M. Savelberg, F. N. van de Vosse, A. Wagemakers and K. Meijer, “*Multi-body Modeling of Recumbent Cycling: An Optimization of Configuration and Cadence*,” Master’s Thesis Medical Engineering, TU/e Biomodelling and Bioinformatics, University of Maastricht, Movement Sciences, Aalborg University, 2006.

[5.15]. K. N. An, B. M. Kwak, E. Y. Chao and B.F. Morrey, “*Determination of Muscle and Joint Forces: A New Technique to Solve the Indeterminate Problem,*” J. Biomech. Eng., 106, 1984, 364–367.

[5.16]. J. Rasmussen, S. Torholm and M. de Zee, “*Computational Analysis of the Influence of Seat Pan Inclination and Friction on Muscle Activity and Spinal Joint Forces,*” International Journal of Industrial Ergonomics, 39, 2009, 52-57.

[5.17]. J. A. Bell and M. Stigant, “*Development of a Fibre Optic Goniometer System to Measure Lumbar and Hip Movement to Detect Activities and their Lumbar Postures*,” J. Med. Eng. Technol., 31, 2007, 361–366.

[5.18]. Z. Yosibash, R. Padan, L. Joscowicz, C. Milgrom, “*A CT-based high-order finite element analysis of the human proximal femur compared to in-vitro experiments,"* ASME, Journal of Biomechanical Engineering, 129 (3), 297–309, 2007.

[5.19]. Mimics, Medical Imaging Software, Materialise, User Documentation, 2009

[5.20]. ABAQUS Version 6.8-1, User Documentation, Dassault Systems, 2009.

[5.21]. P. Y. Papalambros and D. J. Wilde, “*Principles of Optimal Design: Modeling and Computation*,” Cambridge University Press, 2000, 2nd ed., Cambridge, UK.

[5.22]. M. P. Bendsoe and N. Kikuchi, “*Generating Optimal Topologies in Structural Design Using a Homogenization Method*,” Comput. Methods Appl. Mech. Eng., 1988, 71 2 , pp. 197-224.

[5.23]. R. T. Haftka and R. V. Grandhi, “*Structural Shape Optimization: A Survey*,” Comput. Methods Appl. Mech. Eng., 1986, 57(1) , pp. 91-106.

[5.24]. “*HyperStudy, User Manual*”, Altair Engineering Inc., Troy, MI, 2009.

[5.25]. U. Schramm, “*Multi-Disciplinary Optimization for NVH and Crashworthiness*,” Altair Engineering Inc., Troy, MI, 2007.

[5.26]. M. Matsuishi, T. Endo, “*Fatigue of Metals subjected to Varying Stress* ," Proceedings of Kyushi Branch, 1987.

[5.27]. P. Brondsted, H. Lilholt, A. Lystrup, “*Composite Materials for Wind Power Turbine Blades*,” Annual Review of Materials Research, 35:505-38, 2005

[5.28]. ANSYS Version 12, User Documentation, Ansys Inc., 2009.

[5.29]. M. Grujicic, G. Arakere, W. C. Bell, H. Marvi, H. V. Yalavarthy, B. Pandurangan, I. Haque and G. M. Fadel, “*Reliability-based Design Optimization for Durability of Ground-vehicle Suspension-system Components*,” Journal of Materials Engineering and Performance, accepted for publication, April 2009.

[5.30]. Rancho Los Amigos National Rehabilitation Center, http://www.rancho.org/research_home.htm

CHAPTER SIX

GENERAL SUMMARY AND CONCLUSIONS

In the present work, an attempt is made to utilize advanced computational techniques (i.e. musculo-skeletal multi-body dynamics and structural bio-mechanics finite element analysis) to investigate computationally a couple of ergonomics problems (i.e. seating comfort and long-distance driving fatigue) and a couple of bio-mechanics problems (i.e. the performance of femoral-fracture and radius-fracture fixation orthopedic implants).

In each case investigated, an effort was made to provide a deeper physical insight into the basic physics of the problem and to derive the appropriate figure-of-merit quantities. For example, in the case of seating comfort, an effort was made to define and evaluate a metric which quantifies the extent of comfort/discomfort experienced by a seated individual. In the case of long-distance driving fatigue, an effort was made to derive and evaluate the appropriate seating-induced fatigue function. In the case of the two fracture-fixation implant analyses, the work was focused on assessing the performance, validity and durability of the implants. In addition, a simple procedure for implant material selection was introduced and tested.

Lastly, in all four types of analyses employed, open-literature experimental data were gathered and used to validate the computational methods used. Overall, the agreement between the experiment and the computational predictions was reasonable providing support for the computational approaches employed in the present work.

CHAPTER SEVEN

RECOMMENDATIONS FOR FUTURE WORK

The present work can be extended in many different directions such as:

(a) More realistic hard and soft tissue material properties and their variations through the body parts investigated should be employed;

(b) Within the finite element approach, more realistic muscle model should be employed;

(c) More detailed durability of the implant should be considered;

(d) Potential for implant failure under brief-duration overloads should be also considered;

(e) Additional daily activities, such as walking, running, lunging, egress, etc. should be investigated within the musculo-skeletal multi-body dynamics models; and

(f) More detailed models within the finite element analyses should be employed for the joints.